Wind loads on heliostats and photovoltaic trackers

Pfahl, A.

Published: 21/06/2018

Document Version
Publisher's PDF, also known as Version of Record (includes final page, issue and volume numbers)

Wind Loads on Heliostats and Photovoltaic Trackers

Andreas Pfahl

/ Department of the Built Environment

bouwstenen 252

Wind Loads on Heliostats and Photovoltaic Trackers

PROEFSCHRIFT

ter verkrijging van de graad van doctor aan de Technische Universiteit Eindhoven, op gezag van de rector magnificus prof.dr.ir. F.P.T. Baaijens, voor een commissie aangewezen door het College voor Promoties, in het openbaar te verdedigen op donderdag 21 juni 2018 om 11:00 uur

door

Andreas Pfahl

geboren te Frankfurt am Main, Duitsland

Dit proefschrift is goedgekeurd door de promotoren en de samenstelling van de promotiecommissie is als volgt:

voorzitter:	prof.dr.ir. B. de Vries
1e promotor:	prof.dr.ir. B. Blocken
2e promotor:	prof.dr.-ing. R. Pitz-Paal (RWTH Aachen)
copromotor:	dr.ir. C.P.W. Geurts
leden:	prof.dr.-ing. B. Hoffschmidt (RWTH Aachen)
	prof.dr.ir. G.J.F. van Heijst
	prof.ir. H.H. Snijder
adviseur:	dr.-ing. R. Buck (DLR)

Het onderzoek of ontwerp dat in dit proefschrift wordt beschreven is uitgevoerd in overeenstemming met de TU/e Gedragscode Wetenschapsbeoefening.

Imprint

Wind Loads on Heliostats and Photovoltaic Trackers / Andreas Pfahl

A catalogue record is available from the Eindhoven University of Technology Library.
ISBN: 978-90-386-4545-2

Published as issue 252 in the Bouwstenen series.

The research presented in this thesis was prepared at the German Aerospace Center (DLR), Institute of Solar Research, department Solar Tower Systems, Stuttgart and at the Eindhoven University of Technology (TU/e), Department of the Built Environment.

Cover design: Andreas Pfahl
Cover photos: Wacker Ingenieure and BrightSource Energy

Printed by TU/e print service – Dereumaux
Eindhoven, The Netherlands

Technical development is based on

- *team-work/cooperation*
- *system/standardisation*
- *know-how/science*
- *creativity/innovation*

which requires skills of all of the four fundamental personality types first described by Hippokrates/Galenos.

Content

Abstract

For a cost effective design and dimensioning of heliostats and photovoltaic trackers the wind loading must be known as precisely as possible. Properties of the heliostat itself like size, aspect ratio, gaps in the mirror panel, and the kind of stow position are of impact on the wind loads as well as other parameters of the heliostat field like wind fence, heliostat field density, and position within the field. By atmospheric boundary layer wind tunnel investigations these impacts are determined. In the wind tunnel the wind conditions at full scale must be matched. The highest Reynolds numbers and larger eddies cannot be reproduced by usual boundary layer wind tunnels. It is investigated whether these deficits can be neglected for the investigation of heliostats and PV trackers. Also the maximum gust duration has an impact on the wind loading. By full scale measurements it is investigated whether the maximum gust duration is limited enough that the maximum loads could be reduced by shock absorbers. The theory of extreme value statistics for the determination of the wind load peak values and the correlation between eddy diameters and turbulent energy spectra are explained in the appendix.

1 Introduction

1.1 Solar Tower Plants

This section is reproduced from [Pfahl, A., Coventry, J., Röger, M., Wolfertstetter, F., Vasquez, F., Gross, F., Arjomandi, M., Schwarzbözl, P., Geiger, M., Liedke, P., 2017. "Progress in Heliostat Development". Solar Energy 152, 3-37].

Concentrated solar thermal (CST) energy is a promising renewable energy technology capable of large scale electricity production and industrial process heating, usually incorporating energy storage. The main CST technologies are dish-Stirling systems, linear Fresnel systems, trough systems and tower systems. In a solar tower plant, moving mirrors called 'heliostats' track the sun in two axes and reflect the sun's rays onto a 'receiver' at the top of a tower (Fig. 1). The receiver absorbs the radiation and supplies thermal energy via a working fluid at a temperature of typically 300-700°C. At solar power plants the thermal energy is converted into electrical energy which is then called concentrated solar power (CSP). For power towers incorporating energy storage, the working fluid is usually also a heat storage medium (e.g. molten salt), and is stored in tanks to allow power generation upon demand. Alternatively, the energy received by the solar tower plant may be used for providing heat to a thermochemical process, such as the production of synthetic transport fuels.

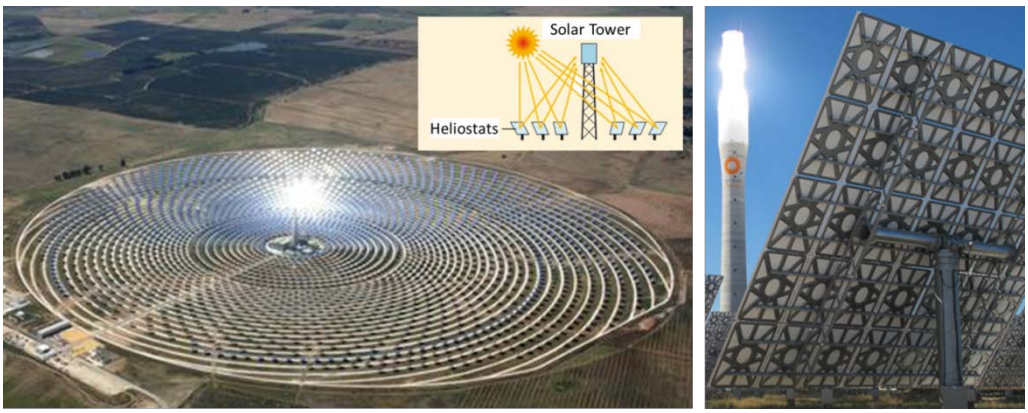

Fig. 1: First commercial solar tower plant with storage using molten salt (Torresol Energy, 2017), (schematic by DLR)

A photovoltaic (PV) power plant currently provides electrical energy at a lower cost than a CSP plant. However, storage of electrical energy is in general more expensive than storage of thermal energy. Therefore, PV plants that

would require electrical energy storage are more suitable for power supply during sun hours and CSP plants during the night and in cloudy conditions because they can use less expensive thermal energy storage. A combination of both PV and CSP is seen as a promising solution for future power supply: “The cost of solar technologies are falling so quickly that within a few years the combination of solar PV and solar towers with storage will be able to compete directly with base load fossil fuels” (Padmanathan, 2015). Indeed, this aim was reached in 2017 by several bidding prices (see e.g. (Clean Technica, 2017)). An important advantage of CSP compared with PV is that during construction a high fraction of labour and equipment is sourced locally, which is especially attractive for developing countries.

Examples of industrial processes that could be driven by solar tower plants are cement production (Gonzáles and Flamant, 2014) and enhanced oil recovery (CSP today, 2013). Solar tower systems can also supply competitively heat to thermal processes at 550°C or below, although 500°C has been achieved as well by some small CSP demonstration plants with trough collectors which had been of lower cost so far. Many industrial processes are designed for higher working temperatures, which are provided by fossil fuel burners. To incorporate solar input it is sufficient to replace only the burner with a solar receiver and the rest of the plant stays almost unchanged. With further reduction of the cost of concentrated solar systems, applications for solar thermal industrial processes will become economically viable.

1.2 Objective

The heliostats represent 40-50% of the cost of a solar tower plant, so they must be relatively low cost for the cost of energy from the plant to be competitive with that of fossil fuels (Mancini et al., 2000). It was shown by Gary et al. (2011) that to achieve a levelised cost of electricity (LCOE) of 0.10 USD/kWh the heliostats must cost no more than 120 USD/m². The heliostats must cost about 75 USD/m² if the target LCOE is 0.06 USD/kWh (Gary et al., 2011). To achieve these targets, innovative designs and solutions regarding the complete heliostat concept and its components are needed. Furthermore, the dimensions of heliostats must be selected to minimise manufacturing and installation costs. This requires accurate estimation of the wind loading on both operating and parked (stowed) heliostats to allow structurally efficient heliostat designs to be developed with good optical performance characteristics, while avoiding structural failure. The objective of the presented

thesis is to close knowledge gaps and to reduce uncertainties regarding the wind loading of heliostats.

Some of the main open questions regarding wind loads on heliostats were:

- How can the wind loads on heliostats be reduced in an economic way?
- Which is the optimum aspect ratio of the mirror panel?
- At which heliostat field position do maximum wind loads occur?
- Are the wind load coefficients of heliostats Reynolds number dependent?
- Which turbulence properties have to be matched by wind tunnel tests?
- Can the peak wind loads be reduced by shock absorbers?

These open questions are addressed by the thesis.

1.3 Structure of the Thesis

At first, it is shown how the wind loads impact the heliostat design (2). Therefore, after a short description of heliostats (2.1) it is explained how the wind loads have to be taken into account for the dimensioning of heliostats (2.2) and how the wind loading can be reduced by the heliostat design or how the resistance of the heliostat against it can be increased (2.3).

Then it is investigated how heliostat properties impact the wind loading (3). An important property is the aspect ratio. For a wide range of aspect ratios the wind load coefficients are determined by atmospheric boundary layer wind tunnel (BLWT) tests for varying elevation angle and wind direction. Reasons for the aspect ratio dependency of the different wind load components are given (3.1). Only few heliostat designs have wide gaps between mirror panels. Therefore, only one sample heliostat was measured to see whether wide gaps could have a significant impact on the wind loads (3.2).

Regarding heliostat fields (4), it is investigated how wind fences could reduce the wind loads at different positions (4.1) to address the question whether a wind fence is worthwhile. Peterka and Derickson (1992) measured an increase of maximum drag and lift within a field compared to an isolated heliostat but give no reasons for this increase. By BLWT tests, this thesis provides an explanation for this finding (4.2).

For realistic results of BLWT tests it is important to match certain wind properties (5). At conventional BLWTs the high Reynolds numbers associated with a storm cannot be reproduced at reduced scale. For heliostats in operation only negligible Reynolds number dependency is expected because the separation occurs at the edges of the heliostat. However, for stow position

the wind “sees” the round torque tube of the heliostat at which the separation points are not fixed and clearly defined. In a high pressure wind tunnel with higher possible Reynolds numbers it was investigated whether this leads to a significant Reynolds number dependency of the wind load coefficients (5.1).

Besides the Reynolds number, it is important to match the turbulence characteristics of the flow. Turbulent energy spectra characterise the distribution of the turbulent energy over the frequencies of the fluctuations of the flow. Unfortunately, in conventional BLWTs the spectra cannot be fully matched because of the restrictions in size. It is investigated whether this mismatch has a significant impact on the measured wind load coefficients and pressure distributions and whether the heliostat size and height is of impact on the wind load coefficients (5.2).

The maximum gust duration causing the peak hinge moment in stow is measured by full scale measurements in (5.3). If short enough, load reduction could be achieved by shock absorbers.

The background of the BLWT investigations is the theory of extreme value statistics and turbulent energy spectra. These theories are shortly described in Appendices A and B respectively.

2 Impact of Wind Loads on Heliostat Design

Partly reproduced from [Pfahl, A., Coventry, J., Röger, M., Wolfertstetter, F., Vasquez, F., Gross, F., Arjomandi, M., Schwarzbözl, P., Geiger, M., Liedke, P., 2017. "Progress in Heliostat Development". Solar Energy 152, 3-37].

Nomenclature

A	[m²]	mirror/PV panel surface
c	[-]	wind load coefficient
f_{field}	[-]	field factor: max. wind load in field / wind load isolated heliostat
F	[N]	wind force
F_x	[N]	drag force
F_z	[N]	lift force
h	[m]	chord length of mirror or PV panel (in wind direction)
H	[m]	height of mirror/PV panel in stow position
M	[Nm]	wind moment
M_{Hy}	[Nm]	hinge moment
M_y	[Nm]	overturning moment at pylon base
M_z	[Nm]	moment about vertical axis
n	[-]	exponent of power law of mean wind speed profile
R	[-]	gust factor (U_{peak} / U_{mean})
U_{peak}	[m/s]	peak horizontal longitudinal wind component (gust wind speed)
x	[m]	coordinate, horizontal, in flow direction
y	[m]	coordinate, horizontal, perpendicular to flow direction
z	[m]	coordinate, vertical
ρ	[kg/m³]	density of air

BLWT	Boundary Layer Wind Tunnel
DLR	German Aerospace Center
DNI	Direct Normal Irradiation
FEM	Finite Element Method
PV	Photo-Voltaic

2.1 Description of Heliostats

A good description of heliostats is given by Mancini (2000): "Heliostats provide the *fuel* for a power tower (sometimes referred to as a central receiver) power

plant. Heliostats are named *helio* for sun and *stat* for the fact that the reflected solar image is maintained at a fixed position over the course of the day. They are nearly flat mirrors (some curvature is required to focus the sun's image) that collect and concentrate the solar energy on a tower-mounted receiver located 100 to 1000 meter distant."

The main heliostat sub-functions and their related components (Fig. 2) are the following (Pfahl, 2014):

1. Reflecting sunlight: mirrors
2. Fixing mirror shape: mirror support structure
3. Ground connection: pylon and foundation
4. Offset determination: control
5. Rotation of mirror panel: drives

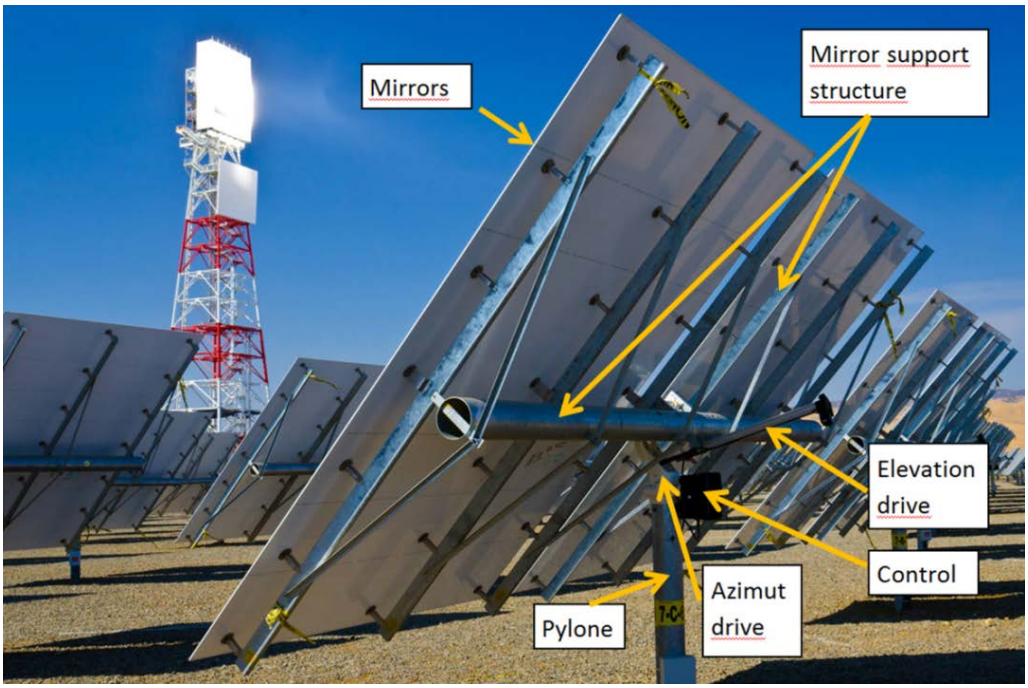

Fig. 2: Heliostat components (Brightsource Energy, 2012)

Details about the single heliostat components are given by Pfahl et al. (2017a, paragraph 4).

2.2 Heliostat Dimensioning Regarding Wind Loads

2.2.1 *Heliostat Size*

When the basic parameter of a heliostat, its size, is defined wind loads have to be taken into account. “What is the cost optimum size of a heliostat?” is a widely discussed but still open question. An analysis of the impact of the heliostat size on the cost is given by Kolb et al. (2007, Appendix A), showing that the curve of optimum size is quite flat. Therefore, the optimum size depends strongly on the specific conditions, and no general answer can be given. The main advantage of large heliostats is that less parts and fewer foundations are needed. The main advantage of small heliostats is that wind speeds are lower because of the low height and that their weight per mirror surface can be smaller. The reason for the lower specific weight is the following (Pfahl et al., 2017a):

By increasing the width and the height of the mirror panel the mirror area increases to the power of two. All other dimensions of the heliostat must be increased according to the width and height to avoid an increase of the stress caused by the peak wind loads. Therefore, the volume and the mass of the heliostat increase with increasing width and height to the power of three or with increasing mirror area to the power of 1.5 respectively (Kolb et al., 2007, A.3) (impact of larger wind loads due to larger wind speeds at increased height of larger heliostats neglected). Because the weight is a measure for the cost, especially for high production rates, small mirror support structures are advantageous due to their lower specific weight. Accordingly, for some heliostat concepts very small heliostat sizes were chosen (in particular, 2m² size in (Ricklin et al., 2014)).

However, also very large heliostats are realised (e.g. Titan-tracker) at comparably low weight and cost. The reason is that for larger heliostats more complex structures with low specific weight like frame work cantilever arms can be realised.

2.2.2 *Tracking Accuracy*

The tracking error is usually defined as the standard deviation of the difference between the actual and the ideal orientation of the optical axis of the heliostat across a year. Partly, the deviation can be caused by systematic errors like imperfect orientation of the rotation axes or errors in the calculation of the sun position. Systematic errors can be calibrated and corrected by aiming the focal spot to an extra target which is seen by a camera. The centre of the focal spot is determined and the deviation from the given aim point is calculated. This

deviation is determined for several incident angles of the sun. With the deviations for different incident angles, the single errors can be calculated and corrected by the control (Berenguel, 2004).

The error caused by backlash of the drives cannot be corrected in this way. Backlash in combination with (turbulent) wind causes fluctuations of the position of the focal spot. If the drives are sufficiently pre-tensioned backlash has no impact at all. For the elevation axis, pre-tensioning can be realised by unbalancing the mirror panel. However, for the vertical axes, pre-tensioning by gravity is not possible. Fig. 3 shows a heliostat with pre-tensioning of the azimuth drive by spring elements. Usually, for the azimuth drive expensive high precision gears with low backlash are needed.

Fig. 3: Heliostat with pre-tensioned azimuth drive via spring (Brightsource Energy, 2012)

It is not trivial to calculate the standard deviation caused by a certain backlash because the influence of fluctuating wind conditions throughout the year and throughout the heliostat field and the breakaway torque have to be considered. Teufel et al. (2008) describe a method to calculate the impact of the backlash on the annual energy yield of a plant. However, this method is yet to be validated. The standard deviation can be determined by measuring the deviation of the position of the centre of the focal spot for several characteristic periods of time to gain a probability distribution of the deviation. A Gaussian distribution can be fitted to it to achieve the standard deviation.

2.2.3 *Deformation by Gravity and Wind During Operation*

The heliostat structure must be rigid enough to avoid significant deformation due to changes of the mirror orientation. A deformation of the torque tube would lead to a misalignment of the mirror facets. Fig. 4 shows how the focal spot splits up for a heliostat with an under-designed torque tube. The facets are canted to achieve a small focal spot at solar noon. In early morning and late afternoon the mirror panels and the torque tube are oriented differently which leads to a different deformation of the torque tube and a different angle of the facets relative to the torque tube, resulting in a significant slope error of the mirror panel.

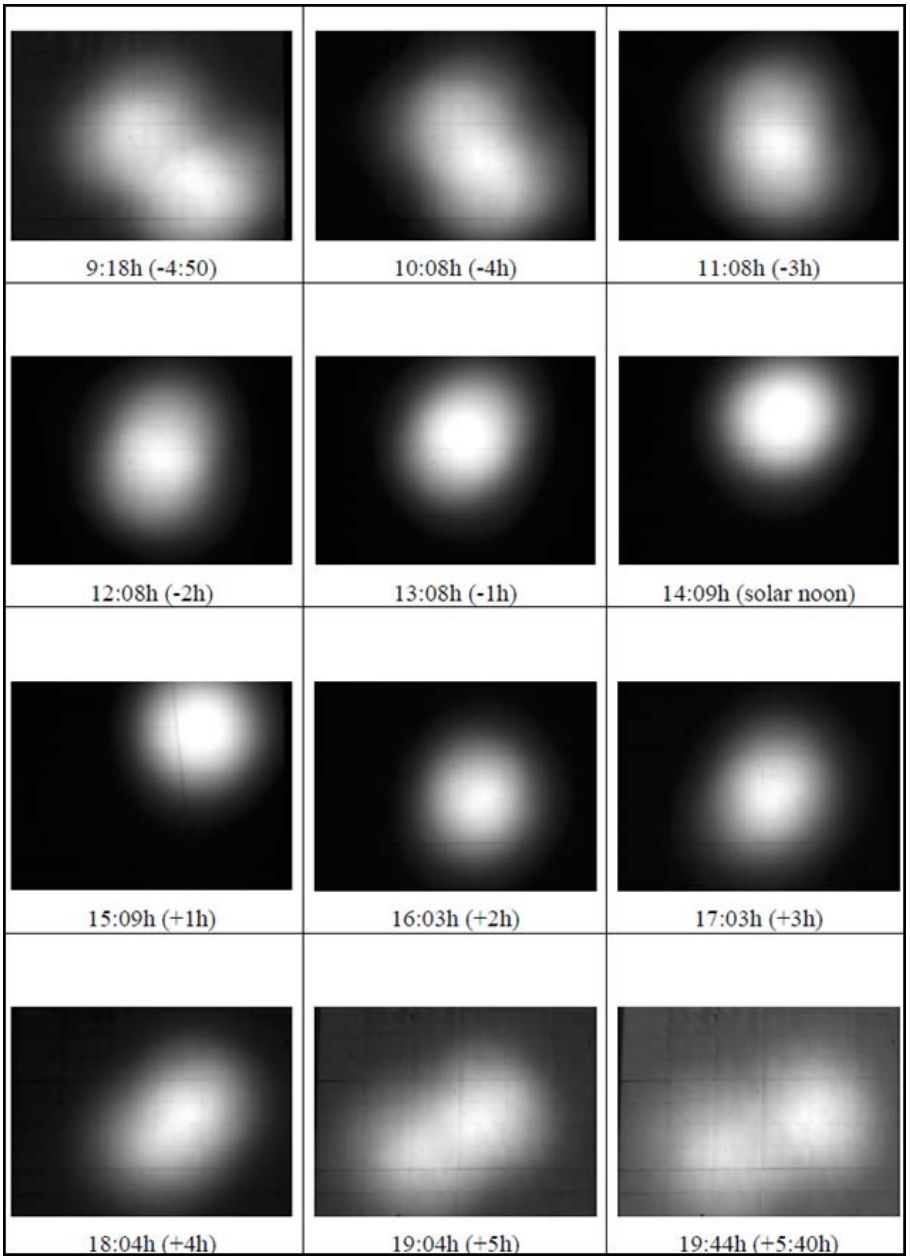

Fig. 4: Split up of focal spot due to gravity for early morning and late afternoon for canting at solar noon caused by too flexible torque tube (Ulmer, 1998)

Teufel et al. (2008) investigated the impact of gravity and wind loads on the annual energy yield. It was found that gravity can have a significant impact on optical losses, while wind during operation can usually be neglected. The reasons for the low impact of wind on the optical losses are the following:

- In operation, only the heliostats at the section of the field perimeter facing the wind (which is a very small portion of the total heliostat field) see significant wind loads while the others are in the wind shadow of the upwind heliostats.
- The maximum loads occur only at certain angles of attack while for other combinations of wind direction and elevation angle the loads are much lower.
- The maximum wind speeds for operation occur quite rarely.
- When heliostats are attacked with significant wind speeds the focal spot will oscillate about a mean position. This will cause only small losses of energy while most of the energy will still hit the receiver. The reason is that the flux intensity is low at the edge of the focal spot. For vibrating heliostats near the tower it is possible no optical loss at all may occur, because their focal spot is small compared to the size of the receiver.
- Heliostats must be designed rigid enough to be able to withstand storms in stow position and to have only low deformation due to gravity during operation. Hence, their deformation in the comparably low wind loads during operation is small.

Therefore, usually the impact of the wind loads on performance during operation can be neglected (for conventional heliostats with sufficient stiffness for all mirror orientations) which simplifies the design process significantly. However, the impact of wind loads on backlash during operation has to be taken into account (see section 2.2.2).

2.2.4 *Survival During Operation and Storm*

The peak wind load coefficients are lowest for the heliostat in stow position (i.e. a horizontal mirror panel) (Peterka and Derickson, 1992). However, these have to be combined with the highest wind speeds occurring during storms. Whether the different wind load components reach their highest values during operation or during storm in stow position depends on the maximum operational wind speed, the highest assumed storm wind speed and their corresponding wind load coefficients. As an example, the peak wind loads on a 30m² heliostat are calculated.

Wind and solar irradiation data (DNI) of Almeria, Spain, were analysed to define the highest wind speed for which the heliostats still have to be in operation. At times with wind speeds below 10 m/s (at 10 m height) already about 97% of the solar energy is gained. Therefore, a limitation of the operational wind speed to 10 m/s is reasonable. The maximum wind speed

that might occur while the heliostat moves into stow position is assumed to be 15 m/s (Ricklin et al., 2014, Table 1; Emes et al., 2015)). For the maximum wind speed usually the 50 year storm event is assumed (Cooke and Mayne, 1980). A typical value is a peak wind speed of U_{peak} = 40 m/s at 10 m height (NBE-AE-88, 1988, tab. 5.1), (DIN 1055-4, fig. A.1). With the wind load coefficients given by Peterka and Derickson (1992) the main peak wind load components for a heliostat within a field were calculated. The mirror area is A = 30 m², chord length h = 5 m, elevation axis height H = 2.9 m, density of air ρ = 1.25 kg/m³ and gust factor R = 1.6. A vertical mean wind speed profile according to the power law with an exponent of n = 0.15 is assumed. The results are given in Table 1.

Table 1: Peak wind load components on 30m² heliostat (without safety factor) according to Peterka and Derickson (1992) including field factors

wind load component	max. $c_{peak,operation}$	max. load operation	$c_{peak,stow}$	load stow
Drag (F_x)	5.6	6.4 kN	0.6	4.9 kN
Lift (F_z)	3.8	4.3 kN	0.9	7.3 kN
Hinge moment (M_{Hy})	0.6	3.4 kNm	0.2	8.1 kNm
Moment pylon base (M_y)	6.2	20 kNm	1.0	23 kNm
Moment vertical axis (M_z)	0.7	4.0 kNm	0.02	0.8 kNm

The drag force F_x and the moment about the vertical axis M_z reach their highest values during operation while the other wind load components are highest for stow conditions with high storm wind speed. For the dimensioning of heliostats the highest values of each wind load component have to be taken into account.

By strategic orientation of the mirror panels considering the wind conditions, the wind loads can be reduced with almost no additional cost. For example, the heliostat can be tilted about the elevation axis to a favourable orientation with respect to the wind direction during stow and storms (Gong et al., 2012) if the typical local weather conditions allow prediction of the wind direction. Alternatively, heliostats oriented in a position with a high wind load coefficient could go to stow position at lower wind speeds, or move to a slightly tilted orientation to protect other heliostats still in operation.

2.3 Wind Load Driven Heliostat Concepts

The highest loads on the structure occur at storm conditions. At these conditions the heliostats and PV-trackers are horizontally aligned to minimise the surface of wind attack (stow position). The wind loads can be further

reduced or the resistance against them can be increased by the following heliostat design approaches (Pfahl, 2014).

2.3.1 *Encased Solar Trackers*

The most radical way to reduce wind loads and to protect the heliostats from sand and hail is to encase them by light-transmissive material, Fig. 5. Besides a reduced dimensioning this would enable the use of front surface mirrors with higher reflectivity. Drawbacks of the concept are the additional significant reflection at the encasement and the extra material for the light-transmissive material with its support structure.

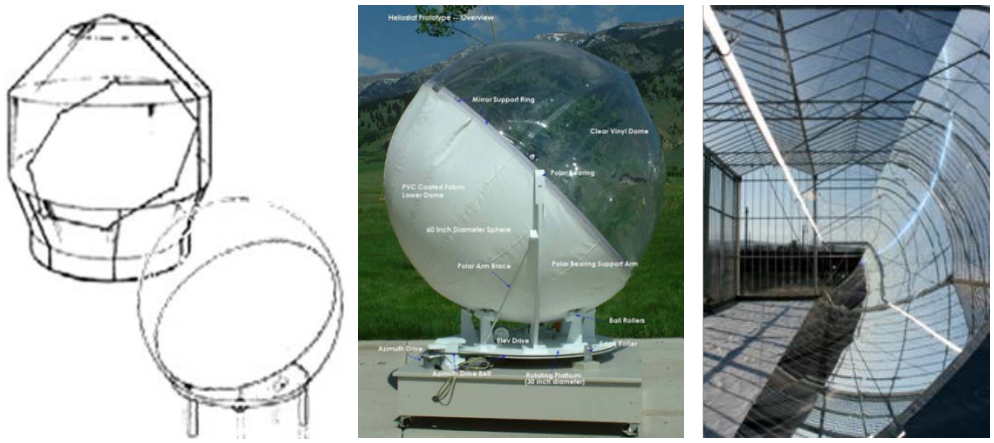

Fig. 5: Left: encased heliostats (Kolb et al., 2007), middle: inflatable heliostat (Sankrithi, 2012), right: parabolic trough in glass house (Glasspoint, 2015)

2.3.2 *Lowering Mirror Panel During Stow*

The loads on the mirror support structure could be reduced by lowering the mirror panel during stow at storm condition. For concepts with the elevation axis at ground level (Fig. 6, left column), the moment about the elevation axis at operation is higher than for conventional heliostats because the forces above and below the elevation axis are less balanced. For usual operational wind speeds, this higher hinge moment is in the same range or even higher than for conventional heliostats in stow position at storm. Furthermore, the moment is increased due to gravity. Therefore, lowering during stow would not lead to cheaper drive systems and also the cost for the mirror panels would not be reduced when the elevation drive is positioned and connected to the panel at its lower end.

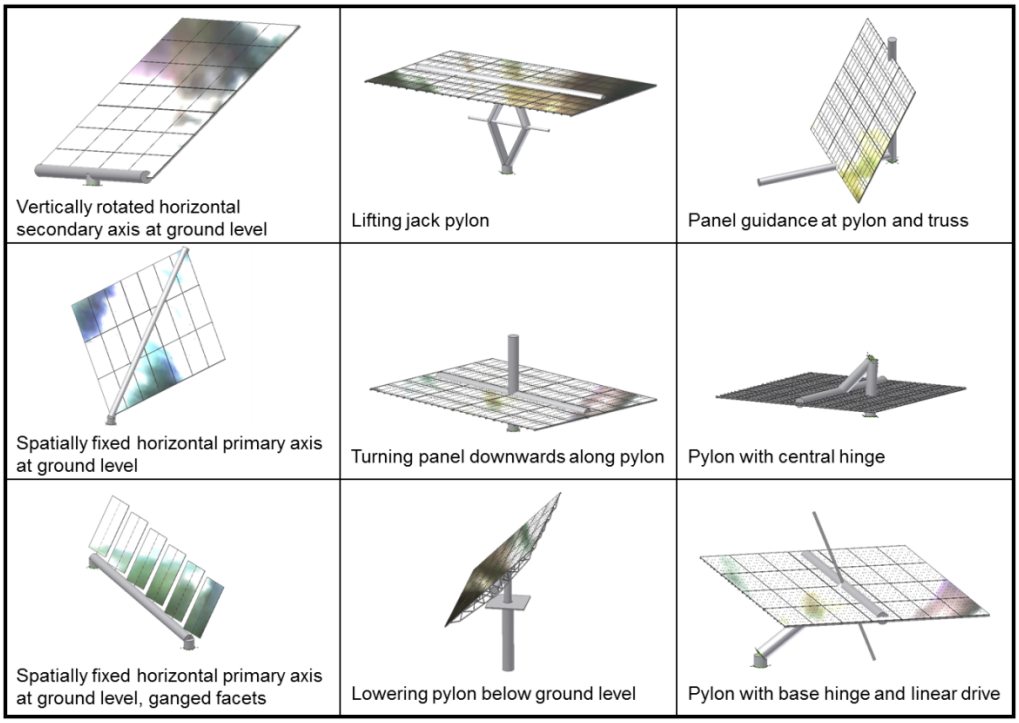

Fig. 6: Approaches for lowering mirror panel at storm condition (Pfahl, 2014)

However, if the elevation drive is connected to the centre of the panel (Fig. 7) low cost drives can be used and the maximum stress in the panel can be reduced by lowering it during stow. The higher moment about the elevation axis during operation due to gravity can be well handled by a spindle drive connected to the panel's centre to achieve a long lever arm. This can be well realised in combination with a carousel carriage with wheel drive (Fig. 7).

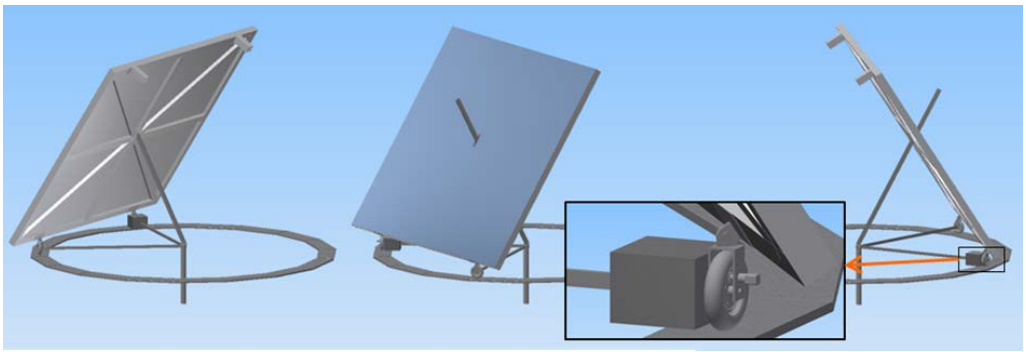

Fig. 7: Azimuthal rotation of a 50m² carousel type heliostat with wheel drive weighted against slippage (DLR) (Pfahl et al., 2017a)

For carousel type heliostats usually ring foundations are used on which the wheels are running to achieve high azimuthal accuracy (Deflandre et al., 1978; Mancini, 2000; Pérez-Rábago et al., 2012). However, such ring foundations are comparably extensive. A ring foundation could be avoided and the wheels of the azimuth drive could run directly on the ground or a simple pavement using a sensor that determines the orientation of the panel independently of the drive mechanism (Fig. 7) (Pfahl et al., 2015b). Such a sensor could be a camera chip with fish eye optics that detects the positions of the centre points of the sun and of the receiver at once. The centre point between these two recognised points is driven to the centre of the imaging space (Fig. 8, right). The normal of the mirror panel (N) is then centred between the vector to the sun (S) and the vector to the receiver (R) so that the rays from the sun hit the receiver (Fig. 8, left) (Pfahl et al., 2008).

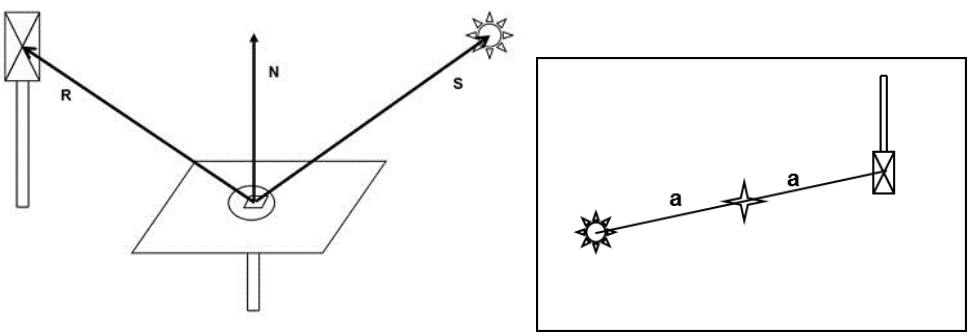

Fig. 8: Sun-target-sensor (Pfahl et al., 2008)

In addition with further innovations described in the following, a lowest heliostat cost of 75$/m² (Pfahl et al., 2017a) is achievable (Pfahl et al., 2017b):

The main component of the heliostat is a monolithic sandwich concentrator which combines the advantages of cantilever-arm and sandwich structures (Siegmeier, 2017). The concept avoids the complexity of canting using only one single facet. Thin glass mirrors sandwiched with a back structure yield high reflectivity and slope accuracy and hence increased optical efficiency. A simple carousel carriage with one actuated wheel realises the azimuth movement. A low cost linear spindle actuator with the drive housed in the spindle passes through the panel's centre and induces the elevation movement. The heliostat uses a closed-loop optical sensor control. Therefore, the carousel carriage may run on a simple track of low accuracy requirements, which consists e.g. of compressed soil or concrete plates stuck together. The carriage is connected to the ground anchor which can be a pile driven into the

ground. A weight of a concrete block or a sand-filled container on the actuated wheel avoids slippage during high wind loads. For stow, the spindle drive pulls the panel to the ground onto the wheels and two extra supports. Thus, the panel is well protected in storm. The reduced wind loads relax requirements and cost for the cantilever-sandwich concentrator (Fig. 9).

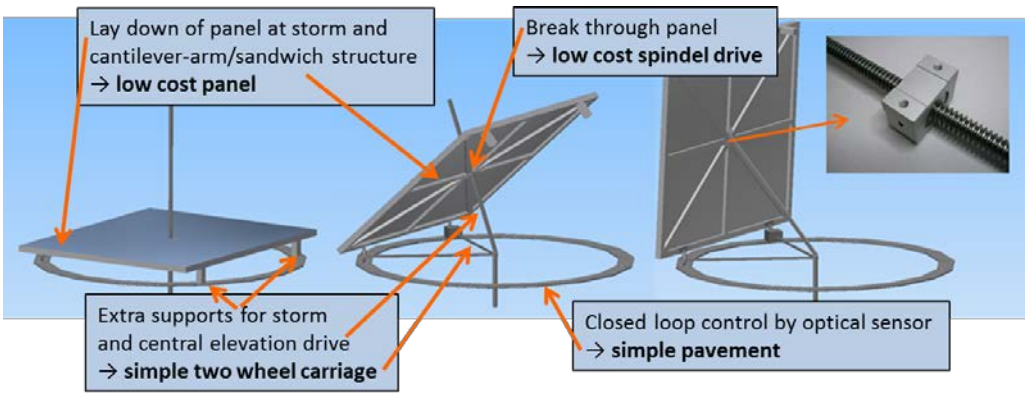

Fig. 9: Heliostat concept for minimum cost of all components (Pfahl et al., 2017b)

The disadvantages of the hitherto solutions, innovations, and resulting cost targets for producing 10 000 heliostats are listed for each part in Table 2.

Table 2: Set of innovations and estimated cost targets for 10 000 heliostats of 50 m² mirror area (Pfahl et al., 2017b)

Part	Disadvantage of hitherto solutions	Innovation (Patent)	Cost [$/m²]
Mirror panel	High wind loads	Lay-down for stow	29
	Many parts	Monolithic cantilever-sandwich panel (Siegmeier et al., 2017)	
	Expensive canting/mold	Low-cost large-size mold (Pfahl et al., 2016)	
Azimuth drive (carousel carriage)	Large, precise foundation ring	Simple pavement or compact ground sufficient due to closed loop control; ground anchor	12
	Extensive 4-wheel carriage	Low cost 2-wheel carriage sufficient due to central elevation drive and panel supports for stow	
	Expensive drive	Weighted wheel drive	
Elevation drive (spindle)	Telescope/scissor-mechanisms expensive	Direct spindle drive through central opening in panel	6
	Drive protection expensive	Drive housed in spindle (Ries, 2017)	
Control/ cabling	High accuracy of mechanical parts required	Closed loop control by optical sensor (Pfahl et al., 2008)	13
Fabrication/ installation/ profit			20
Total cost			**80**

2.3.3 *Locking Device*

For the stow position with its high possible storm wind loads the elevation drive can be unloaded by a locking device. Locking of the elevation can be easily realised using the azimuth drive as actuator (see Fig. 10: for locking the black bolt is positioned by the azimuth drive into the grey cramp). Locking of the azimuth drive is not needed because the loads about the azimuth axis in stow position are small.

Fig. 10: Locking of elevation drive during stow and framework facets, seen at Themis solar power plant heliostats

Presumably, for conventional heliostats no cost reduction can be achieved by locking devices because for the elevation usually linear actuators are used: they are self-locking anyhow and the dimensioning of their spindles is not affected by an additional locking device because buckling is decisive for it which is small at stow position when the spindle is retracted. For drive concepts with increased lever arm like the rim drive concept (see section 2.3.4) locking could be realised at lower cost, because the locking device could use the lever arm of the drives.

2.3.4 *Rim Drive Heliostats*

The lever arm of the actuators is increased for heliostats with rims (Fig. 11) to reduce the torque on the drives and the accuracy requirements to be able to use low cost drives. The loads on the mirror support structure and partly on the bearings are reduced as well.

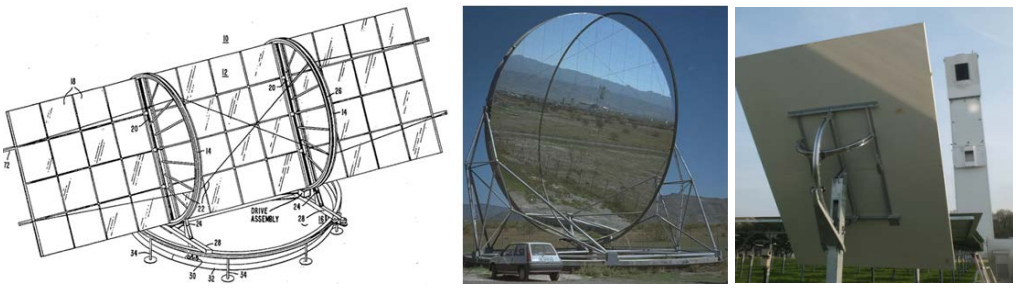

Fig. 11: Rim drive heliostats; left and middle: with vertical primary axis (Sayre, 1980; Weinrebe, 2000); right: with horizontal primary axis

For the rim drive heliostats with vertical (spatially fixed) primary axis shown in Fig. 11, left and middle, extensive foundation is needed. When the first axis is horizontal this can be avoided (Fig. 11, right) (Pfahl, 2011; Pfahl et al., 2013)). Drawback is that an extra guidance for the first rim is needed. By the rims the loads on the drives are reduced. Further more, the loads on the bearings, on the locking device (see section 2.3.3), on the mirror support structure, and on the upper part of the pylon (above the rim) are reduced (Fig. 12).

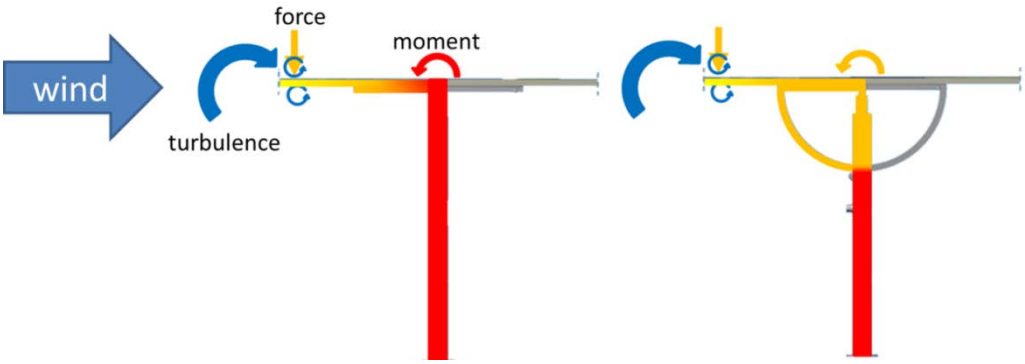

Fig. 12: The turbulence of the approach flow leads to a resulting force near the leading edge of the mirror panel causing a moment at the central bearing. By the rim this moment and thus the loads on drives, mirror support structure, locking device, central bearing, and upper part of the pylon are reduced. The colour change from yellow to red indicates increasing moment.

The rims can be driven via chains, traction sheaves or simply by winch wheels (Fig. 13). Winch wheels and chains (when pretensioned) have almost no backlash (Liedke et al., 2015).

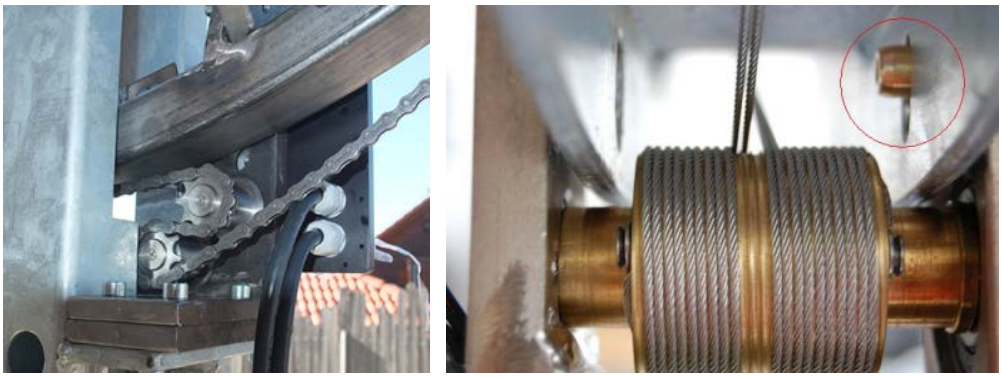

Fig. 13: Rim driven by chain (left) and by winch wheel (right) (with locking bolt (red circle))

The diameter of the sprockets of chain gears should be small to achieve a high gear ratio. Usually, small sprockets lead to fluctuating tension of the chain which reduces its lifetime (Liedke et al., 2015). However, by a special arrangement of the sprockets (Fig. 14, right) the fluctuating tension is avoided (Liedke et al., 2017).

Fig. 14: DLR 9m² rim drive heliostat with chain gear avoiding fluctuating tension of the chain caused by the polygon effect

Assuming e.g. a ten times longer lever arm for the drives, their torque capacity of the drives could be reduced by the same factor to one-tenth (Fig. 15).

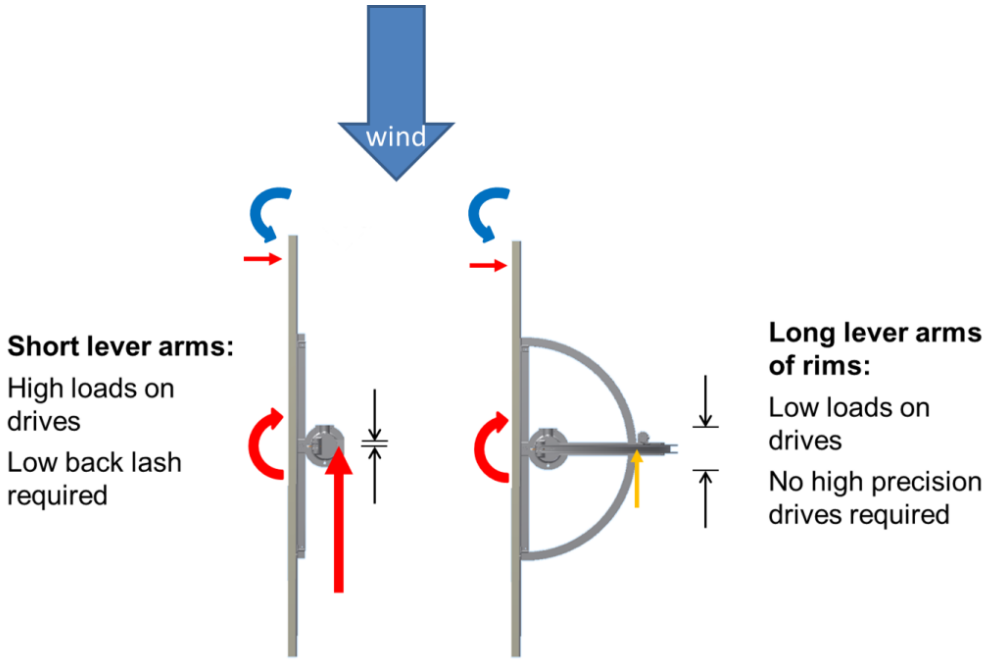

Fig. 15: Reduction of wind loads on drives and reduction of required precision of the drives by rims

A further advantage of the rims is the additional rigidity they provide, which leads to higher natural frequencies (4.7 Hz and 4.9 Hz for the first two modes, Fig. 16, left) and thus to lower dynamic loads (Liedke et al., 2017). The magnification of the hinge moment due to dynamic effects is only 1.4 (Fig. 16, right) compared to conventional structures with values in the range of 2 (Vásquez-Arango et al., 2015; Vásquez-Arango, 2016).

Fig. 16: Vibration behaviour of the heliostat structure at main modes (left and middle), time signals of input and output moment at the elevation axis with amplification factor 1.4 (right) (Vásquez-Arango, 2016)

For heliostats with horizontal primary axis the height of the elevation axis is increased by less than 20% compared to azimuth-elevation tracking because

it is defined by the diagonal of the mirror panel and not only by the chord length. The increased height leads to somewhat increased wind loads compared to an azimuth-elevation heliostat of same area, especially at the pylon base (Pfahl et al., 2017a).

2.3.5 *Spoilers*

The wind loads on the mirror support structure could be reduced by spoilers mounted at the mirror panel (Peterka et al., 1986, Pfahl et al., 2014). Mainly the wind loads at storm are decisive for the dimensioning of the heliostat structure. Therefore, spoilers would have to be designed mainly for the stow position (horizontal mirror panel). Wind tunnel measurements showed a reduction of the hinge moment M_{Hy} of 40% (Pfahl et al., 2014).

Without spoilers, the incident flow with vertical velocity component separates stronger at the frontal edge causing suction on the opposite side of the mirror. The resulting pressure difference between top and bottom of the facet leads to high pressure coefficients (c_p-values) near the frontal edge (Pfahl et al., 2011a; Gong et al., 2013) and therefore to a high overturning moment, see Fig. 17, left. By a fence like structure at the frontal edge separation and thus suction is reduced, see Fig. 17, right.

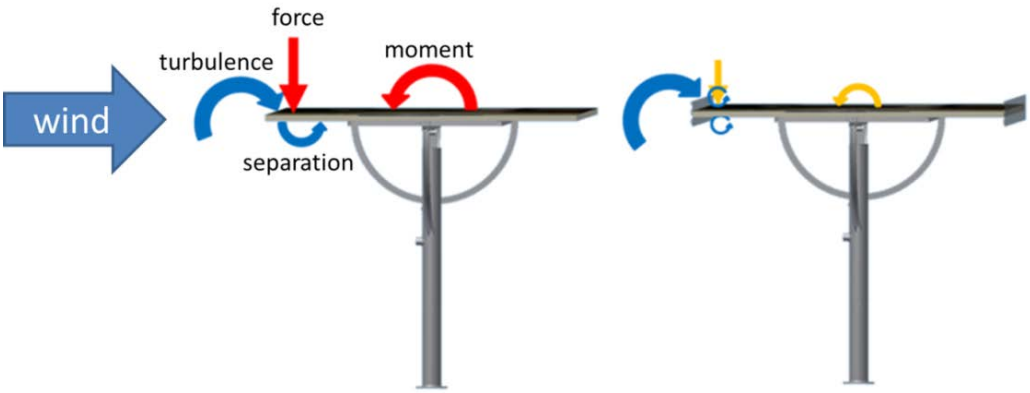

Fig. 17. Left: Turbulence of the approach flow causing separation at the frontal edge leading to high pressure coefficients c_p at the frontal edge and a high overturning moment. Right: Flow manipulators (fence like structures) reducing suction and overturning moment for heliostats in stow position

3 Impact of Heliostat Properties on Wind Loads

3.1 Aspect Ratio

Partly reproduced from [Pfahl, A., Buselmeier, M., Zaschke, M, 2011. "Wind Loads on Heliostats and Photovoltaic Trackers of Various Aspect Ratios". Solar Energy 85, 2185-2201].[1]

Abstract

For the layout of solar trackers the wind loads on the structure have to be known. They can be calculated using wind load coefficients given in the literature. So far, these values are only valid for aspect ratios of the panel (width to height) of about 1.0. Therefore, this study investigates the wind load coefficients for heliostats of aspect ratios between 0.5 and 3.0.

As solar trackers are exposed to the turbulent atmospheric boundary layer, the turbulence of the approach flow has to be modelled. As a reliable method with reasonable cost, wind tunnel measurements were chosen. Solar trackers of 30 m² panel size were investigated with a model scale of 1:20. Wind direction and elevation angle of the panel were varied to investigate especially the constellations for which the highest wind loads are expected (critical load cases). By spires and roughness elements a mean wind speed profile and turbulence intensity profile of the modelled wind according to typical sites for solar trackers were achieved. The loads were measured by a high frequency force balance placed underneath the models. Additionally, measurements of the pressure distribution on a panel with aspect ratio of 1.2 were performed to better understand the effects that lead to the peak values of the wind load coefficients.

Indeed, a significant impact of the aspect ratio was measured. For combinations of elevation angle of the mirror panel and wind direction with possible maximum wind load components the aspect ratio dependencies of the peak wind load coefficients were determined. By these, the peak wind loads on solar trackers of various aspect ratios can be calculated.

Regarding the single solar tracker components the main results are: Higher aspect ratios (width to height) are advantageous for the dimensioning of the foundation, the pylon and the elevation drive but disadvantageous for the azimuth drive.

[1] The BLWT measurements were defined and its results proofed and analysed by the main author. The preparation and execution of the measurements were performed by the co-authors.

Keywords

heliostat, wind load, aspect ratio, PV tracker, central receiver, solar tower plant

Nomenclature

A	[m²]	mirror area
b	[m]	width of mirror panel
c	[-]	wind load coefficient
$c_{Fi,meas}$	[-]	measured wind force coefficient
$c_{Fi,meas,ra=1}$	[-]	measured wind force coefficient for aspect ratio r_a = 1
$c_{Fi,Pet}$	[-]	wind force coefficient according to Peterka and Derickson (1992)
$c_{Mi,meas}$	[-]	measured wind moment coefficient
$c_{Mi,meas,ra=1}$	[-]	measured wind moment coefficient for aspect ratio r_a = 1
$c_{Mi,Pet}$	[-]	wind moment coefficient according to Peterka and Derickson (1992)
c_{Py}	[-]	wind force coefficient of circular cylindrical pylon
D	[m]	diameter of pylon
$d_{ra,Fi}$	[-]	aspect ratio dependency of force
$d_{ra,Mi}$	[m]	aspect ratio dependency of moment (= effective force lever arm)
F	[N]	force caused by wind
$F_{i,meas}$	[N]	measured wind force of aspect ratio r_a
$F_{i,Pet}$	[N]	wind force of according to Peterka and Derickson (1992)
$F_{i,ra}$	[N]	calculated wind force of aspect ratio r_a based on peak measurements with various r_a
F_{xPa}	[N]	drag force of panel
F_{xPy}	[N]	drag force of pylon
h	[m]	height of mirror panel
H	[m]	height of elevation axis
H_P	[m]	height of elevation axis not wind shaded by panel
i		indication of x, y, Hy or z
l	[m]	characteristic lever arm

l_i	[m]	characteristic lever arm of Peterka and Derickson (1992)
M	[Nm]	moment caused by wind
$M_{i,meas}$	[Nm]	measured wind moment at aspect ratio r_a
$M_{i,Pet}$	[Nm]	wind moment according to Peterka and Derickson (1992)
$M_{i,ra}$	[Nm]	calculated wind moment of aspect ratio r_a based on peak measurements with various r_a
n	[-]	exponent of power law describing vertical wind speed profile
p_{dyn}	[N/m²]	dynamic pressure
R	[-]	gust factor (peak wind speed / mean wind speed, for 2-3 sec. gusts and 18% turbulence intensity R = 1.6)
$r_a=b/h$	[-]	aspect ratio width to height of mirror panel
v	[m/s]	mean wind speed at elevation axis height H
v_{ref}	[m/s]	mean wind speed at mean wind tunnel height (100 cm)
$v(z)$	[m/s]	mean wind speed at height z
x	[m]	coordinate, horizontal, perpendicular to elevation axis, at base
y	[m]	coordinate, horizontal, along elevation axis, at base
z	[m]	coordinate, vertical upwards (azimuth axis); height
z_{ref}	[m]	reference height
α	[°]	elevation angle of mirror panel, 0° when horizontal
β	[°]	wind direction, 0° when perpendicular to elevation axis
ρ	[kg/m³]	density of air

3.1.1 *Introduction*

As photovoltaic (PV) and solar thermal power plants are getting more and more important for the worldwide energy supply, heliostats of central receiver power plants and PV trackers are built in rising quantities. The higher the quantities the more significant is a cost effective design of the structure. For their dimensioning the wind loads are decisive and therefore should be known as precisely as possible.

An important characteristic of solar trackers is the aspect ratio of the panel. For the determination of the aspect ratio two contrary aims have to be taken into account: First, to reduce the height of the solar tracker and thus the average wind speed, wide panels would be favourable. Second, to avoid long lever arms and for to reach high field densities (assuming that the distance between the solar trackers is determined by the diagonal of the panel), square panels would be best. From investigations of simple plates it is known that the aspect ratio can have a significant influence on the wind loads (Sakamoto and Arie, 1983). Therefore, the impact of the aspect ratio concerning wind loads has to be known for a cost effective design of solar trackers.

Peterka and Derickson (1992) have extensively investigated the wind loads on heliostats through boundary layer wind tunnel (BLWT) tests. By their report, the wind load coefficients for the main wind load components are available. However, they explicitly remark that the tested heliostats were nearly square in shape and that the impact of the aspect ratio is not known from the tests leading to their report (Peterka and Derickson, 1992, p. 13). More recent publications are based also only on heliostats with aspect ratio around 1 (Wang and Li, 2008; Wu et al., 2010). Therefore, the aspect ratios (width/height) 0.5, 1.0, 1.2, 1.5, 2.0 and 3.0 (see Fig. 18) were investigated. Although aspect ratios of 0.5 and 3.0 are usually not chosen for solar trackers, these values were investigated to achieve more pronounced results which help to understand more clearly the effects that are causing the aspect ratio dependencies.

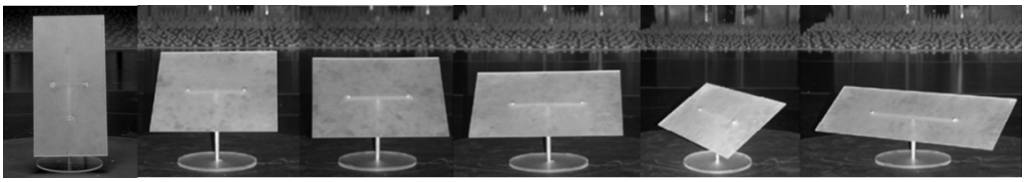

Fig. 18: Heliostat models with aspect ratio 0.5, 1.0, 1.2, 1.5, 2.0 and 3.0

Background of the investigations was the development of a heliostat with hydraulic drive and a mirror area of 30m² (HydroHelio^{TM}). Prior to the present investigation it was not possible to decide in a profound way which aspect ratio for the mirror panel should be chosen.

For uniformity reasons, the coordinate system and the characteristic lengths are according to (Peterka and Derickson, 1992, p. 11), see Fig. 19.

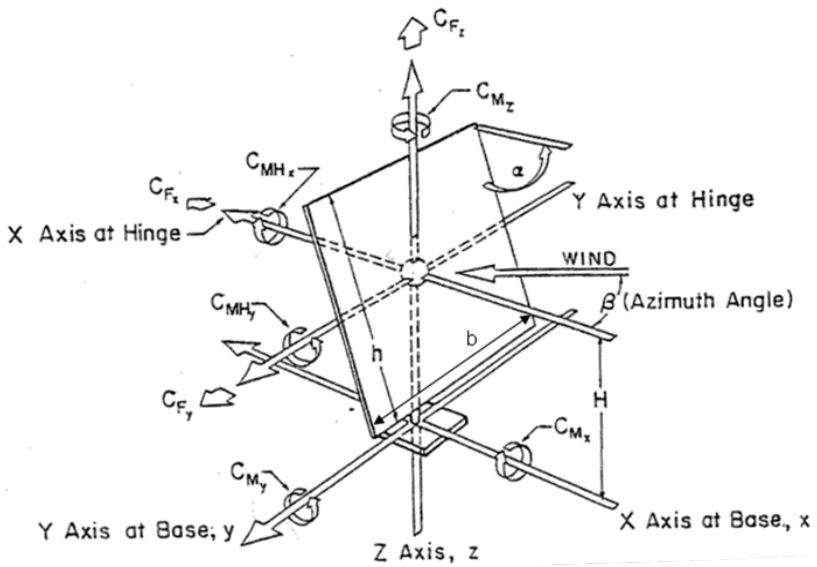

Fig. 19: Coordinate system and characteristic lengths (Peterka and Derickson, 1992)

3.1.2 *Method*

3.1.2.1 Selection of method

The wind loads could be determined at real scale heliostat models exposed to atmospheric wind. However, the low reproducibility of the wind conditions would make it almost impossible to compare the results of heliostats with different aspect ratio. With numerical simulations (computational fluid dynamics, CFD) and with physical wind tunnel tests using appropriate model scales this problem can be avoided.

For the layout of solar trackers the peak values of the wind loads are decisive. Therefore, CFD is not very suitable because especially the peak values of the wind load components are highly sensitive to turbulence (gustiness) in the attacking wind, as Peterka and Derickson (1992, p. 2) observed in their wind tunnel tests and which is also known for other structures (Hucho, 2002, section 3.7). Hence, it is important that the turbulence of the attacking wind is appropriately modelled. For CFD this means that a turbulent inflow must be generated. Fröhlich (2006, p. 207 et seqq.) gives an overview of possible methods. A method for synthetic turbulence generation that is already implemented in commercial tools is the vortex method (Sergent, 2002; Mathey et al. 2006). Furthermore, it must be ensured that the turbulence does not dissipate before reaching the investigated body. The common RANS (Reynolds averaged Navier-Stokes) simulations do not explicitly resolve the

turbulence structures in the flow (Fröhlich, 2006, p. 16 et seqq.). The used turbulence models account for this only by a modelling process. Thus, only simulation approaches at which at least the largest turbulence structures are actually resolved are suitable for determining wind loads. This is especially the case for Large Eddy Simulations (LES) or Detached Eddy Simulations (DES) (Spalart, 2000). Furthermore, it is necessary to run the simulation for a sufficient long time period to be able to apply extreme value statistics to determine the peak values of the wind load coefficients (Cook and Mayne 1980). In combination with the fine grid which is necessary for LES or DES this would be difficult to achieve in view of a very large demand of computational power and time.

For some cases it is possible to determine the peak loads by just multiplying the loads gained with attacking wind of (almost) no turbulence (measured or calculated) with the square of the gust factor R corresponding to the turbulence intensity of the site (for a typical solar site turbulence intensity of 18% R = 1.6) (Peterka and Derickson, 1992, p. 5 et seqq.). However, this approach does not work well for cases in which a wind load component is sensitive – first – to a change of the wind direction or – second – to an unequal pressure distribution on the mirror panel.

The first is the case for example for the hinge moment M_{Hy} at stow position (horizontal mirror panel). The mean value for this position is near zero while the peak value caused by a temporarily sideward wind attack (caused by a vortex passing the panel) is not. Peterka and Derickson (1992, p. 18) measured a ratio of peak to mean value of 10 for this case while R^2 is only 2.56. Also mean values can be sensitive to the turbulence intensity of the attacking wind (Peterka and Derickson, 1992, p. 13 et seqq.). This is confirmed by the comparison of CFD simulation and wind tunnel measurement of Wu and Wang (2008) at which significant discrepancies occurred.

The second is the case for example for M_{Hy} at upright mirror orientation and frontal wind attack. For a low-turbulence approach flow the force on the upper and lower part of the mirror panel is relatively equal which causes only a low moment about the elevation axis. However, for realistic turbulent approach flows temporarily unequal pressure distributions are causing peak hinge moments that are in the measurements of Peterka and Derickson (1992, p. 18) 12 times and in this study 9 times higher than the mean loads. Also in this case, CFD or wind tunnel measurements with attacking wind of no or low turbulence in combination with the gust factor approach would not lead to realistic results for the peak values.

For these reasons, boundary layer wind tunnel tests were chosen to determine the impact of the aspect ratio on the wind load components. This way, the wind conditions can be defined reproducible at comparably reasonable cost.

3.1.2.2 Specifications

The mirror area (A = 30 m²) and the distance of the mirror panel to the ground at upright orientation (H - 1/2h = 0.4 m) was the same for all aspect ratios. This means that the elevation axis height H decreases with increasing aspect ratio. For this reason, the wind load coefficients are calculated on the base of the wind speed v at elevation axis height H to obtain better comparability. Especially for the overturning moments M_x and M_y, H is of influence. For the other wind load components H is of much smaller impact. Nevertheless, for ratios of ground distance to mirror area (H - 1/2h) / A much different to the value of this study the results might not be valid.

In reality, the mirror panel is divided by thin gaps between the facets but these are of negligible impact on the wind loads as shown by Wu et al. (2010). The scale of the models is 1:20. Exemplarily a drawing of the model with aspect ratio 1.2 is given by Fig. 20.

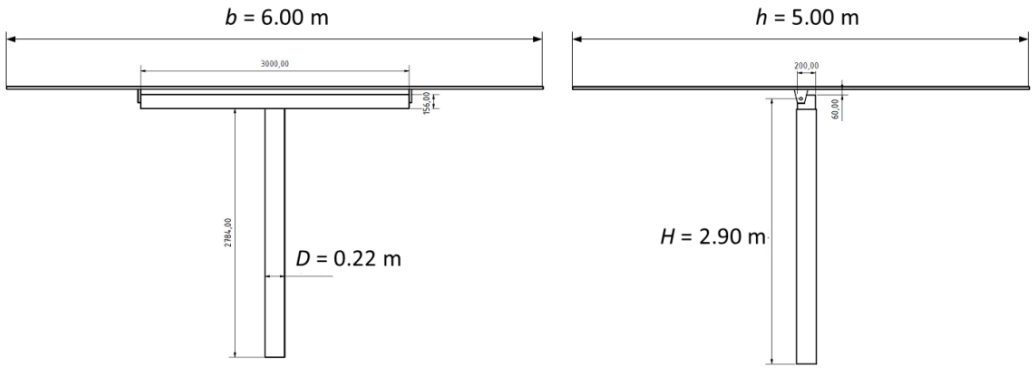

Fig. 20: Sketch of heliostat model with aspect ratio 1.2; front view (left) and side view along elevation axis (right)

The wind load components vary with the elevation of the panel α and with the wind direction β. The combinations of α and β that lead to the maximum values of the wind load components have to be considered for the dimensioning of solar trackers (see section 2.2.4 (Peterka and Derickson, 1992, p. 17 et seq.)). These relevant load cases were investigated (see Table 3).

Table 3: Critical load cases of combinations of α and β with possible maximum wind load components

critical load case	α	β	wind load components with possible maximum value
1	90°	0°	F_x, M_y
2	30°	0°	F_z, M_{Hy}
3	90°	60°	M_z
4	0°	0°	F_x, F_z, M_{Hy}, M_y
5	0°	90°	F_y, M_x

3.1.2.3 Experimental Procedure

3.1.2.3.1 Similarity

In order to obtain realistic wind loads by means of BLWT tests the most significant model laws have to be accounted for. These are mainly the geometric similarity of the model and the dynamic similarity of the approach flow (Plate, 1982).

Wind events can be classified into those that are mainly caused by large-scale meteorological changes and appear usually in periods down to one hour and those that are caused mainly by upwind obstacles and ground roughness that disturb the wind and appear in periods up to 10 min. The range between 10 min and 1 h is the so called "spectral gap" with only rare wind events (Cook and Mayne, 1979; Van der Hoven, 1957).

The wind events caused by upwind obstacles and ground roughness in interaction with the investigated structure lead to a certain wind loading. The loads would have to be measured in a time interval of minimum 10 min (at real scale) to capture all possible wind events. For the determination in wind tunnels, these fluctuations must be modelled according to the length scale. Also the needed time for the measurements scales with the length scale. Therefore, for example for the used length scale of 1:20 and accounting for the minimum 10 min time interval, a duration of every measurement of 30 seconds would be necessary.

Unfortunately, the dimensions of the wind tunnel are far too small to simulate vortex structures of a size that corresponds to such duration. In section 5.2 the consequences of this limitation are investigated.

For a repeated measurement, the maximum peak value could be higher than the maximum value of the first measurement. Hence, the more often the 10 min measurement is repeated, the higher is the most probable maximum peak value of all experiments. By extreme value statistics (Cooke and Mayne, 1980) it is possible to determine the maximum peak value that would appear within an arbitrary period of time (see Appendix A). In building codes usually a period of 50 years is used as a standard. Therefore, the peak wind load coefficients given here are the ones that together with the expected maximum 10 min mean wind speed within 50 years lead to the 50 years peak wind loads (“50 year event”). Additionally, a safety factor has to be applied to achieve an acceptable failure rate. For example, for buildings the failure rate must be of course extremely low while it can be higher for heliostat fields.

With the geometric scale of 1:20 of the wind tunnel models it was ensured that the models were big enough in order to deliver highly resolved and accurate measurement data but were still of an appropriate size in order to avoid any wind tunnel blockage that could influence the measurements (the wind tunnel cross section is 1.80 m x 2.00 m, the resulting blockage ratio is 2%). The models were equipped with a mechanism allowing to adjust their elevation angle and mounted on a turntable which made it possible to rotate them in order to model the different wind directions.

The similarity of the approach flow depends crucially on the upstream surface characteristics. For the present case it is appropriate not to consider any individual obstacles like buildings or vegetation in the vicinity of the heliostat but to characterise the surrounding landscape by its surface roughness. This is reasonable because the results of the investigation should be as general as possible and not be limited to one particular case. In the laboratory, the roughness is realised by placing vortex generators (spires) at the entrance of the wind tunnel and roughness elements along the flow upwind of the model. A schematic section through the BLWT used for the present investigation is given by Fig. 21.

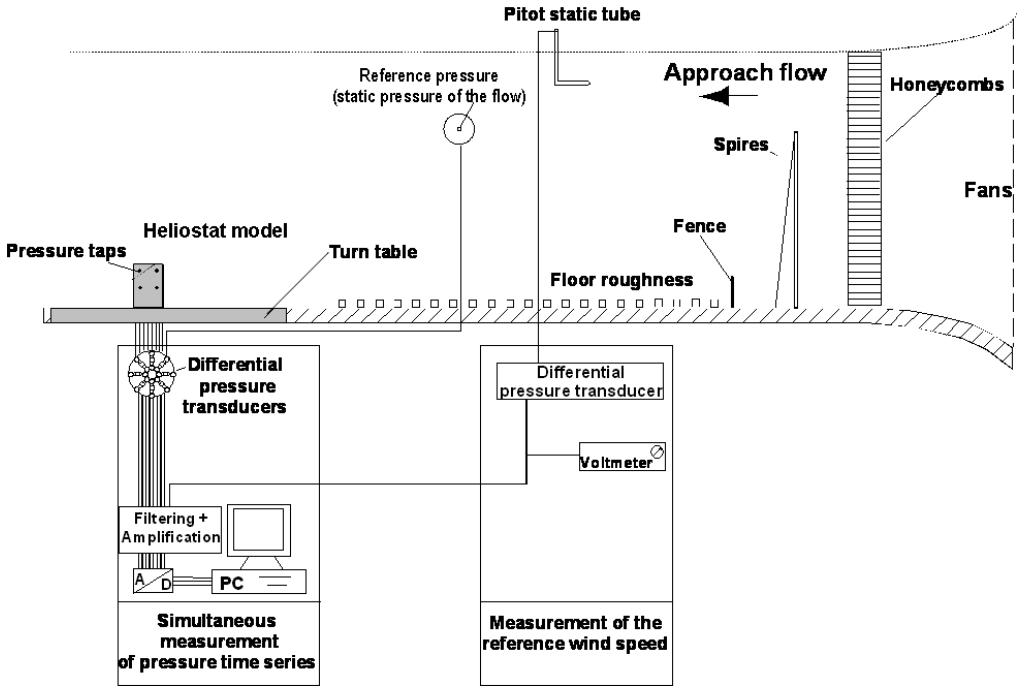

Fig. 21: Schematic section through the atmospheric boundary layer wind tunnel used for the present investigation.

In wind engineering, it is common practice to describe the vertical distribution of mean wind speed *v(z)* using the power law approach (see equation (3.1.1) and Fig. 22, left). The exponent *n* is a function of the upwind surface roughness.

$$\frac{v(z)}{v(z_{ref})} = \left(\frac{z}{z_{ref}} \right)^{n} \qquad (3.1.1)$$

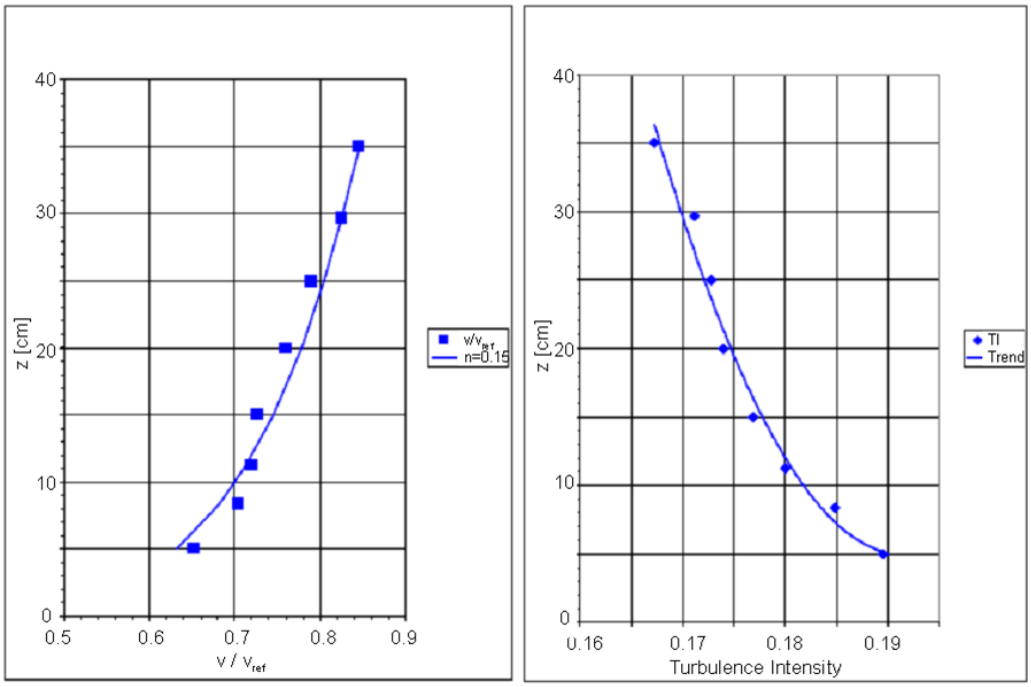

Fig. 22: Vertical mean wind speed profile (left) and vertical turbulence intensity profile (right) of the simulated atmospheric boundary layer

The vertical mean wind speed profile (Fig. 22, left) was measured in the middle of the empty turntable. Presumably, two different boundary layers separated near a height of 12.5 cm lead to this profile. Besides the vertical mean wind speed profile, the roughness also determines the turbulence characteristics of the boundary layer flow. Typical surroundings of solar power plants are open countries with single trees and buildings. The corresponding value for n of the power law approach is n = 0.15 (Peterka and Derickson, 1992, p. 6). Therefore, it was decided to adjust the roughness elements and vortex generators in the wind tunnel in order to reproduce the corresponding profile. The distance between the vortex generators and the model test section is about 8 meter. This length is sufficient to achieve a sufficient boundary layer thickness of more than five heliostat heights.

The main turbulence characteristic is the turbulence intensity which is defined as the standard deviation of the wind speed fluctuations around the mean wind speed. The elevation axis of the models varies between 0.10 m (for r_a = 3) and 0.22 m (for r_a = 0.5) at model scale. At this height range, a turbulence intensity between 17.3% and 18.2% was measured in the wind tunnel (Fig. 22, right). It was assumed that at full scale a similar difference occurs and was therefore accepted.

A further modelling requirement is to ensure equality of the Reynolds numbers at reduced scale and at full scale. Especially for curved shapes like circular cylinders or spheres or for the flow through openings, the Reynolds number similarity is important because for these cases the Reynolds number influences the position of the separation point and thus the wind induced pressure distribution. However, for sharp edged bodies, the separation point (or line) is defined by the edges and therefore is fixed and independent of the Reynolds number for the relevant wind speed range (Plate, 1982). By wind tunnel measurements at a high pressure wind tunnel with a wide variability of the Reynolds number, it could be shown that the dependency of the wind load coefficients of heliostats on the Reynolds number is negligible even for solar trackers with circular cylindrical torque tube which is exposed to the wind at horizontal panel at stow position. This will be shown later in Chapter 5, section 5.1.

3.1.2.3.2 Force balance

For the determination of the wind force coefficients a high frequency force balance was used. With it, the bearing forces at the pylon feet of the model can be measured directly. The fluctuating and the time-averaged reaction forces can be determined. To exclude distortions of the fluctuating load reactions, it is important that the resonance frequency of the force balance in the three force directions is higher than the frequency of the actuating force. If the range of the frequencies of the actuating force would be in the range of the resonance frequency of the balance resonance would occur which would lead to too high measuring results. The force balance therefore must be as stiff as possible with high resonance frequency. Usually, it is sufficient to adjust the balance in a frequency range higher 100 Hz. The fixing of the wind tunnel model on the measuring table was realised with vacuum technique.

With the force balance it is possible to determine the forces and moments at the pylon feet. By this, the hinge moment at elevation axis height cannot be directly measured. However, it is possible to estimate it by equation (3.1.2) with sufficient accuracy assuming the following: The total drag force (measured at the pylon feet) F_x is composed by the drag force of the pylon F_{xPy} and by the drag force of the panel F_{xPa} (equation (3.1.5)). The drag force of the pylon can be calculated using the load coefficient for circular cylinders c_{Py} = 0.7 (equation (3.1.3)). Thereby, only the part of the pylon which is not wind protected by the panel (H_P) has to be considered (equation (3.1.4)).

$$M_{Hy} = M_y - F_{xPa} \cdot H - F_{xPy} \cdot \frac{H_P}{2} \tag{3.1.2}$$

with

$$F_{xPy} = c_{Py} \cdot \frac{\rho}{2} \cdot v^2 \cdot H_P \cdot D \tag{3.1.3}$$

$$H_P = H - \sin(\alpha) \cdot \frac{h}{2} \tag{3.1.4}$$

$$F_{xPa} = F_x - F_{xPy} \tag{3.1.5}$$

3.1.2.3.3 Pressure measurements

In addition to the measurements with the force balance, pressure measurements were performed for a heliostat with the most common aspect ratio of 1.2 (Fig. 23). The corresponding model was constructed using three-dimensional printing technologies. The panel was built as a pressure measurement module. The mean and the fluctuating wind pressure on front and back side of the panel could be measured directly as a function of wind direction and elevation angle. Disturbance of the flow by the pressure tubes could not be avoided but was assumed to be low enough that by the measured pressure distributions the results of the force balance can be explained. The measurements were performed simultaneously on front and back side and throughout the entire surface area of the panel in order to be able to determine the differential pressures. The resulting dimensionless wind pressure coefficients (c_p-values) describe the relation between the measured pressures acting on the panel and the dynamic pressure of the undisturbed flow at elevation axis height *H*.

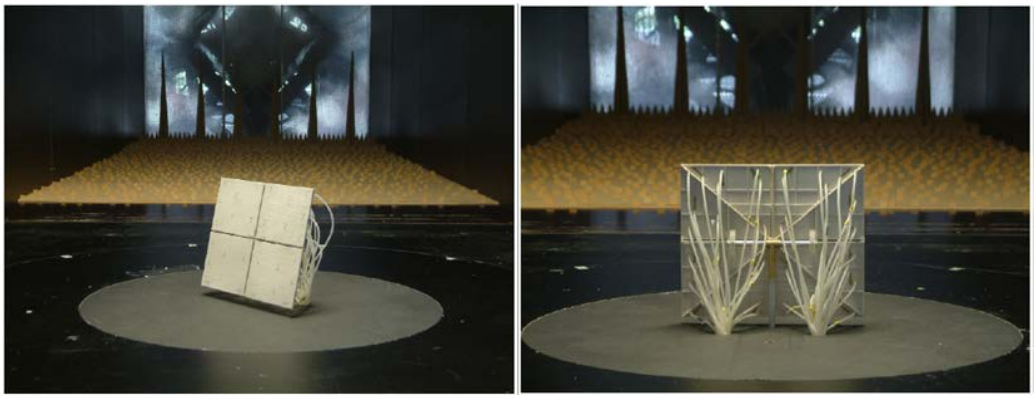

Fig. 23: BLWT model for pressure measurements

On each side of the panel 28 taps for the pressure measurements were positioned, typically 1 mm in diameter. The mirror panel consists of four facets “A” – “D” (Fig. 24). Each facet was divided into seven sections with one pressure tap delivering an approximately representative value for the corresponding section.

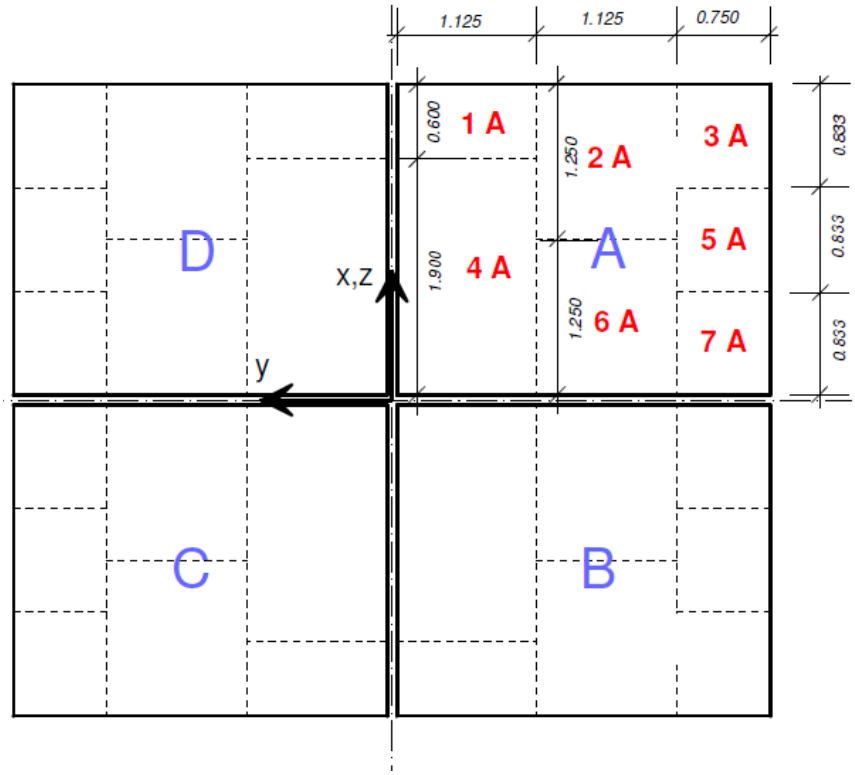

Fig. 24: Sections of pressure measurements at four facets “A” – “D”; full scale dimensions in meter

For facet “A” the positions of the measuring points are given in Table 4. The positions of the measuring points of the other sections follow symmetry.

Table 4: Positions of measuring points for facet A

measuring point	x [m]	y[m]
1 A	2.30	-0.50
2 A	1.90	-1.80
3 A	2.30	-2.75
4 A	0.90	-0.50
5 A	1.40	-2.75
6 A	0.90	-1.80
7 A	0.50	-2.75

For load cases for which a symmetric pressure distribution can be assumed, only half of the panel was measured to reduce the amount of pressure tubes and thus the distortion of the flow.

3.1.2.3.4 Definitions of Wind Load Coefficients

The following laws lead to the definitions of the wind load coefficients:

$$F \sim p_{dyn} = \frac{\rho}{2} \cdot v^2 \tag{3.1.6}$$

$$F \sim A \tag{3.1.7}$$

$$M \sim F \tag{3.1.8}$$

$$M \sim l \tag{3.1.9}$$

According to equations (3.1.6) - (3.1.9) Peterka and Derickson (1992, p. 10) defined the wind load component coefficients as follows:

$$F_{i,Pet} = c_{Fi,Pet} \cdot \frac{\rho}{2} \cdot v^2 \cdot A \tag{3.1.10}$$

$$M_{i,Pet} = c_{Mi,Pet} \cdot \frac{\rho}{2} \cdot v^2 \cdot A \cdot l_i \tag{3.1.11}$$

with i indicating the coordinate direction x, y or z and l_i indicating a characteristic length ($l_{Mx} = l_{My} = H$; $l_{MHy} = l_{Mz} = h$).

For the calculation of both the mean and the peak wind loads the mean speed at elevation axis height is used. Thus, the differences between mean and peak wind loads are directly given by the wind load coefficients. The wind load coefficients given by Peterka and Derickson (1992) are intended to be valid only for r_a =1.

To be able to compare the wind load coefficients of the measurements of this study with the ones of Peterka and Derickson (1992) they are defined equally:

$$F_{i,meas} = c_{Fi,meas} \cdot \frac{\rho}{2} \cdot v^2 \cdot A \quad (3.1.12)$$

$$M_{i,meas} = c_{Mi,meas} \cdot \frac{\rho}{2} \cdot v^2 \cdot A \cdot l_i \quad (3.1.13)$$

with l_i indicating the same characteristic lengths as used in the definitions of Peterka and Derickson (1992).

By a fitting of the measured peak values by an exponential function the aspect ratio dependencies are obtained. With them, the peak wind loads can be calculated for various aspect ratios with the wind load coefficients for aspect ratio r_a =1:

$$F_{i,ra} = c_{Fi,meas,ra=1} \cdot \frac{\rho}{2} \cdot v^2 \cdot A \cdot d_{ra,Fi} \quad (3.1.14)$$

$$M_{i,ra} = c_{Mi,meas,ra=1} \cdot \frac{\rho}{2} \cdot v^2 \cdot A \cdot d_{ra,Mi} \quad (3.1.15)$$

3.1.3 *Results and Discussion*

Most of the following graphs of the measured peak wind load coefficients are quite irregular. The reason is the general uncertainty of peak value measurements. The aspect ratio dependencies were gained only by the measured peak values because for the dimensioning of heliostats mainly the peak values are relevant. They are also applied to the mean values to prove their general validity.

3.1.3.1 F_x – horizontal force perpendicular to elevation axis (drag)

At load case 1 (α = 90°, β = 0°) the heliostat is similar to a vertical flat plate with a gap of 0.4 m to the ground. For free standing plates on ground, the wind force coefficient decreases with increasing aspect ratio for aspect ratios < 5 (Sakamoto and Arie, 1983; Letchford and Holmes, 1994). (For slightly lifted plates this effect is reduced by only a small portion (ESDU 89050, figure 7c; Leder and Geropp, 1993). In the present study, an even more pronounced reduction of F_x for increasing aspect ratio was measured (Fig. 25).

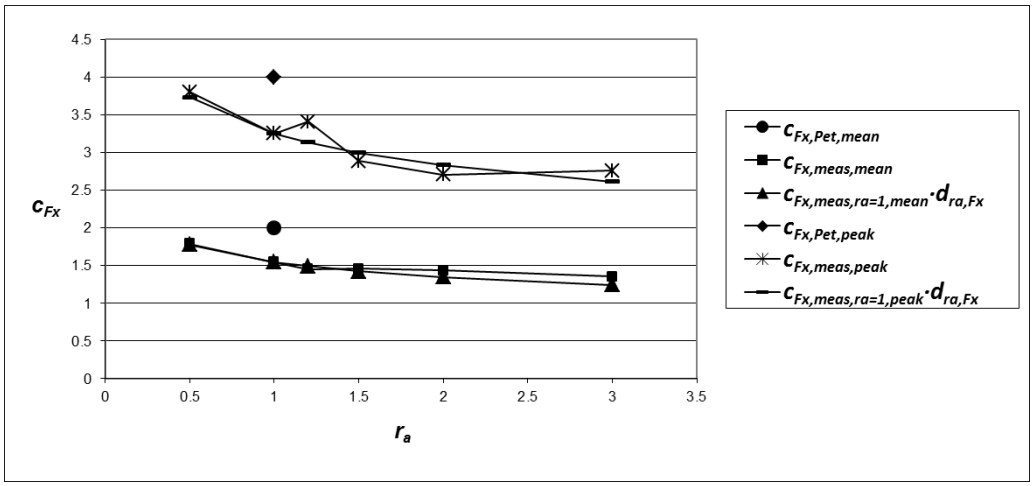

Fig. 25: Aspect ratio dependency of c_{Fx} at load case 1

For load cases 2 and 3 the projected mirror area is smaller than for load case 1 and therefore also the drag force. However, for high storm wind speeds and relatively low maximum wind speed for which the heliostat is in operation, the maximum drag force could occur during storms. At load case 4, the panel is horizontal (α = 0°, β = 0°) in stow position which means that the cross bar is directly exposed to the wind. The cross bar increases with increasing aspect ratio as well as the frontal edge of the panel (Fig. 20, left). Therefore, F_x increases with increasing aspect ratio (Fig. 26). The calculated mean values are not in good agreement with the measured ones. The reason for it is not clear.

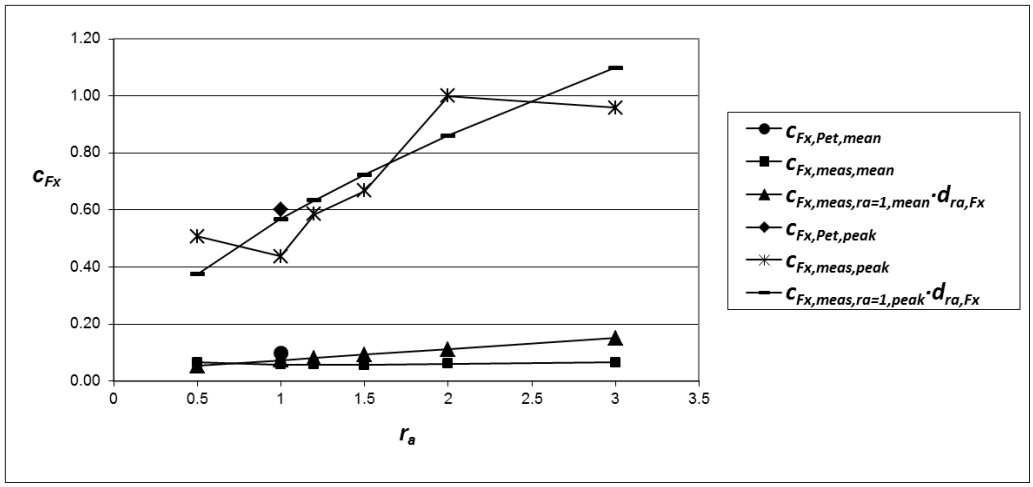

Fig. 26: Aspect ratio dependency of c_{Fx} at load case 4

3.1.3.2 F_y – horizontal force along elevation axis

The values of F_y at load case 5 (α = 0°, β = 90°) decrease (Fig. 27) because the area of attack (pylon and frontal edge of the panel) decrease with increasing aspect ratio (Fig. 20, right).

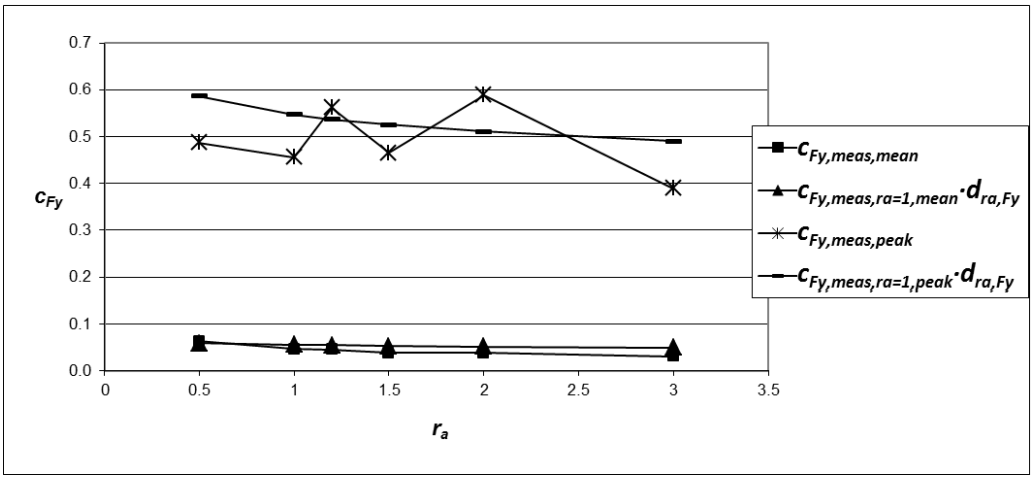

Fig. 27: Aspect ratio dependency of c_{Fy} at load case 5

3.1.3.3 F_z – vertical force (lift)

The absolute values of F_z at load case 2 decrease slightly with increasing aspect ratio (Fig. 28). The reason might be that for bigger width b the gusts of maximal wind speed cover a smaller portion of the mirror panel.

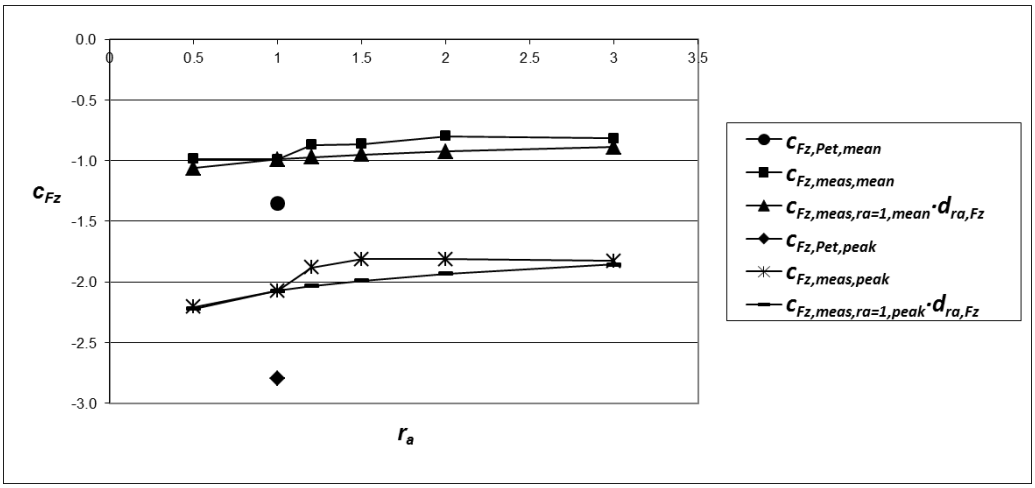

Fig. 28: Aspect ratio dependency of c_{Fz} at load case 2

For load case 4, the mean wind has no component normal to the mirror panel. Therefore, the mean values of F_z are very low (Fig. 29). The peak values are

caused by turbulent gusts which lead to temporarily sideward wind attacks causing the high pressure values at the frontal edge (Fig. 30, left). Since this edge increases with increasing aspect ratio, F_z increases as well. The high differences with the results from Peterka and Derickson (1992) particularly for this case are not clear.

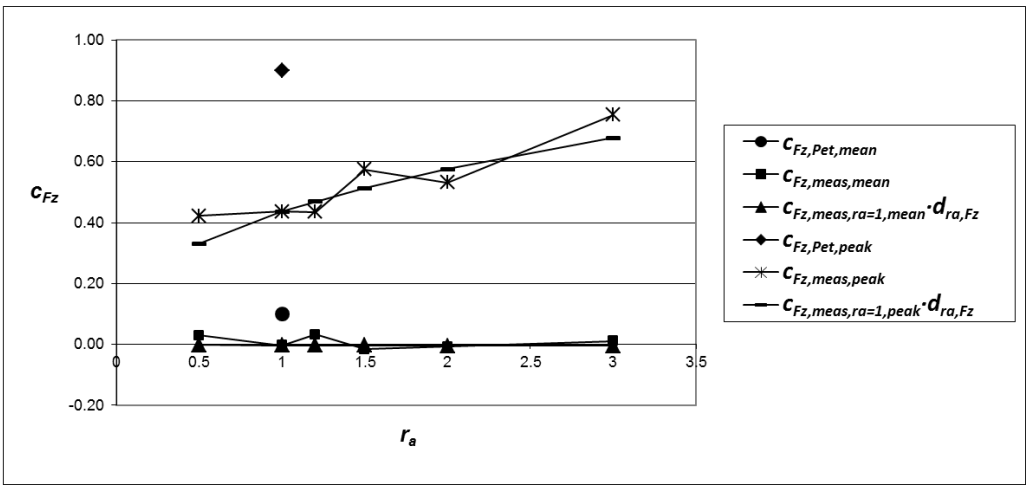

Fig. 29: Aspect ratio dependency of c_{Fz} at load case 4

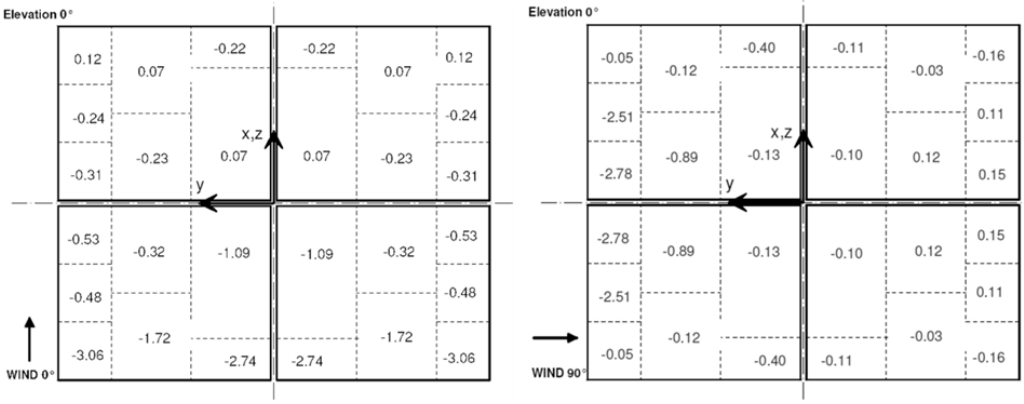

Fig. 30: Pressure coefficient distribution for aspect ratio 1.2 at point in time with peak F_z with α = 0° and β = 0° (load case 4) (left) and peak M_x with α = 0° and β = 90° (load case 5) (right)

3.1.3.4 M_x - moment at pylon base about x axis

Similar to F_z, the peak values of M_x are caused by a zone of high pressure at the frontal edge of the panel (Fig. 30, right). For the wind moments, this leads also to an almost constant aspect ratio dependency (which will be discussed in section 3.1.3.8) for load case 5 (Fig. 31). By Peterka and Derickson (1992)

the definition of M_x is given but no values of the coefficient. Therefore, they are missing in the diagram.

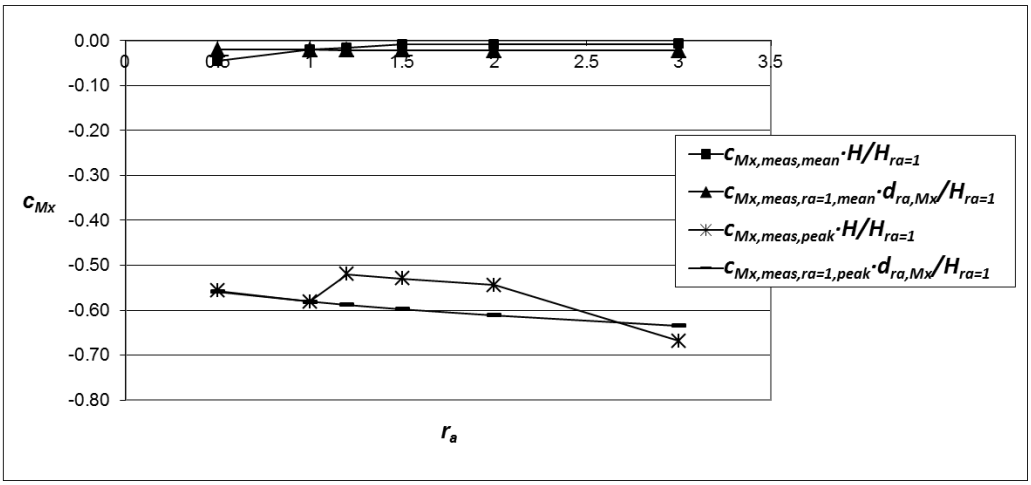

Fig. 31: Aspect ratio dependency of cM_x normalised by the characteristic lever arm H for $r_a = 1$ at load case 5

3.1.3.5 M_{Hy} - hinge moment

The definitions given by Peterka and Derickson (1992, p. 10) are assumed to be valid for all angles of attack and not to apply exclusively to special load cases. Furthermore, they are only valid for squared heliostats (p. 13). They did not intend to give aspect ratio dependencies of the wind load coefficients. However, for the wind moments an effective lever arm is accounted for according to equation (3.1.9). These lever arms are aspect ratio dependent and therefore an aspect ratio dependency is implicitly given by their formulas for the wind moments. For the hinge moment M_{Hy}, the effective lever arm (= characteristic length h) lead to a good agreement with the aspect ratio dependencies of this study (especially for load case 2, see Fig. 32) and are therefore given in the following diagrams.

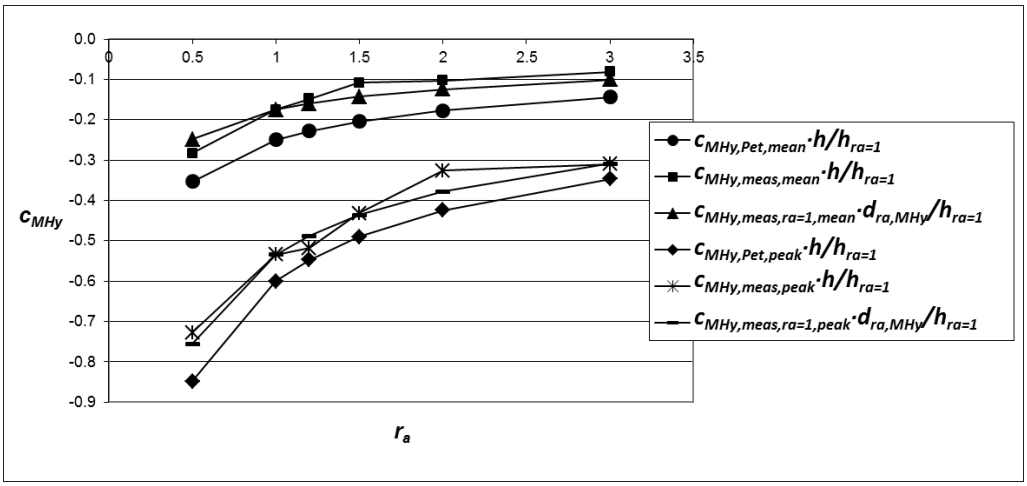

Fig. 32: Aspect ratio dependency of c_{MHy} normalised by the characteristic lever arm h for r_a = 1 at load case 2

The reason for this dependency is the almost linear pressure distribution at load case 2 (Fig. 33, left). For a linear pressure distribution, the lever arm of the resulting force is proportional to h whereas the value of the resulting force itself remains the same because the mirror area is not varied (this will be further discussed in section 3.1.3.8). Thus, all in all M_{Hy} is almost proportional to h.

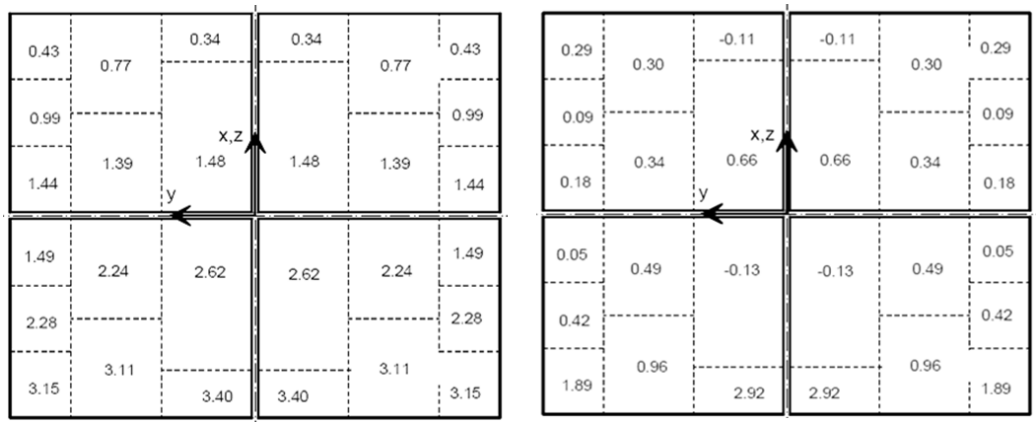

Fig. 33: Pressure coefficient distribution for aspect ratio 1.2 at point in time with peak M_{Hy} with α = 30° and β = 0° (load case 2) (left) and α = 0° and β = 0° (load case 4) (right)

For load case 4 (Fig. 33, right) the pressure distribution which leads to the peak value of M_{Hy} is different to load case 2 (Fig. 33, left). At the frontal edge a small region of high pressure is measured. Presumably, it is caused by a turbulence structure which just hits the mirror panel there. The width of the

frontal edge increases with increasing aspect ratio but the lever arm (distance of the frontal edge to the *y* axis) decreases (see Fig. 39). This explains why the aspect ratio dependency of M_{Hy} at load case 4 is less pronounced compared to Peterka and Derickson (1992, equation (4)) (Fig. 34) and to load case 2 (Fig. 32).

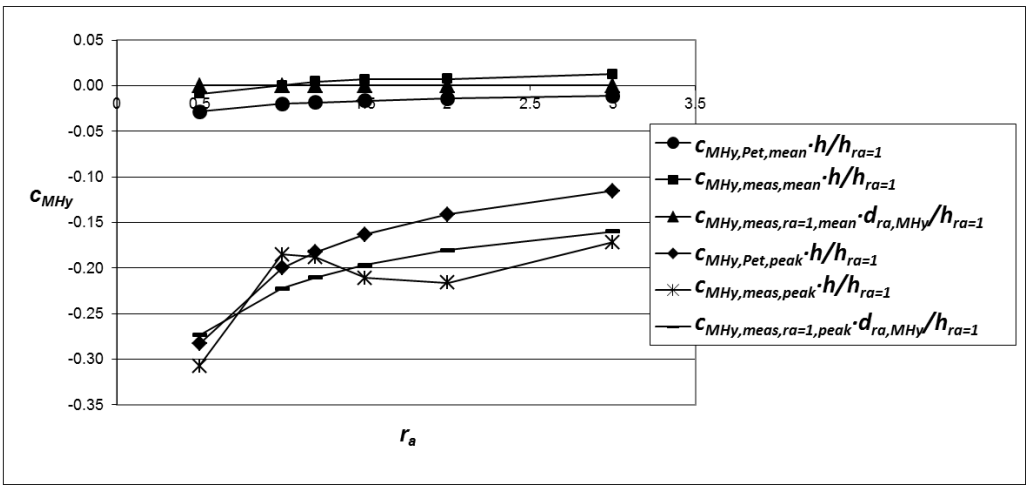

Fig. 34: Aspect ratio dependency of c_{MHy} normalised by the characteristic lever arm h for $r_a = 1$ at load case 4

3.1.3.6 M_y - moment at pylon base about *y* axis

Peterka and Derickson (1992, equation (6)) calculated M_y with

$$M_y = F_x \cdot H + M_{Hy} \qquad (3.1.16)$$

At load case 1, M_{Hy} is relatively small so that equation (3.1.16) can be simplified to

$$M_y \approx F_x \cdot H \qquad (3.1.17)$$

This explains the decrease of the load coefficient of M_y with increasing r_a (Fig. 35) for which H decreases.

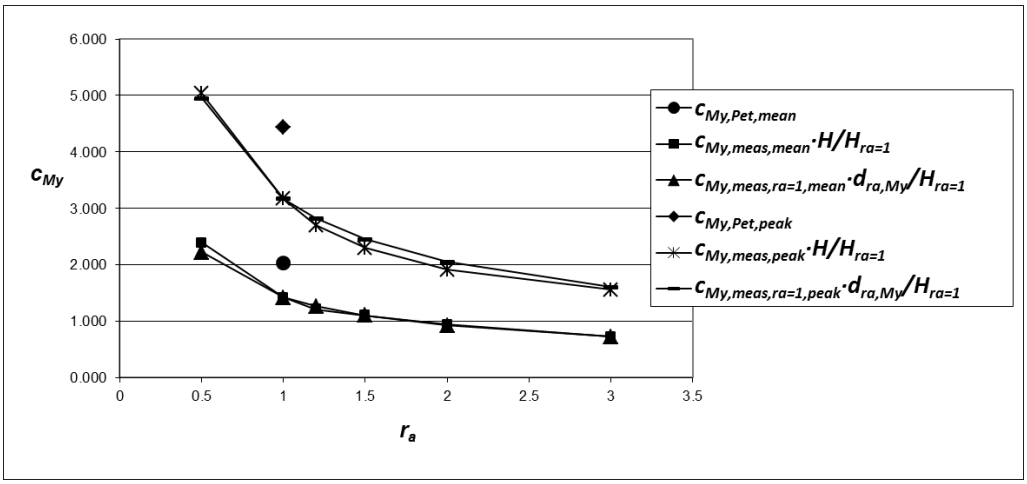

Fig. 35: Aspect ratio dependency of c_{My} normalised by the characteristic lever arm H for r_a = 1 at load case 1

For load case 4, M_{Hy} cannot be neglected. For this case, equation (3.1.16) leads to too high peak values of M_y because the peak values of F_x and M_{Hy} do not occur at the same point in time since they are caused by different flow conditions. This partly explains the higher peak values of M_y of Peterka and Derickson (1992) at load case 4 (Fig. 36).

The values of M_x at load case 5 (Fig. 31) are lower than of M_y at load case 4 (Fig. 36) because of the orientation of the crossbar along with the wind direction which leads to a smaller area of wind attack.

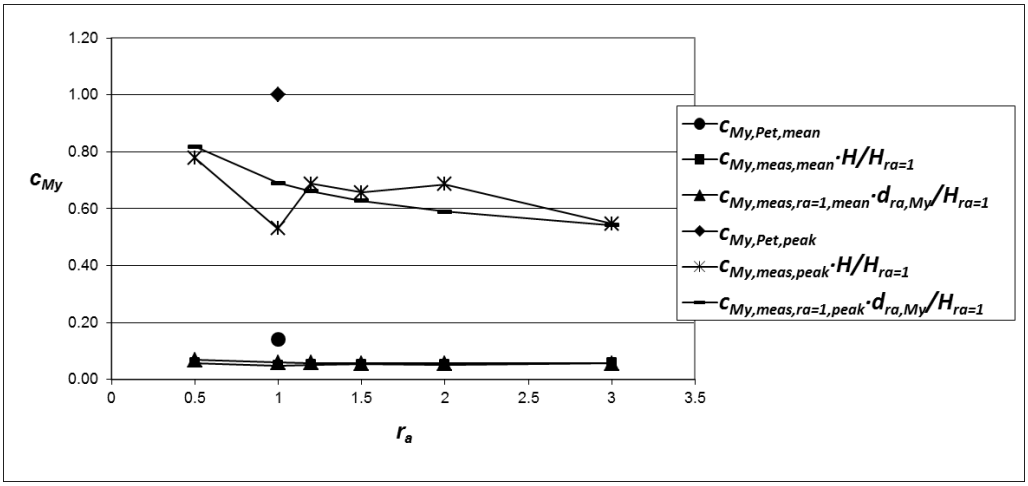

Fig. 36: Aspect ratio dependency of c_{My} normalised by the characteristic lever arm H for r_a =1 at load case 4

3.1.3.7 M_z - moment about azimuth axis

As Peterka and Derickson (1992, equation (5)) assume a squared mirror panel they could take for M_z the same definition as for M_{Hy} for uniformity reasons. However, for varied aspect ratio, a dependency on the width b instead of the height h of the mirror panel would be expected for load case 3 (α = 90°, β = 60°) which is confirmed by the measurements, see Fig. 37. The reason for the almost proportional increase of the absolute values of M_z with increasing b is the alost linear pressure distribution on the whole mirror panel along b comparable to M_{Hy} with h at load case 2 (see section 3.1.3.5).

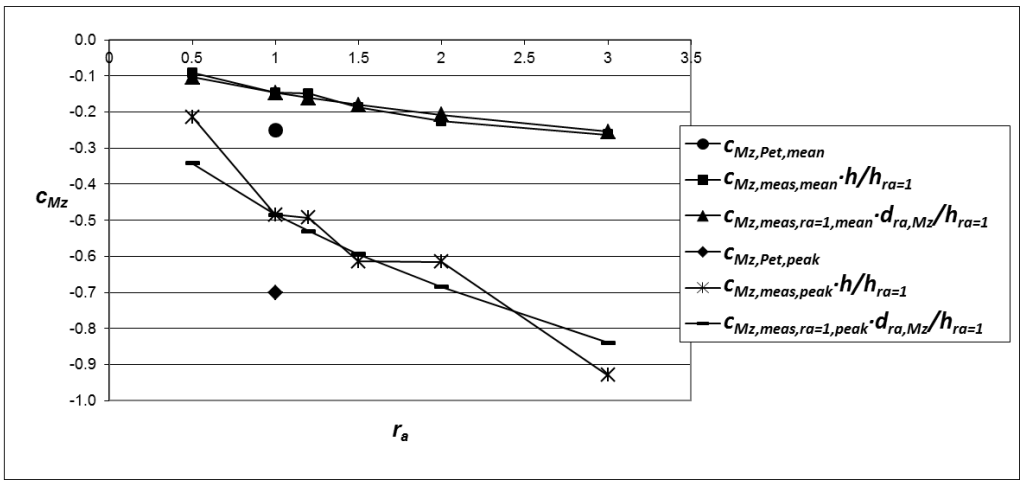

Fig. 37: Aspect ratio dependency of c_{Mz} normalised by the characteristic lever arm h for r_a =1 at load case 3

3.1.3.8 Comparison of aspect ratio dependencies without impact of vertical mean wind speed profile

The values of Peterka and Derickson (1992) for r_a = 1 are for almost all cases considerably higher than measured in this study. If a heliostat model as described in (Peterka et al., 1986, p. 15) was used, part of the reason would be the wide gaps between the three vertical facets. By wind tunnel tests with a heliostat model with two vertical facets and a wide gap in between an increase of the wind loads could be partly measured (section 3.2).

The aspect ratio dependencies defined by equations (3.1.14) and (3.1.15) and given in Table 5 represent exponential fitting curves of the measured data. The fitting was realised by multiplying an appropriate factor and by multiplying the aspect ratio by the power of an appropriate exponent. The aspect ratio dependencies were also used to calculate mean values for varied aspect ratio to prove their general validity. The comparison showed in general good

agreement besides F_x for load case 4 for which the reason is not clear. H, h and b can also be expressed by r_a (the equations for it will be given in the following section). However, for clearness and better comparability with the values of Peterka and Derickson (1992) they are partly given explicitly in Table 5. The exponents and factors are rounded to avoid the impression of an unrealistic high accuracy which is not attainable for peak wind load measurements.

Table 5: Aspect ratio dependencies of peak load measurements with various aspect ratios (without impact of vertical mean wind speed profile) and characteristic lengths of (Peterka and Derickson, 1992)

load case	α	β	wind force	d_{ra} according var. r_a measurements	wind moment	l_i (Peterka and Derickson, 1992)	d_{ra} according var. r_a measurements
1	90°	0°	F_x	$1.0 / r_a^{0.2}$	M_y	H	$H / r_a^{0.2}$
2	30°	0°	F_z	$1.0 / r_a^{0.1}$	M_{Hy}	h	h
3	90°	60°	-		M_z	h	b
4	0°	0°	F_x	$1.3 \cdot r_a^{0.6}$	M_{Hy}	h	$1.2 \cdot h \cdot r_a^{0.2}$
4	0°	0°	F_z	$r_a^{0.4}$	M_y	H	$1.3 \cdot H \cdot r_a^{0.2}$
5	0°	90°	F_y	$1.2 / r_a^{0.1}$	M_x	H	$H \cdot r_a^{0.5}$

For load case 1 the horizontal wind force F_x reduces slightly with the aspect ratio similar to the results of measurements of free standing plates (Sakamoto and Arie, 1983). M_y at load case 1 is the product of the force F_x and the corresponding lever arm H. Therefore, the aspect ratio dependency is equal to the aspect ratio dependency of F_x multiplied by H.

The peak values of M_{Hy} at load case 2 and of M_z at load case 3 are caused by a linear pressure distribution on the panel (Fig. 33, left (M_{Hy})). Such a pressure distribution leads to a linear aspect ratio dependency with the chord length h for load case 2 (and b for load case 3) which is explained by Fig. 38: The resulting force is independent of the aspect ratio because the average pressure and the panel area do not vary with the aspect ratio while the effective lever arm increases linearly with increasing chord length h for load case 2 (or with increasing panel width b for load case 3 respectively).

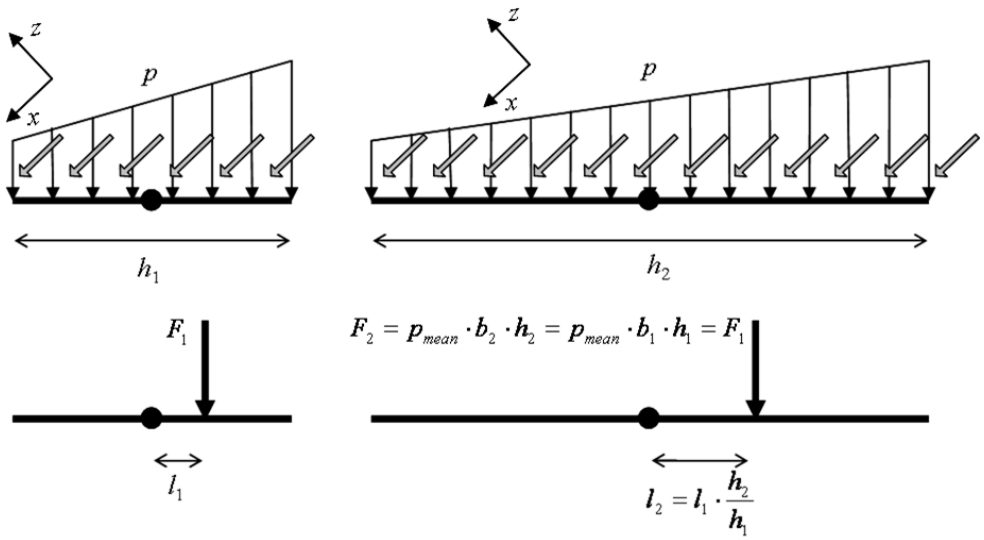

Fig. 38: Resulting force and lever arm at linear pressure distribution for higher (left) and smaller (right) aspect ratio for load case 2

The characteristic lengths l_i of Peterka and Derickson (1992) are almost equal to the effective lever arms for load cases 1 and 2: the elevation axis height H for M_y and the chord length h for M_{Hy}. For M_y, additionally the aspect ratio dependency of F_x is of impact which explains the lower agreement. Corresponding to M_{Hy}, the width b of the panel instead of its height h would have to be used for M_z at load case 3 which was confirmed by the measurements.

For load cases 4 and 5 the panel is in horizontal orientation and thus not directed against the main wind direction. However, at load case 4, the cross bar is exposed directly to the wind and is of higher impact on the wind loads than for the other load cases. Furthermore, the thickness of the panel is of higher impact. For this load case, the area of wind attack of cross bar and frontal panel edge increases with increasing aspect ratio which explains the corresponding increase of F_x. At load case 5, the cross bar is in line with the main wind direction and therefore of no impact. However, the height of the pylon and thus its area of wind attack and the edge of the panel seen by the main wind reduce with increasing aspect ratio which explains the reduction of F_y with increasing aspect ratio. For the peak values of F_z, the length of the frontal edge is decisive because of high pressure in this region which leads to increased values for higher aspect ratios.

High pressure at the frontal edge occurs also at the flow conditions which lead to the peak values of M_x and of M_{Hy} and M_y at load cases 5 and 4 respectively

(see Fig. 30, right (M_x) and Fig. 33 right (M_{Hy})). The impact of it on the aspect ratio dependency is explained by Fig. 39: The resulting force increases with increasing aspect ratio (because of increased panel width *b*) while the lever arm decreases by the same ratio. Therefore, the wind moment would be constant for varied aspect ratio. In fact, the aspect ratio dependencies are less pronounced as for the cases with linear pressure distributions and correction terms which increase with increasing aspect ratio (by the power of 0.2 or 0.5 respectively) are multiplied.

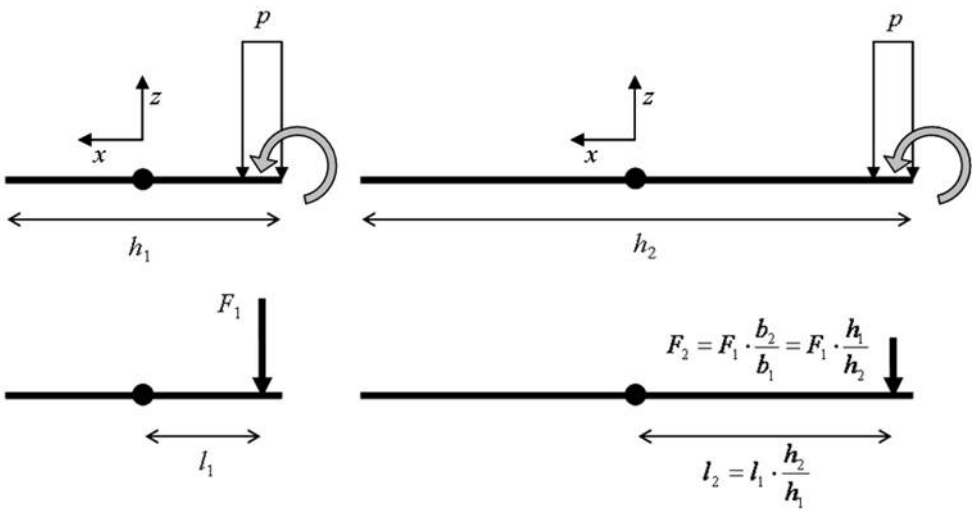

Fig. 39: Resulting force and lever arm for increased pressure at one edge for higher (left) and smaller (right) aspect ratio for load case 4

3.1.3.9 Total impact of aspect ratio on wind load components inclusive vertical mean wind speed profile

Finally, the aspect ratio dependencies are given as functions of r_a only using

$$b = \sqrt{A \cdot r_a} \sim \sqrt{r_a} \tag{3.1.19}$$

$$h = \sqrt{\frac{A}{r_a}} \sim \frac{1}{\sqrt{r_a}} \tag{3.1.19}$$

$$H \cong \frac{1}{2} h \sim \frac{1}{\sqrt{r_a}} \; . \tag{3.1.20}$$

Furthermore, the impact of the solar trackers height is taken into account for all load cases using equation (3.1.1) with n = 0.15 and equation (3.1.6) which leads to

$$p_{dyn} \sim H^{0.3} . \qquad (3.1.21)$$

The resulting total impact of the aspect ratio on the wind load components are given in Table 6.

Table 6: Impact of aspect ratio on wind load components (impact of vertical mean wind speed profile included)

load case	α	β	**wind force**	impact r_a	**wind moment**	impact r_a
1	90°	0°	$\boldsymbol{F_x}$	$\sim 1 / r_a^{0.35}$	$\boldsymbol{M_y}$	$\sim 1 / r_a^{0.85}$
2	30°	0°	$\boldsymbol{F_x}$	$\sim 1 / r_a^{0.25}$	$\boldsymbol{M_{Hy}}$	$\sim 1 / r_a^{0.65}$
2	30°	0°	$\boldsymbol{F_z}$	$\sim 1 / r_a^{0.25}$	**-**	
3	90°	60°	**-**		$\boldsymbol{M_z}$	$\sim r_a^{0.35}$
4	0°	0°	$\boldsymbol{F_x}$	$\sim r_a^{0.45}$	$\boldsymbol{M_{Hy}}$	$\sim 1 / r_a^{0.45}$
4	0°	0°	$\boldsymbol{F_z}$	$\sim r_a^{0.25}$	$\boldsymbol{M_y}$	$\sim 1 / r_a^{0.45}$
5	0°	90°	$\boldsymbol{F_y}$	$\sim 1 / r_a^{0.25}$	$\boldsymbol{M_x}$	$\sim 1 / r_a^{0.15}$

3.1.4 *Conclusions*

The wind load components vary partly significantly with the aspect ratio of the panel. Therefore, the aspect ratio must be considered for the layout of the components of solar trackers. The main components of solar trackers are the foundation, the pylon, the mirror panel, and the elevation and the azimuth drive.

Foundation and pylon must resist the moment at pylon feet M_y. Especially for upright orientation of the panel (load case 1) but also for the stow position with wind direction along the panel height h (load case 4), M_y decreases significantly with increasing aspect ratio. Therefore, the solar tracker in stow position could be turned with the elevation axis orthogonal to the main wind direction to take advantage of this load reduction (if it is possible for the given site to predict the main wind direction at storm conditions). Anyhow, a higher aspect ratio is advantageous regarding the layout of the foundation and of the pylon which could be designed weaker and would be also shorter.

The elevation drive is loaded by the hinge moment M_{Hy}. Usually, the conditions at which the drive is in operation and maximal loaded (load case 2)

are decisive for its layout. Also for the stow position (load case 4) a significant load reduction of M_{Hy} with increasing aspect ratio was determined. Hence, also for the elevation drive a high aspect ratio would be favourable.

For the stow position, the peak value of the moment about the vertical azimuth axis M_z is small even for high storm wind speeds. Thus, for the azimuth drive the upright orientation of the panel with sideward (30° to the panel) wind attack (load case 3) is relevant. For load case 3 an increase of M_z with increasing aspect ratio was determined. This increase is less pronounced compared to the decreases of M_{Hy} with increasing aspect ratio at load cases 2 and 4 (which are decisive for the layout of the elevation drive) but is of more importance for most conventional heliostats for which the azimuth drive is more expensive than the elevation drive.

For a reasonable determination of the aspect ratio, the costs of all components of the solar tracker for different aspect ratios would have to be taken into account.

Please note that different turbulence intensity and unusual flow conditions (for example caused by surrounding buildings or for sites at hilltops), unusual distinctive back structures of the mirror panel or of the torque tube, significantly different relative distance of the mirror panel to the ground at upright position and dynamical effects which are design dependent and not considered in the present study, can lead to different wind loads. Especially in these cases, specific wind tunnel tests are necessary.

Acknowledgments

The investigations were financed by the Bundesministerium für Umwelt, Naturschutz und Reaktorsicherheit (BMU) in the project HydroHelio™ (0325123B). The authors thank also J. F. Vásquez Arango and the reviewers for their helpful suggestions for improvement of this paper.

3.2 Gaps in Mirror Panel

Partly reproduced from [Pfahl, A., Buselmeier, M., Zaschke, M., 2011. "Determination of Wind Loads on Heliostats". Proc. SolarPACES 2011 conference, Granada].[2]

3.2.1 *Introduction*

Most heliostats are designed with closed panels with only small gaps between the facets. Wu et al. (2010) found that these small gaps are of negligible impact on the wind loads. However, it was not investigated yet whether wide gaps are of impact. Peterka and Derickson (1992, p.12) state that up to a portion of 15% of openings the mirror panel can be treated as a solid surface area.

3.2.2 *Method*

The impact of wide gaps on the wind loads was analysed by comparison of the wind load coefficients of a heliostat with no gap and one with two separated mirror facets. The total mirror area (30 m² at full scale, modelling scale 1:20) was the same for both models. The gap was 0.5 m wide at full scale which means that the portion of the opening was 8% (Fig. 40). The wind tunnel set up was the same as described in sections 3.1.2.3.1 and 3.1.2.3.2.

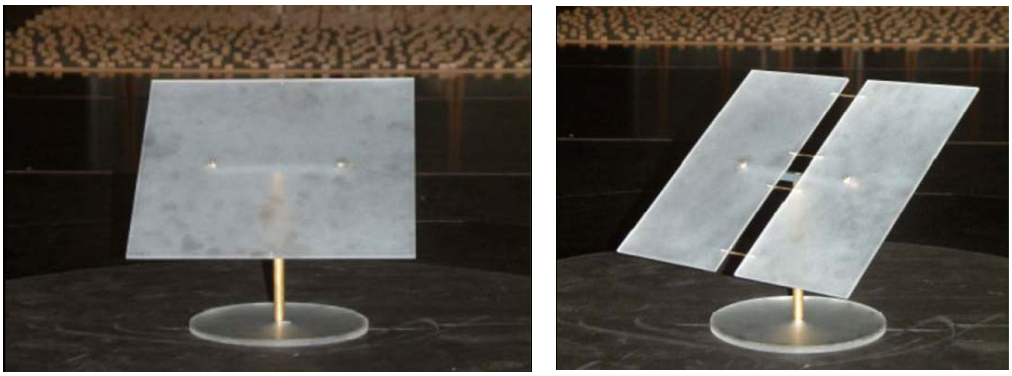

Fig. 40: Heliostat models for investigation of impact of wide gap between mirror facets

3.2.3 *Results and Discussion*

For almost all critical load cases at which one of the loads may have its maximum peak value only small differences between the heliostat models

[2] The BLWT measurements were defined and its results proofed and analysed by the main author. The preparation and execution of the BLWT measurements were performed by the co-authors.

were measured (Table 7) in line with the findings by Peterka and Derickson (1992). However, for the hinge moment M_{Hy} the mean and peak values at load case 2 and the peak value at load case 4 are about 20% higher. The drag force F_x at load case 4 is also increased for the heliostat with wide gap because of the wider torque tube which is of impact especially in the stow position where it is not wind shadowed by the panel. The increased drag force F_x together with the increased hinge moment M_{Hy} lead also to an increased overturning moment at ground level M_y.

Table 7: Impact of wide gap on peak and mean wind load coefficients

load case	α	β	**wind force**	$c_{peak,\ no\ gap}$ ($c_{mean,\ no\ gap}$)	$c_{peak,wide\ gap}$ ($c_{mean,\ wide\ gap}$)	**wind moment**	$c_{peak,\ no\ gap}$ ($c_{mean,\ no\ gap}$)	$c_{peak,wide\ gap}$ ($c_{mean,\ wide\ gap}$)
1	90°	0°	F_x	3.3 (1.5)	3.2 (1.5)	M_y	3.2 (1.4)	3.1 (1.4)
2	30°	0°	F_x	1.6 (0.71)	1.6 (0.65)	M_{Hy}	-0.45 (0.15)	**-0.56 (0.18)**
2	30°	0°	F_z	-2.1 (-0.97)	-2.1 (-0.92)	-	-	-
3	90°	60°	-	-	-	M_z	-0.50 (-0.15)	-0.49 (-0.14)
4	0°	0°	F_x	0.57 (0.06)	**0.78** (0.06)	M_{Hy}	±0.18 (0.00)	**±0.22** (0.00)
4	0°	0°	F_z	±0.50 (0.00)	±0.50 (0.00)	M_y	0.69 (0.05)	**0.82** (0.05)
5	0°	90°	F_y	0.43 (0.05)	0.42 (0.05)	M_x	0.60 (0.03)	0.54 (0.03)

3.2.4 *Conclusions*

Wide gaps in the mirror panel lead to an increase of the pressure distribution at the edges of the gap, especially at the windward corners. This causes an increase of the hinge moment of about 20% for an angle of attack of 30° to the panel and for a main flow direction along the gap. The peak hinge moment at stow position is also increased by this effect because it is caused by an instantaneous sideward angle of wind attack.

Acknowledgments

The BLWT investigations were financed by the Bundesministerium für Umwelt, Naturschutz und Reaktorsicherheit (BMU) in the project HydroHelio™ (0325123B).

4 Wind Loads Within Heliostat Field

4.1 Wind Fence and Heliostat Field Density

Partly reproduced from [Pfahl, A., Buselmeier, M., Zaschke, M., 2011. "Determination of Wind Loads on Heliostats". Proc. SolarPACES 2011 conference, Granada].[3]

4.1.1 *Introduction*

Wind loads on heliostats can be reduced by wind fences. Peterka et al. (1986) state that a reduction of the *mean* loads of 70% can be achieved by wind shading. The reduction of the *peak* loads – which are mainly relevant for the dimensioning of heliostats – is less and is given in (Peterka and Derickson, 1992) for heliostats in operation with orientations that lead to maximal wind load coefficients (called critical load cases 1-3 in our study, see Table 5). The reduction is different for the different wind load components and is between 20-40%. For the safety position (horizontal mirror panel, called "stow position", load case 4 of Table 5) no values were found in literature. However, the peak wind load components usually reach their highest values for the stow position because of the high maximum possible storm wind speeds that overcompensate the low wind load coefficients of the heliostat with horizontal mirror panel in stow. Therefore, in the present study, wind tunnel measurements for the stow position (load case 4) were performed and also for load cases 1-3 (heliostat in operation) for comparison with the values given by Peterka and Derickson (1992).

4.1.2 *Method*

4.1.2.1 Sample Heliostat Field

The wind shading effect depends on the porosity and height of the wind fence and on the distances of the heliostats to the fence and to each other. The distance between the heliostats defines the field density (mirror area/ground area). The field density varies significantly within the field of solar tower plants. To evaluate the benefit of wind fences for solar tower plants the regions of different field densities have to be investigated separately. Furthermore, the field density distribution must be known.

[3] The BLWT measurements were defined and its results proofed and analysed by the main author. The preparation and execution of the measurements were performed by the co-authors.

Therefore, at first a heliostat field with a typical power range had to be defined. Higher power levels lead to higher efficiency and lower specific cost of the power cycle but to lower efficiency of the heliostat field especially due to atmospheric attenuation because of the bigger fields with in average longer distances of the heliostats to the receiver. A reasonable electrical power range is 100 MW at the design point in time as basic cost optimisation calculations have shown and which is confirmed by the power range of commercial solar tower plants. A corresponding heliostat field layout was done with the ray tracing tool HFLCal (Schwarzbözl et al., 2009) with heliostats of 120 m² mirror area and a resulting receiver centre height of 220 m (Fig. 41).

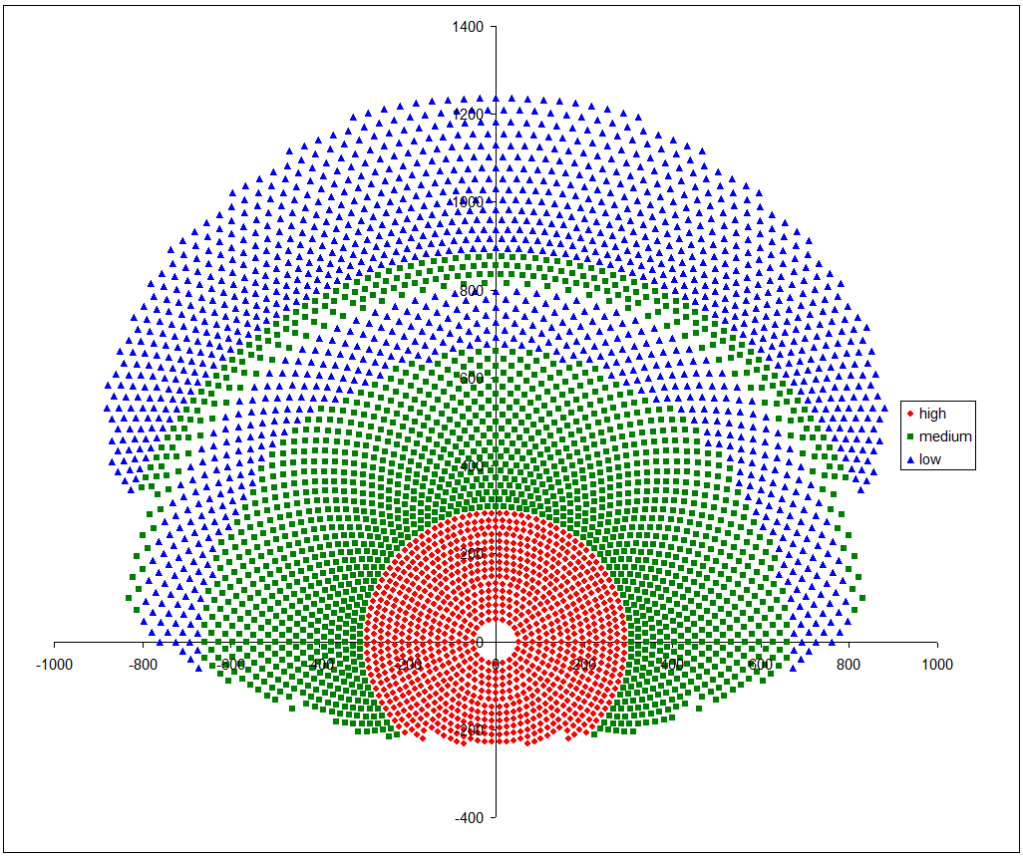

Fig. 41: Regions of high, medium and low field density of heliostat field of a 100MWel solar tower plant

The regions of low (10-20%), medium (20-40%) and high (40-50%) field density for the sample field are shown in Fig. 41 and their portions of all heliostats of the field are given in Table 8.

Table 8: Field density regions

level of field density	value of field density	portion of the field
low	10 - 20%	33%
medium	20 - 40%	43%
high	40 - 50%	24%

4.1.2.2 BLWT Investigations

Peterka and Derickson (1992, p. 44) recommend a fence porosity of 30-50% and a fence height of at least 1.15 to 1.3 times the elevation axis height. Therefore, 40% fence porosity and 1.25 times elevations axis height as fence height was chosen. The porosity of the fence avoids the development of big turbulence structures (Peterka et al., 1986). The main dimensions of the heliostat and the wind fence are given in Fig. 42. Model scale is 1:20. The reflective mirror area is 30m².

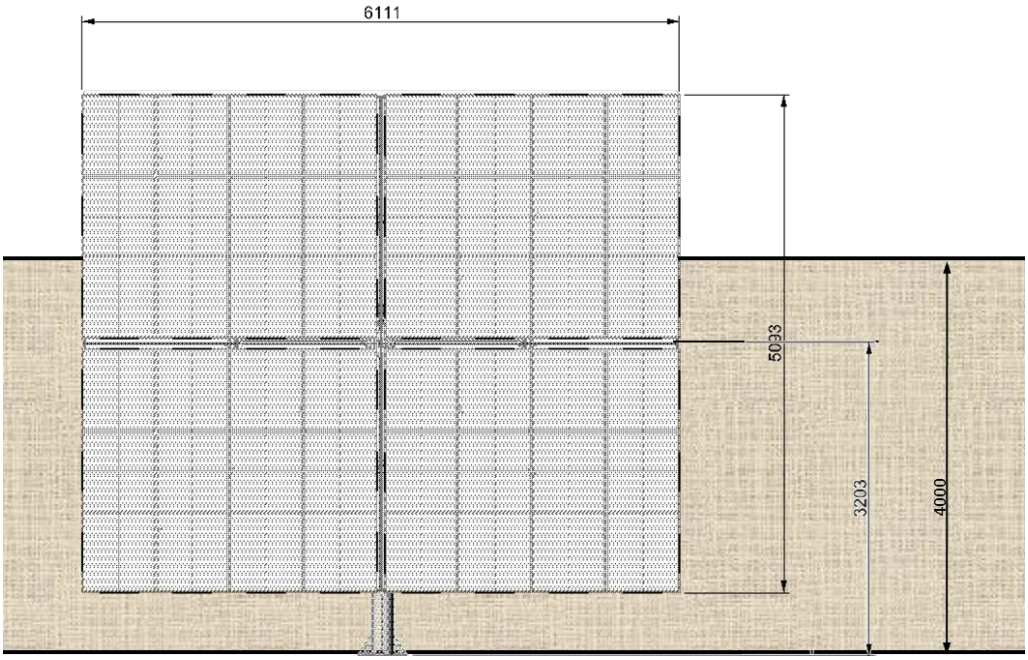

Fig. 42: Dimensions in mm of upright heliostat (α = 90°) and of wind fence (grey, in background) at full scale

Peterka and Derickson (1992) define a Generalised Blockage Area (GBA) for the investigation of the effect of wind shadowing on the wind load coefficients (Fig. 43): GBA = [solid area of upwind blockage projected to wind direction] / [upwind ground area].

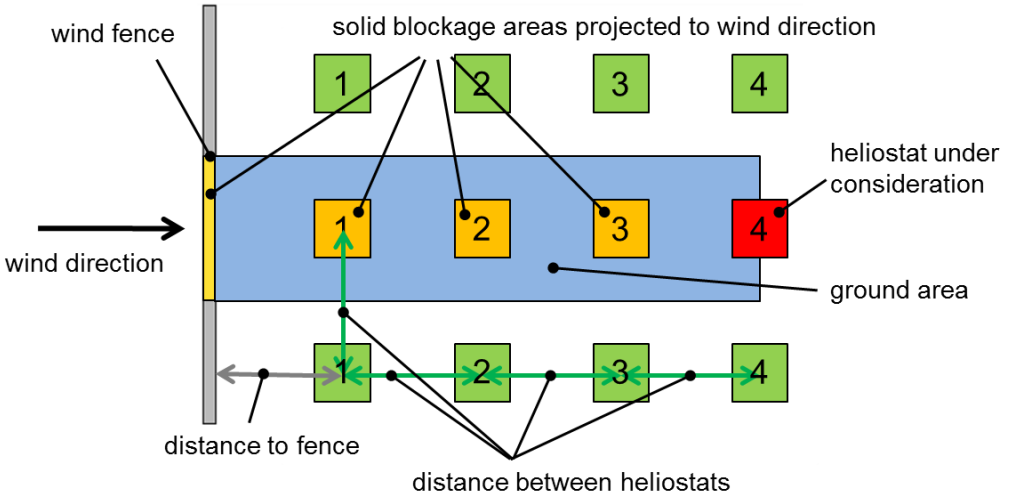

Fig. 43: Definition of areas for the calculation of the Generalised Blockage Area (GBA); red: heliostat for which GBA is calculated, yellow: section of fence that is relevant for the calculation of the solid area of upwind blockage, grey: sections of fence without relevance for the GBA of the red heliostat; blue: upwind ground area; orange: upwind heliostats relevant for the calculation of the GBA of the red heliostat for operation mode (for the stow position their areas projected to the wind direction are negligible small), green: heliostats without relevance for the calculation of the GBA of the red heliostat

For three different distances between the heliostats (8 m, 19 m, and 30m) and for four different distances of the first row heliostat to the fence (5 m, 10 m, 20 m, and 30 m) and for 1-4 rows behind the wind fence (see Fig. 43) the wind load coefficients were determined. The measured combinations and the corresponding field densities and GBAs are listed in Table 9. The amount of investigated rows is lower for larger distances between the heliostats because of size limitations of the wind tunnel.

Table 9: Configurations of wind tunnel measurements for different field densities and different combinations of α (elevation angle) and β (angle between wind direction and elevation axis) for which the maximum values of the wind loads (*Fx, My, Fz, MHy, Mz*) occur (critical load cases)

distance to fence	distance between heliostats	field density	row	GBA operation F_x, M_y: $\alpha = 90°$, $\beta = 0°$	*GBA* operation F_z, M_{Hy}: $\alpha = 30°$, $\beta = 0°$ M_z: $\alpha = 90°$, $\beta = 60°$	GBA stow F_x, F_z, M_y, M_{Hy}: $\alpha = 0°$, $\beta = 0°$
5 m	8 m	47 %	1	0.32	0.32	0.32
			2	0.42	0.27	0.15
			3	0.45	0.26	0.11
			4	0.46	0.26	0.095
10 m	19 m	8 %	1	0.16	0.16	0.16
			2	0.11	0.083	0.061
			3	0.10	0.067	0.040
20 m	30 m	3 %	1	0.080	0.080	0.080
			2	0.053	0.042	0.034
30 m	30 m	3 %	1	0.053	0.053	0.053

Exemplarily, the test set up for the measurement of a heliostat in stow position in row 4 and a distance between the heliostats of 8 m and of 5 m to the fence is shown in Fig. 44. The general wind tunnel configuration was the same as described in sections 3.1.2.3.1 and 3.1.2.3.2.

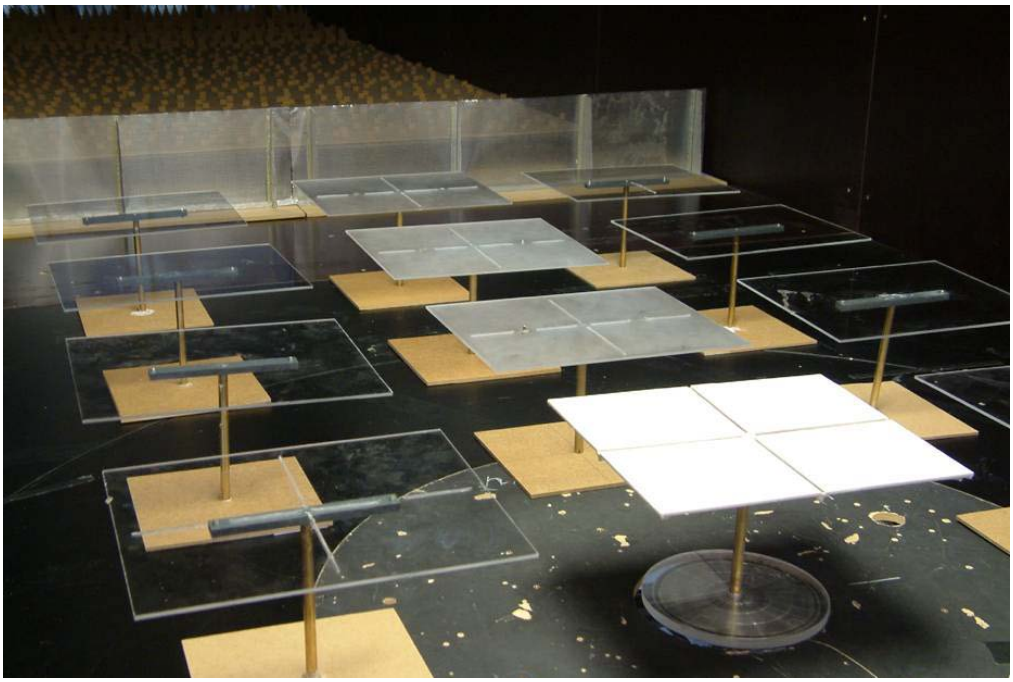

Fig. 44: BLWT investigation of the impact of a wind fence on the wind loads of heliostat fields

4.1.3 *Results and Discussion*

4.1.3.1 Results

Fig. 45 shows how the peak drag coefficient F_x reduces with increasing blockage area for operation mode. The graph is quite irregular because of the high uncertainty in the determination of peak values. For heliostats in operation the orientation that lead to the highest drag is α = 90° and β = 0° (vertical mirror panel, frontal wind attack). The measured reduction for operation mode is higher than stated by Peterka and Derickson (1992). Presumably, the reason is that Peterka and Derickson (1992) measured more configurations with also more disadvantageous ones. The ones with lowest load reduction were used by them to determine the load reduction function.

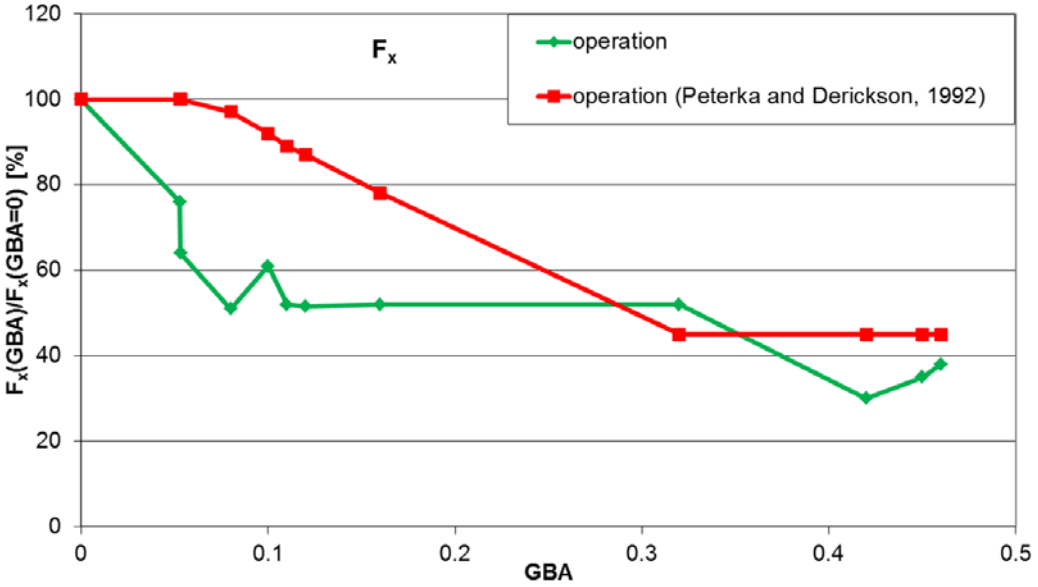

Fig. 45: Reduction of peak drag F_z with increasing Generalised Blockage Area (GBA) for operation mode

For the maximum peak lift coefficient F_z in operation mode (for α = 30° and β = 0°), the measured load reduction is also higher than measured by Peterka and Derickson (1992) (Fig. 46).

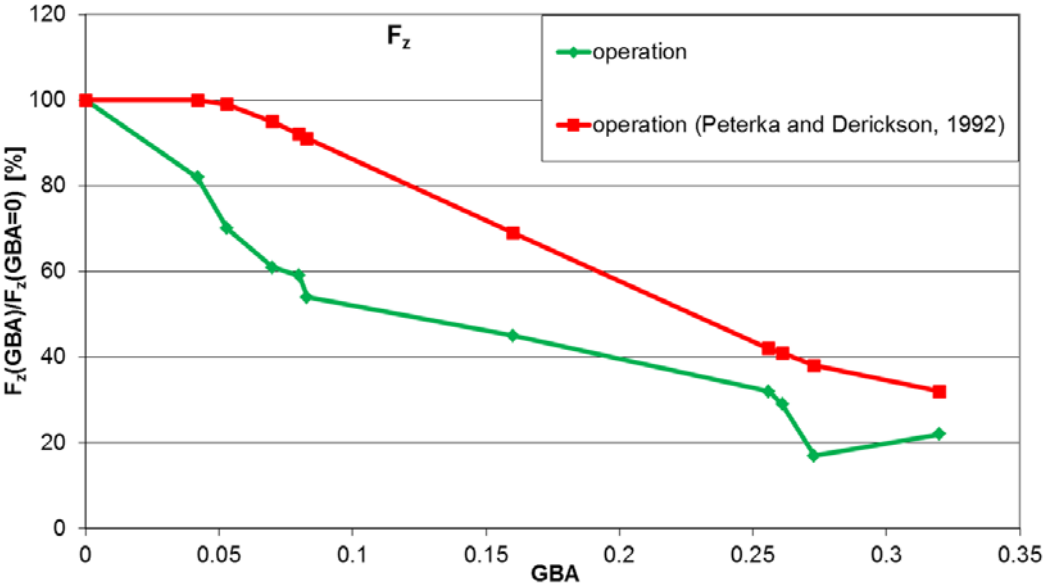

Fig. 46: Reduction of peak lift F_z with increasing GBA for operation mode

Fig. 47 shows the reduction of the overturning moment about the pylon base M_y (for α = 90° and β = 0°). The graph is again quite irregular because of the high uncertainty in the determination of peak values. Peterka and Derickson (1992) give no values for it but only a formula to calculate it by the hinge moment and the drag force (equation (3.1.16)).

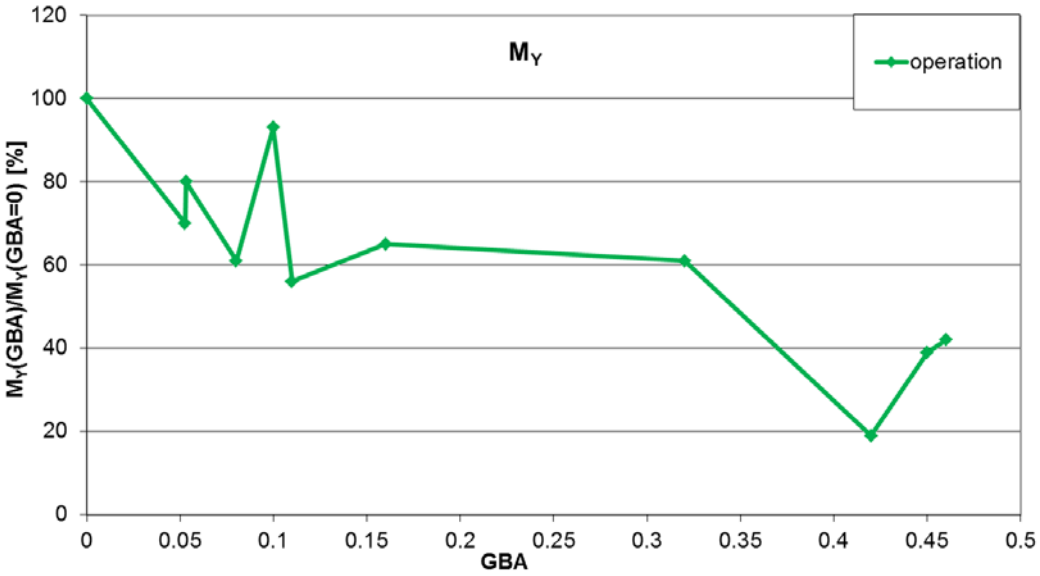

Fig. 47: Reduction of peak base overturning moment M_y with increasing GBA for operation mode

For a GBA < 0.15, the values of the hinge moment coefficient M_{Hy} for operation mode (for α = 30° and β = 0°) are lower than the values of Peterka and Derickson (1992). The irregular graph results again from the general uncertainty of peak load measurements. For a GBA > 0.25, significantly higher values were measured (Fig. 48). Presumably, the reason are turbulence structures caused by the fence which impact especially the hinge moment coefficient of heliostats close to the fence.

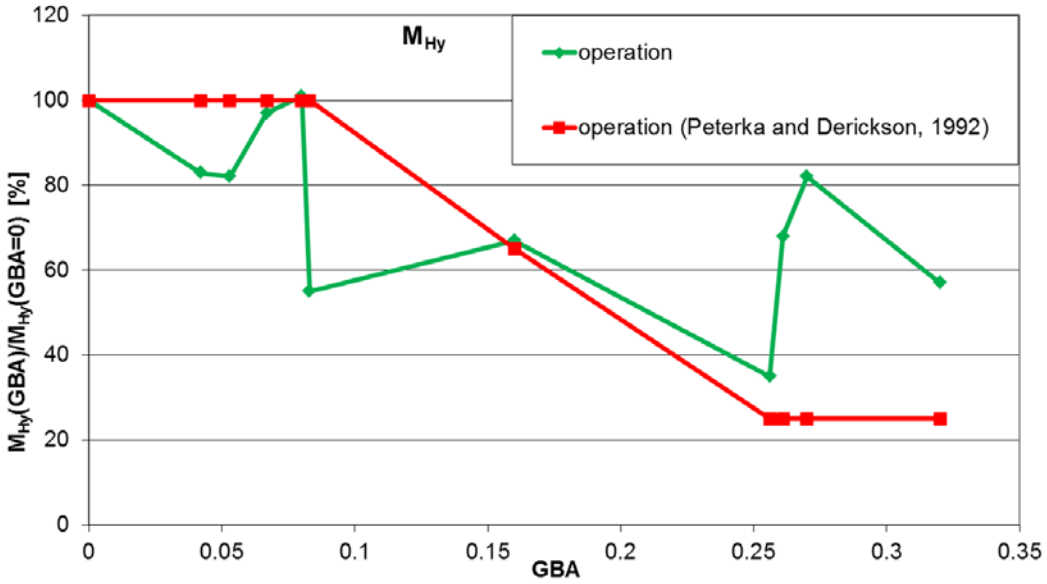

Fig. 48: Reduction of peak hinge moment M_{Hy} with increasing GBA for operation mode

For a GBA > 0.1, the reduction of the maximum peak moment about the vertical axis M_z for heliostats in operation (for α = 90° and β = 60°) is lower than measured by Peterka and Derickson (1992) (Fig. 49).

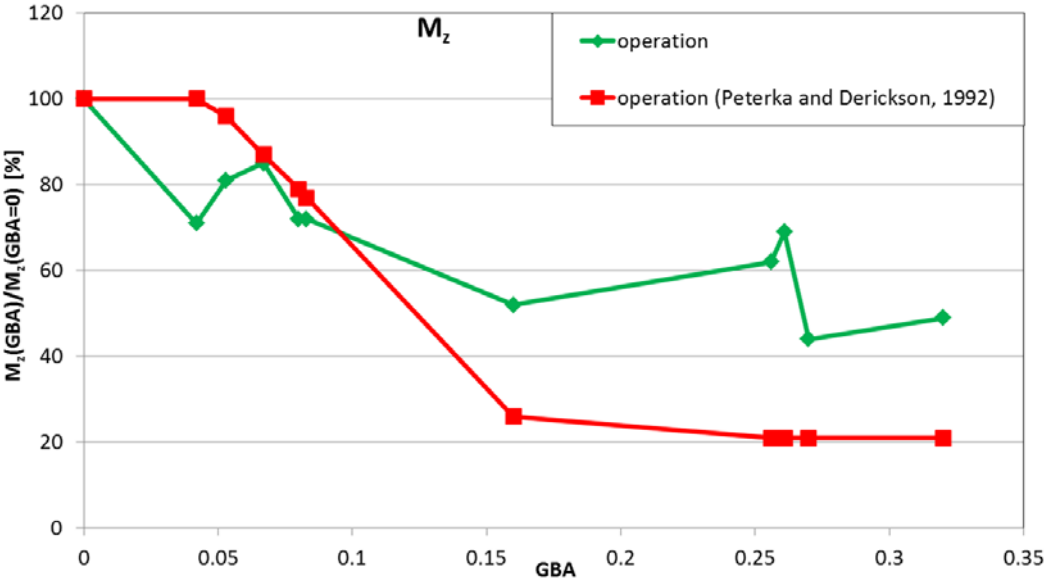

Fig. 49: Reduction of peak moment about vertical M_z axis with increasing GBA for operation mode

For stow position (α = 0° and β = 0°), a significant load reduction for the peak values of F_x, M_{Hy}, and M_y was measured even for low GBA (Fig. 50). However, for the peak lift force F_z even an increased value was measured. Presumably, the reason is the recirculation area behind the wind fence which leads at certain distances and field densities to higher values of the vertical wind velocity component which impacts especially the lift force for horizontal mirror panel.
The moment about the vertical axis M_z is negligible low for stow and was not investigated.

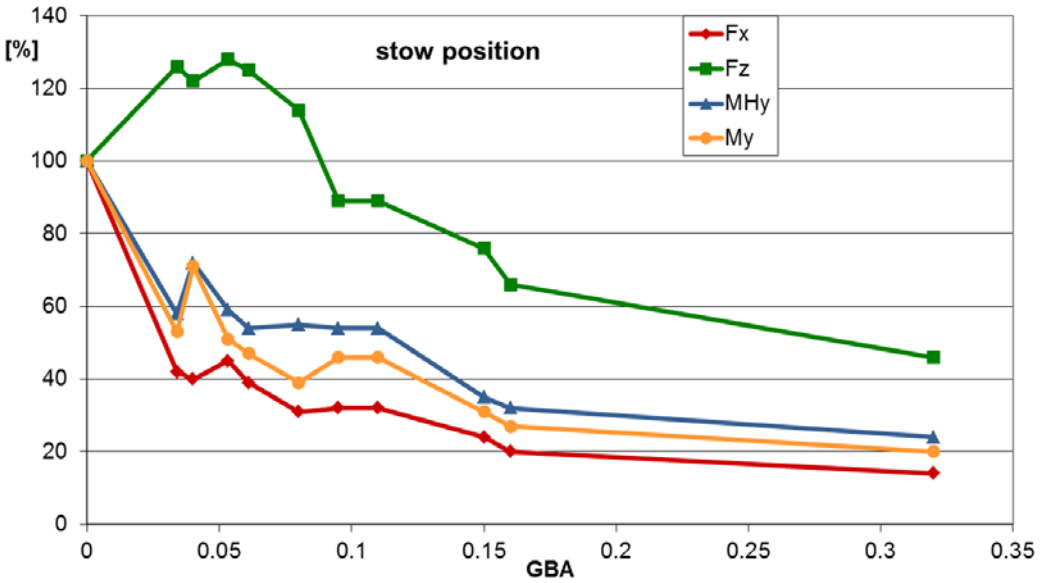

Fig. 50: Reduction of peak coefficients of F_x, F_z, M_{Hy}, and M_y with increasing GBA for the stow position

4.1.3.2 Discussion

Table 10 gives an overview of the load reductions (relative to an isolated heliostat) for the different wind load components for high and for low field density for the critical load cases. The negative value indicates that not a load reduction but an increase of the load within the field was measured. The values are valid for the sample case given in section 4.1.2 with lowest field density of 10%. This corresponds to a GBA of approximately 0.1 for F_x and M_y, 0.07 for F_z, M_{Hy} and M_z for operation mode and 0.04 for stow (Table 9). Highest field density is 47% which corresponds to a minimum GBA of 0.32 for F_x and M_y, 0.26 for F_z, M_{Hy} and M_z for operation mode and 0.1 for stow (Table 9). The corresponding load reductions were determined with Fig. 45 - Fig. 49.

In each case, the lower value of the measurements and of Peterka and Derickson (1992) was taken into account.

Table 10: Load reduction for heliostats in operation and in stow position for high and low field density

mode:	operation		stow		relevant for component
wind load component \ field density:	low	high	low	high	
F_x	10%	50%	60%	70%	pylon
F_z	0%	60%	-30%	10%	panel
M_{Hy}	0%	20%	30%	50%	elevation drive
M_y	10%	40%	30%	50%	pylon
M_z	10%	30%	-	-	azimuth drive

It must be noted that in this study only a few constellations could be measured. There might be other constellations which would lead to higher values, especially with rows further away from the fence. To achieve the highest values of a specific heliostat field it is necessary to perform wind tunnel investigations with models of the special heliostat and of specific characteristic field regions (for example corners formed by the fence or aisles within the field) and for various wind directions.

4.1.4 *Conclusions*

By wind fences a load reduction of 10% of the horizontal force F_x and the moment about the pylon base M_y in operation mode (relevant for the dimensioning of the pylon) at regions of low field density is achievable for the investigated field configurations. For the hinge moment M_{Hy} and the moment about the azimuth axis M_z in operation mode (relevant for the drive's dimensioning) the load reduction is as well only small (0% and 10% respectively) for low field densities. Regarding the dimensioning of the mirror panel, a wind fence can be even disadvantageous because of the increased vertical force F_z at stow position. Therefore, if a uniform heliostat design for the complete field is foreseen (which have to take the only low load reduction of field regions with low field densities into account, see orange coloured fields of Table 10) it is doubtful whether a wind fence is worthwhile. If the heliostats could be dimensioned differently, the whole structure and the drives could be designed significantly weaker for regions of high field density (see relevant green coloured fields of Table 10).

Acknowledgments

The BLWT investigations were financed by the Bundesministerium für Umwelt, Naturschutz und Reaktorsicherheit (BMU) in the project HydroHelio™ (0325123B).

4.2 Heliostat Field Corners

4.2.1 *Introduction*

In (Peterka et al., 1992) it is stated that within a heliostat field higher wind loads occur at than for an isolated heliostat. The field positions where the higher wind loads occur are not given. The factors (f_{field} = max. wind load in field / wind load single heliostat) for the mean and for the peak wind forces as determined by these authors are given in Table 11. For the wind moments no such increase is stated.

Table 11: Factors of increase of mean and peak wind loads within field according to (Peterka et al., 1992)

Elevation α	Wind Direction β	Wind Force	$f_{field,\ mean}$	$f_{field,\ peak}$
90°	0°	Drag (F_x)	1.5	1.4
30°	0°	Lift (F_z)	1.4	1.3

The reason for the increased values within the field is not given by (Peterka et al., 1992). In the following, it is investigated whether the increase of the drag force F_x is caused by an increased wind speed at the corner of the field.

4.2.2 *Method*

The flow around the corner of a heliostat field was simulated in a BLWT. The mirror panel of the investigated heliostat is 4m x 4m and the model scale is 1:30. The boundary layer is generated as described in sections 3.1.2.3.1 and 3.1.2.3.2. The model for the measurements of an isolated heliostat is shown in Fig. 51.

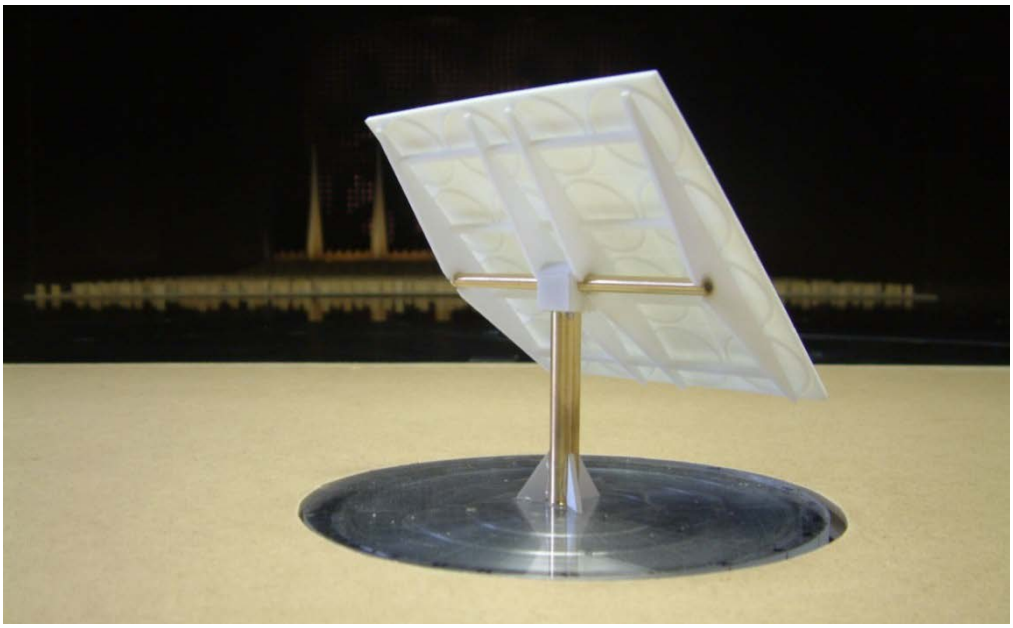

Fig. 51: Model for measurements of an isolated heliostat

16 heliostats were positioned according to Fig. 52. The sideward distance of the heliostats is 9 m and the row distance 6 m at full scale.

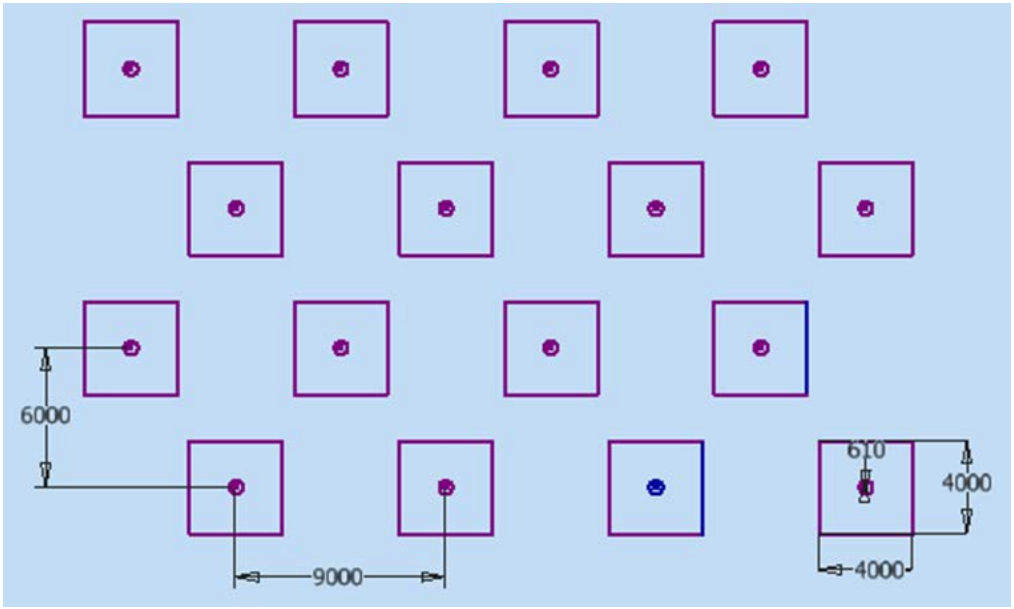

Fig. 52: Dimensions of heliostat field configuration for BLWT measurement.

Fig. 53 shows the BLWT test set up of the investigated field configuration.

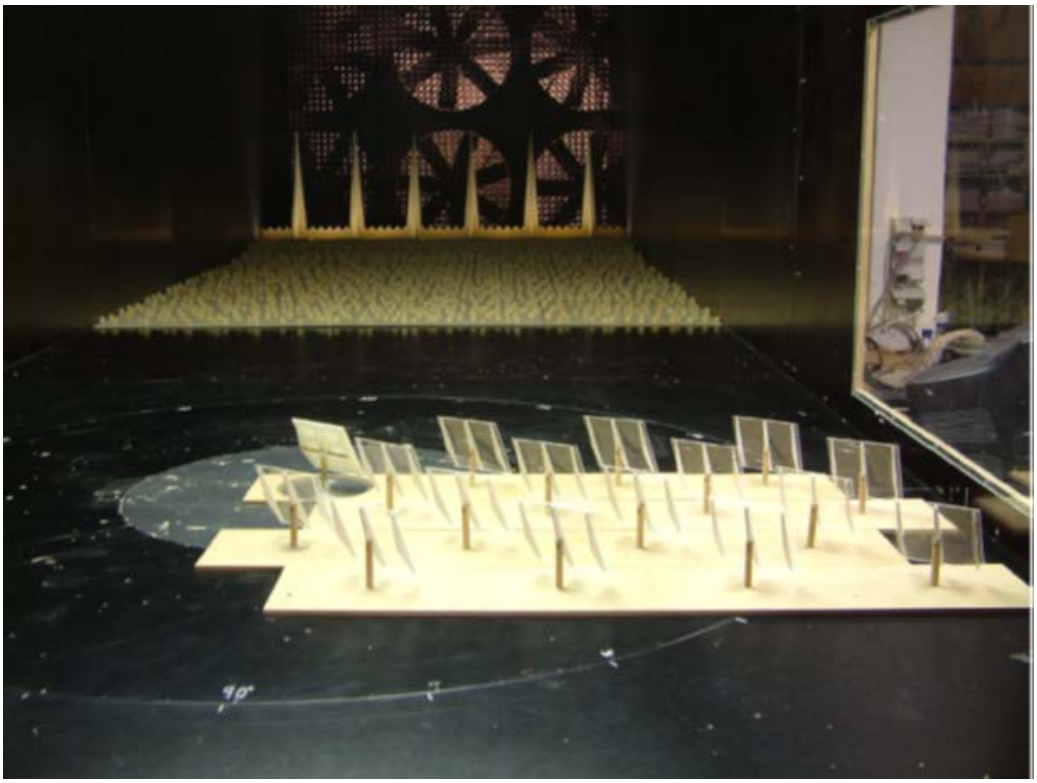

Fig. 53: Edge field configuration of wind tunnel measurements

4.2.3 *Results and Discussion*

As expected, the drag coefficient is increased at the corner heliostat of the investigated field configuration (Table 12). However, the resulting field factor is less then stated by Peterka et al. (1992). There might be other more disadvantageous configurations which lead to even more increased loads. Especially, a higher field density could lead to a higher field factor.

Table 12: Factors of increase of mean and peak wind loads at heliostat field corner compared to single heliostat

mean/peak	Configuration	c_{Fx}	f_{field}	f_{field} *(Peterka et al. 1992)*
mean	single	1.36	1.11	1.5
	field corner	1.51		
peak	single	3.17	1.11	1.4
	field corner	3.52		

4.2.4 *Conclusions*

An increase of the drag force at the corner heliostat of a heliostat field was measured by boundary layer wind tunnel tests. The effect is much less than the increase within a field stated by Peterka et al. (1992) who may have investigated more disadvantageous configurations. This should be followed up by future wind tunnel investigations.

Acknowledgments

The investigations were financed by the Bundesministerium für Umwelt, Naturschutz und Reaktorsicherheit (BMU) in the project HELIKO (16UM0081).

5 Impact of Wind Properties on Heliostat Wind Loads

5.1 Reynolds Number

This section is reproduced from [Pfahl, A., Uhlemann, H., 2011. "Wind Loads on Heliostats and Photovoltaic Trackers at Various Reynolds Numbers". Journal of Wind Engineering and Industrial Aerodynamics 99, 964-968].[4]

Abstract

Wind loads on heliostats are usually determined by boundary layer, low-speed wind tunnels at which the design full-scale Reynolds number cannot be reached. In doing so, it is supposed the wind load coefficients are Reynolds number independent, which is known to be the case for sharp edged bodies. However, for the stow position the usually round torque tube is directly exposed to the wind and could influence the wind loads.

By measurements in a high-pressure wind tunnel, it can be demonstrated that the design-relevant wind load coefficients are not Reynolds number dependent. However, the inclination of the mirror panel in stow position, due to the deflection of the heliostats structure at high Reynolds number, leads to increased wind loads and must be considered. The results are also valid for photovoltaic trackers of similar shape.

Keywords

heliostat, PV tracker, wind load, Reynolds number, high pressure wind tunnel, central receiver, solar tower, concentrated solar power, solar thermal

5.1.1 *Introduction*

Solar thermal power plants are a promising option to cover significant parts of increasing energy demand. At solar tower plants (Fig. 54), sun-light is concentrated by mirrors that track the sun in two axes, the so-called heliostats. To reduce the blocking of each other, the heliostats reflect the sun rays to the top of a tower. There a receiver absorbs the radiation and supplies thermal energy to a power cycle; alternatively, the energy is used by chemical thermal processes or concentrated photovoltaic generation.

[4] The BLWT measurements and the FEM-calculations were defined and its results proofed and analysed by the main author. The preparation and execution of the measurements were performed by the co-author.

Fig. 54: Solar tower plant (Brightsource Energy, 2011)

The heliostat field is the main cost factor of solar tower plants. For a cost efficient dimensioning of the heliostats, the wind loads must be known. Wind tunnel measurements that have been published so far have all be performed at Reynolds numbers (*Re*) considerably below the maximum values that can occur in realty.

While the drag force coefficient of sharp-edged bodies does not depend on *Re* because the separation is determined by the edges, for structures with round edges it may significantly vary beyond a certain critical *Re* depending on the surface roughness (*k*/*d* = grain size of sand / diameter of cylinder), see Fig. 55.

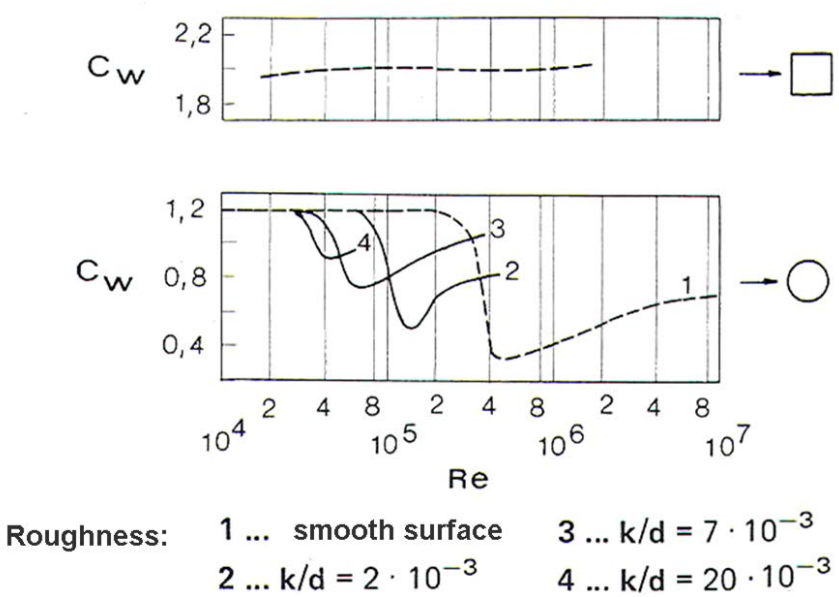

Fig. 55: Drag force coefficient for square and circular profile at different surface roughnesses (Scruton, 1981)

The usually horizontally aligned, circular torque tube of heliostats might be a source of such Re-dependent wind load coefficients. In regular operation, this torque tube is not directly exposed to the wind (Fig. 56) and therefore is of minor importance for the wind loads.

Fig. 56: Heliostats with mirror panels of 120m²

For storm protection, the heliostats are horizontally aligned to minimise the surface of wind attack. In this stow position the torque tube is exposed directly to the wind. Hence, the separation at the torque tube and the following recirculation could depend on *Re*. The recirculation area influences the pressure distribution on the back side of the mirror panel (Fig. 57) and thus the hinge moment M_{Hy} about the torque tube centre line (elevation axis). M_{Hy} at this position can be maximised and therefore this configuration is relevant for the heliostat design. The main objective of the investigations is to determine whether a significant dependency of the wind load coefficient of M_{Hy} on *Re* exists.

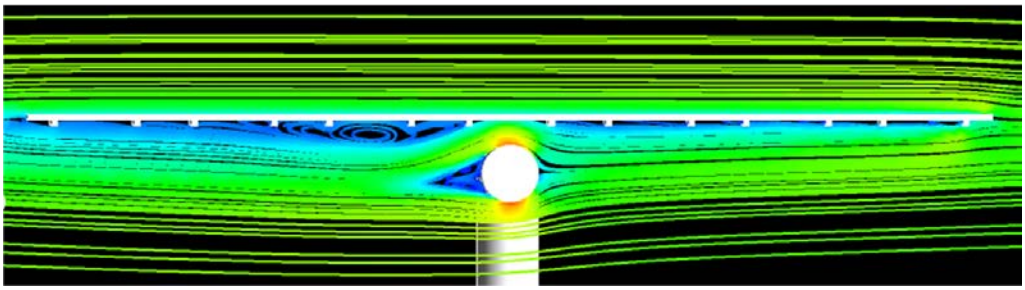

Fig. 57: Stream lines around heliostat in stow position (CFD simulation, only for illustration)

5.1.2 *Method*

5.1.2.1 Specifications and definitions

The *Re*-numbers are highest for big heliostats. Therefore, a typical, big heliostat with 120m² mirror area (Fig. 56) was investigated. The main specifications are:

h	9.6 m	height of mirror panel
b	12.9m	width of mirror panel
H	5.4 m	height of elevation axis
d	0.6 m	diameter of torque tube
V_{max}	40m/s	design wind speed at height H
$Re_{d,max}$	$1.7 \cdot 10^6$	full-scale *Re* based on d at height H

The investigated wind loads are:

F_x	[N]	horizontal wind force perpendicular to el. axis
F_z	[N]	vertical wind force
M_y	[Nm]	wind moment at foundation
M_{Hy}	[Nm]	wind moment about elevation axis

The definitions of the wind load coefficients are according to Peterka and Derickson (1992, p. 10 et seqq.):

$$F_x = c_{Fx} \cdot \frac{\rho}{2} \cdot V^2 \cdot A \tag{5.1.1}$$

$$F_z = c_{Fz} \cdot \frac{\rho}{2} \cdot V^2 \cdot A \tag{5.1.2}$$

$$M_y = c_{My} \cdot \frac{\rho}{2} \cdot V^2 \cdot A \cdot H \tag{5.1.3}$$

$$M_{Hy} = c_{MHy} \cdot \frac{\rho}{2} \cdot V^2 \cdot A \cdot h \tag{5.1.4}$$

with

c	[-]	wind load coefficient
ρ	[kg/m³]	density of air
V	[m/s]	mean wind speed at elevation axis height H
A	[m²]	mirror area

5.1.2.2 Selection of tool

For the determination of the *Re* dependency, computational fluid dynamics (CFD) is almost not feasible because for the prediction of the position of the separation point of round-shaped bodies a very high resolution grid would be required for which a supercomputer would be needed.

The determination of the *Re* dependency in the atmosphere at full scale is hardly possible because the appearance of the needed high wind speeds is seldom and not predictable. Investigations in a wind tunnel at real scale would demand a huge wind tunnel, which was not available. Measurements in conventional wind tunnels would be relatively cheap, but the needed *Re* cannot be reached because *Re* reduces with the model scale (*Re* is linear to the length scale):

$$\mathrm{Re} = \frac{\rho \cdot V \cdot l}{\eta} \tag{5.1.5}$$

with

l [m] characteristic length

η [kg·m/s] dynamic viscosity

Even if the required wind speed could be reached, the results of the measurements would not be reliable because the Mach number would be higher than 1 at regions of high wind speed (especially at the thickest cross section of the cylinder). Therefore, the flow could not be regarded as incompressible which is a requirement for the assumption of similarity (Hucho, 2002, p. 439 et seqq.). By roughening of the round shapes the critical *Re* can be reduced (see Fig. 55). However, it is still too high to be reached by conventional boundary layer wind tunnels. Furthermore, the flow of the recirculation area would be influenced which would distort the results.

Re can also be increased using a fluid of lower kinematic viscosity ($\nu=\eta/\rho$) like water (15 times lower than air) as realised in water tunnels. However, at high fluid speed, cavitation occurs. Therefore, the achievable *Re* is too low for the given task (Hucho, 2002, p. 470).

In kryo channels, the kinematic viscosity is reduced as well – through cooling of the fluid. However, the Mach number is also increased and therefore (because of the Mach number limitation) the specified *Re* number could not be reached at the available Kryo Channel of Cologne (Vieweger, 1989).

Instead of cooling the fluid it also can be pressurised to increase its density. At the High Pressure Wind Tunnel of Göttingen (HDG), up to 100 bars (= 10 MPa) and a wind speed of 35m/s can be reached (Förscher et al., 1981), which leads to sufficient high *Re*. The impact of the *Re* number on the wind load coefficient of isolated circular cylinders (Fig. 55) was investigated in the same wind tunnel by Schewe (1983). A scheme of the HDG and its main characteristics are shown in Fig. 58.

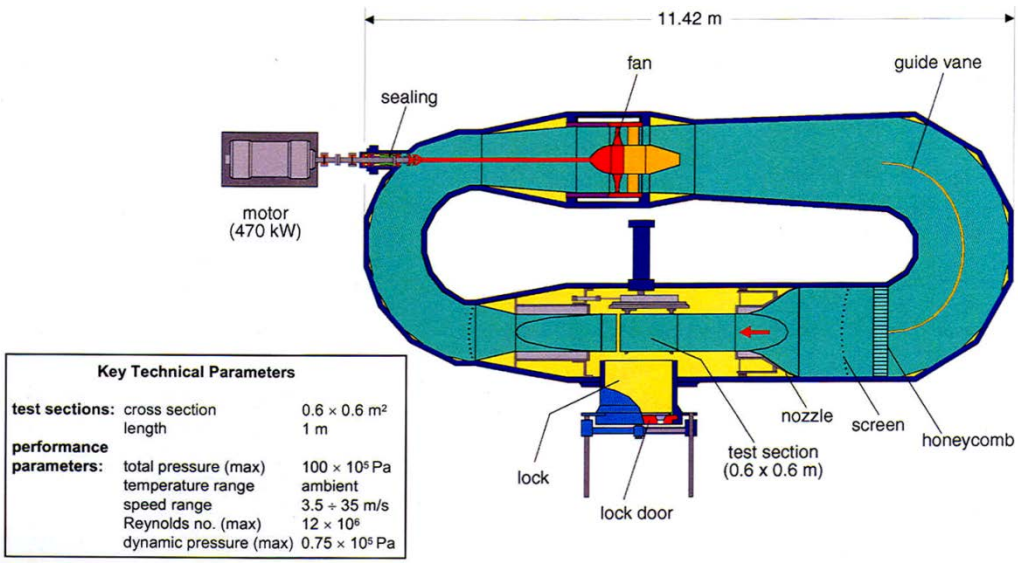

Fig. 58: High Pressure Wind Tunnel of Göttingen (HDG)

At the HDG it was not possible to simulate the turbulence of the atmospheric boundary layer. The vertical fluctuating component of the turbulent wind induces additional lift forces on the torque tube of circular cross-section (Basu and Vickery, 1983) and on the heliostat in all (Peterka and Derickson, 1992; Pfahl et al., 2011a). Furthermore, by Cheung and Melbourne (2005) an increase of the span-wise force correlation with increasing turbulence intensity was determined. However, regarding *Re* dependency, it is expected that by measurements with low turbulence intensity, all effects that would appear at high turbulence intensity are captured because for circular cylinders the critical *Re* reduces for higher turbulence intensity to lower values (Fage and Warsap, 1929).

5.1.2.3 Model and test set-up

A model scale of 1:50 was chosen to ensure the boundary layer of the side walls would not affect the measurements and the blockage was not too high (Isyumov, 1999, p.14). The support structure of the mirrors was roughly

modelled using the advanced sinter metal rapid prototyping technique (Fig. 59). In general, the small gaps between the mirror facets are not of significant influence on the wind loads (Wu et al., 2010). Nevertheless, they were modelled because it could not be excluded that they have an impact on the *Re* dependency.

Fig. 59: Heliostat model in HDG, scale 1:50

The heliostat model was arranged above a splitter plate, simulating the ground, and connected to a strain gauge balance outside the test section. The whole set-up is integrated into the side wall. Here, the heliostat model is mounted by its pylon to the external balance (Fig. 60). Although possible in the HDG, no wind-over-ground profile was simulated because for the stow position, it should be of negligible influence. A 90° angle of wind attack to the torque tube at horizontal mirror panel was investigated because at this configuration the influence of the torque tube should be highest.

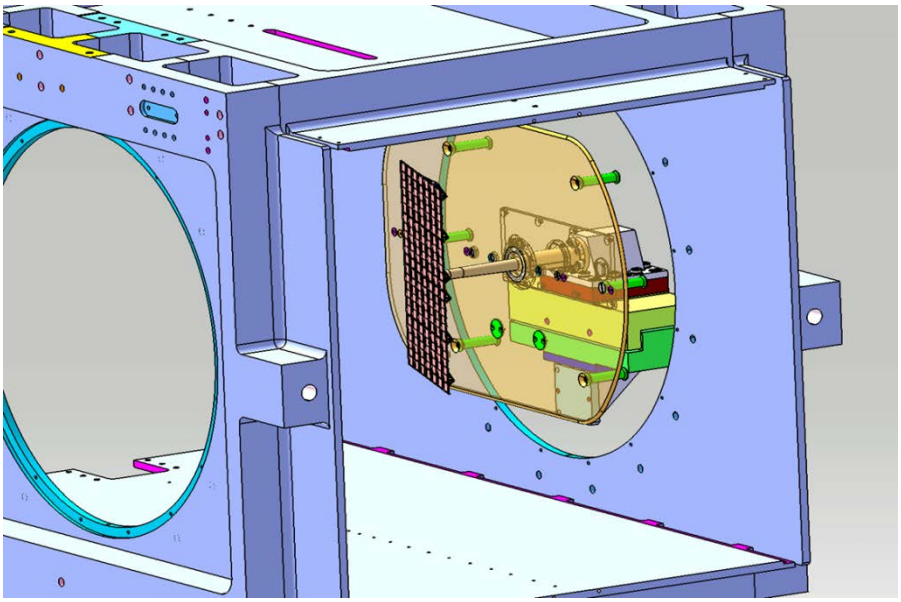

Fig. 60: Schematic view of the HDG-Set-Up with heliostat model, splitter plate, external balance and turn table

5.1.2.4 Correcting model deflection due to wind loads

The model is more stressed by the wind loads than the original heliostat because:

$$\sigma = M / S \quad (5.1.6)$$

$$M \sim p \cdot l^3 \quad (5.1.7)$$

$$p \sim \rho \cdot V^2 \quad (5.1.8)$$

$$S \sim l^3 \quad (5.1.9)$$

so

$$\sigma \sim \rho \cdot V^2 \quad (5.1.10)$$

with

σ	[N/m²]	maximal bending stress
M	[Nm]	bending moment
S	[m³]	section modulus
l	[m]	characteristic length
p	[N/m²]	dynamic pressure

Assuming a pressure of 70 bar (= 7 MPa) in the wind tunnel and a wind speed of 35 m/s to reach $Re_d = 1.7 \cdot 10^6$, the stress of the model material would be

about 50 times higher than the one of the full scale heliostat at the same *Re* (wind speed of 40 m/s). This was partly compensated using solid profiles, slightly thicker cross sections and a material with high modulus of elasticity for the model. Nevertheless, at high *Re,* deflection of the model could not be avoided which is critical because it influences the results significantly.

To eliminate the influence of the deflection, the inclination caused by the measured loads at high *Re* was calculated via FEM (finite element method). The model was validated by calculating and measuring the deflection at a nominal panel inclination angle of the mirror panel of 10° and at $Re_d = 1.7 \cdot 10^6$. Taking the backlash of the bearing also into account, a good agreement between measurements and simulation could be assessed (Fig. 61).

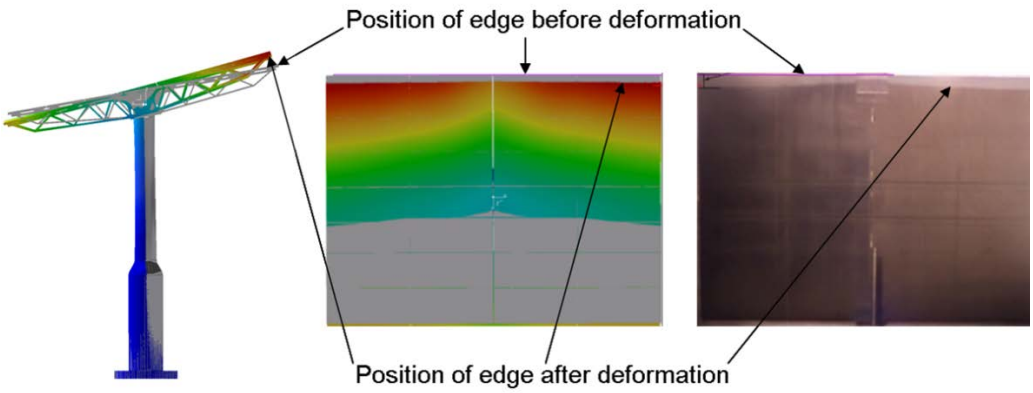

Fig. 61: Calculated (left and middle) and measured (right) deflection of wind tunnel model at *Re* = 1.7·10^6

With the FEM model, the influence of the deflection could be eliminated by the following steps:

- Wind tunnel measurement of the moment about the pylon base for a nominal panel inclination of 0° at $Re_d = 1.7 \cdot 10^6$
- Calculation of the pressure distribution according to the typical pressure distribution of an even plate at small angles of wind attack and adapted according to the measured moment about the pylon base
- Calculation of the deflection caused by this pressure distribution via FEM model and determination of the resulting inclination of the mirror panel
- Measurement of the wind loads at the calculated inclination at low *Re* and determination of the wind load coefficient

- Comparison of the wind load coefficients for Re_d = $1.7 \cdot 10^6$ and a nominal panel inclination of 0° and for the calculated inclination and low *Re*: If a *Re* dependency exists the values should be different.

5.1.3 *Results and Discussion*

5.1.3.1 Results

All six components of the aerodynamic loads were systematically measured at Re_d= $0.2 \cdot 10^6$ - $1.7 \cdot 10^6$, for nominal inclination (for unloaded mirror panel) and yaw angles of 0º (storm idle position). The diagram (Fig. 62, solid lines) shows the coefficients of drag (c_{Fx}), lift (c_{Fz}), and pitching moment about pylon base (c_{My}) over *Re*.

According to Schlichting and Truckenbrodt (1969, p. 72 et seqq.), a linear, increasing pressure toward the edge of attack can be assumed as pressure distribution for even plates at small angles of wind attack. With this approach and taking the measured loads into account, the according pressure distribution was determined and applied to the FEM model. An average deflection of the mirror panel of 4° was calculated.

For nominal inclination of 4° and low Re_d= $0.45 \cdot 10^6$, the coefficients of drag (c_{Fx}), lift (c_{Fz}), and pitching moment (c_{My}) were measured and are given in Fig. 62 as single measuring points.

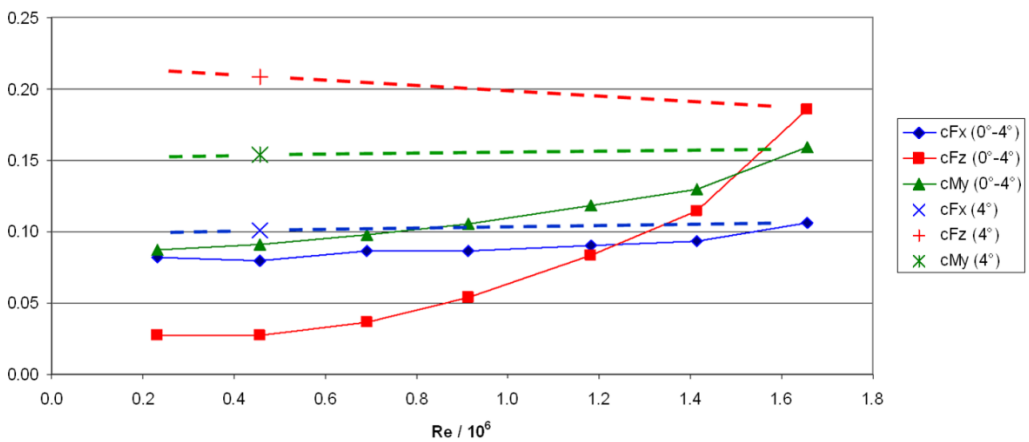

Fig. 62: Wind load coefficients for various *Re* and resulting 0°-4° inclination of the mirror panel due to deformation (solid lines) and for 4° inclination at low *Re*

The solid lines of Fig. 62 represent the measured values for the nominal panel inclination of 0º, but with the actual load induced inclination between 0º (low *Re*-number) and 4º (highest *Re*-number). If the measured value at Re_d=

$0.45 \cdot 10^6$ at nominal panel inclination of 4º (which needs no correction) is compared with the measured value at $Re_d = 1.7 \cdot 10^6$ at nominal panel inclination of 0º (which has to be corrected to 4º) it can be concluded that the design-driving components drag, lift and pitching moment coefficients are not depending on *Re* (dashed line).

5.1.3.2 Discussion

At the stow position, the drag force F_x, lift force F_z , pitching moment M_y and hinge moment M_{Hy} reach their maximal value at storm conditions. Thus, their values at stow position are relevant for the design of heliostats. Since M_{Hy} is hard to measure directly, it is calculated by the drag force F_x and by the moment at the pylon feet M_y (Peterka and Derickson, 1992, p. 10). As the wind load coefficients of F_x and M_y show no *Re* dependency, the wind load coefficient of M_{Hy} is not *Re* dependent as well.

cF_z shows a slight decrease with increasing *Re* (dashed line). However, compared to the increase due to deflection (solid line), it is small and is within the range of the uncertainties of the method.

5.1.4 *Conclusions*

No design-relevant *Re* dependency of the wind load coefficients of heliostats at stow position was measured. Thus, it is valid to determine the wind load coefficients at conventional boundary layer wind tunnels at low *Re*.

However, for the layout of heliostats their possible deflection through wind loads and the resulting increase of the inclination of the mirror panel at high *Re* must be considered. Hence, stiffness and damping of the structure must be high enough to avoid torsional divergence, flutter, galloping and resonance due to vortex shedding of the structure itself or of upstream structures at any possible *Re* number (Cook, 1985).

The results of this investigation cannot be transferred to solar trough collectors because the round shape of the trough is surely of bigger influence than the torque tube of a heliostat. Hosoya et al. (2008, p. 39 et seq.) performed wind tunnel measurements for trough collectors with various *Re*, but the critical *Re* was not reached (compare with Fig. 55). An approval of the *Re* independency of the wind load coefficients of solar trough collectors is still absent and could be also examined in the High Pressure Wind Tunnel of Göttingen.

Acknowledgments

The authors thank the DLR division “Energy” for the financing of the measurements.

5.2 Turbulent Energy Spectra

This section is reproduced from [Pfahl, A., Zaschke, M., Geurts, C.P.W., Buselmeier, M., 2018. "Impact of Turbulent Energy Spectra Characteristics on Wind Loading of Heliostats and PV Trackers in Stow Position". Under review].[5]

Abstract

Panels of PV trackers and heliostats are usually aligned horizontally for stow in order to minimise the area of wind attack. Aerodynamically, they constitute the simple case of a flat plate aligned in mean wind direction and submerged in a turbulent atmospheric boundary layer. Due to the turbulence of the oncoming flow, the instantaneous angle of attack varies. In combination with separations especially at the leading edge this results in significant fluctuating lift forces and hinge moments. Thus, correct modelling of the atmospheric boundary layer turbulence is of particular importance for wind load predictions.

Due to their small size, PV panels and heliostats have to be modelled at unusually big geometric scales in the wind tunnel (10 to 30 times above common geometric model scales). This makes it impossible to correctly capture the low-frequency part of the turbulent energy spectra because the corresponding wavelengths would be far above the standard wind tunnel width and height. The purpose of this study is to investigate the impact of this mismatch on the wind load coefficients.

At first, an approach is described and validated to overcome the scale mismatch. Within this approach it was observed that matching of either the longitudinal or the vertical turbulence spectrum could be reached, but not these two simultaneously. To investigate the impact of the scale mismatch, wind tunnel tests with pronounced differences of the ratio between vertical and longitudinal turbulence intensity were performed.

Admittance functions and the observed strict dependency of the wind load coefficients on the vertical turbulence intensity confirm that the match of the vertical turbulence intensity is decisive for the peak lift force and peak hinge moment. Furthermore, they show that spectra mismatches are of small impact, at least for the investigated boundary conditions. Besides, it became clear that for heliostats of different height it is important to take different turbulence intensities into account because the turbulence intensity varies significantly with height.

[5] The BLWT measurements were defined and its results proofed and analysed by the main author. The preparation and execution of the measurements were performed by the co-authors from Wacker Engineers.

As a conclusion, wind tunnel tests of heliostats in stow lead to realistic lift and hinge moment coefficients in spite of mismatches in turbulent energy spectra as long as the vertical turbulence intensity at elevation axis height is matched (for the range of boundary conditions investigated in this study).

Keywords: heliostat, PV-tracker, horizontal flat plate, turbulent energy spectra, turbulence intensity, boundary layer wind tunnel, vortex street

Nomenclature

A	[m²]	mirror/PV panel surface
a	[m]	distance of cylindrical tube to heliostat/PV tracker model
b	[m]	width of mirror or PV panel (perpendicular to wind direction)
c	[-]	in the present study always *peak* wind load coefficient for T_0 = 3s
d	[m]	diameter of circular cylindrical tube for vortex street generation
D	[m]	diameter of eddy
$D_{encl.}$	[m]	diameter of eddy that safely encloses the heliostat mirror panel
D_{max}	[m]	diameter of eddy that corresponds to BLWT restrictions
f	[1/s]	frequency of wind speed fluctuation
f^*	[-]	normalised frequency of wind speed fluctuation ($f^* = fh/U_{mean}$)
F_z	[N]	in the present study always *peak* lift force
h	[m]	chord length of mirror or PV panel (in wind direction)
H	[m]	height of mirror/PV panel in stow position
I_u	[-]	turbulence intensity of longitudinal wind component at height H
I_w	[-]	turbulence intensity of vertical wind component at height H
Je	[-]	Jensen number
L^x_u	[m]	length scale of turbulence in x-direction relating to u-component
L^x_w	[m]	length scale of turbulence in x-direction relating to w-component
M_{Hy}	[Nm]	in the present study always *peak* hinge moment
p	[N/m²]	dynamic pressure
r		reference
S_{ii}	[m²/s]	S_{uu} or S_{ww} respectively
S_{uu}, S_{ww}	[m²/s]	spectral density functions of u and w-components
St	[-]	Strouhal number
T	[s]	period of time for determination of autocorrelation function

T_0	[s]	averaging time: observation period over which atmospheric wind speeds are measured (as mean values of this time interval) and measuring period for the determination of the peak wind load coefficient
T_{filter}	[s]	effective filtering time resulting from BLWT spatial restrictions
U_{mean}	[m/s]	mean streamwise wind speed component for T_0 and H
U_i	[m/s]	streamwise wind speed at height z_i
u	[m/s]	fluctuating streamwise velocity component
w	[m/s]	fluctuating vertical velocity component
x	[m]	Cartesian coordinate, streamwise
y	[m]	Cartesian coordinate, lateral
z	[m]	Cartesian coordinate, vertical
z_0	[m]	aerodynamic roughness length
α	[-]	factor in modified von Karman equations
β_1, β_2	[-]	factors in modified von Karman equations
γ_u, γ_w	[-]	auxiliary variables for modified von Karman equations
ρ	[kg/m³]	density of air
σ_u	[m/s]	standard deviation of streamwise velocity fluctuations
σ_w	[m/s]	standard deviation of vertical velocity fluctuations
φ	[rad]	wind attack angle with horizontal plane or elevation
χ_{Fz}^{w}	[-]	admittance function of lift for vertical velocity component
χ_{MHy}^{w}	[-]	admittance function of hinge moment for vertical velocity component
ω	[1/s]	angular frequency = $2\pi f$
BL1-3		BLWT configuration, number 1, 2 or 3
BLWT		boundary layer wind tunnel
CYL1-14		measurement with vortex street generation by cylinder, number 1 to 14

5.2.1 *Introduction*

Photovoltaics and solar thermal power plants are a promising option to cover significant parts of the increasing energy demand. The main solar thermal power technologies are parabolic trough, tower, dish, and linear-Fresnel

systems. At solar tower plants, sunlight is concentrated by mirrors tracking the sun in two axes, the so-called heliostats. The heliostats reflect the sun rays to the top of a tower, where a receiver absorbs the radiation and supplies thermal energy to a power cycle. Alternatively, the energy is used by chemical thermal processes or concentrated photovoltaics. The heliostat field is the main cost factor of solar tower plants. It is exposed not only to the sun but also to wind. For a cost efficient dimensioning of the heliostats, the wind loads must be known. The highest loads on the structure occur at storm conditions. At these conditions the heliostats are horizontally aligned to minimise the surface of wind attack (stow position). This is also the case for PV-trackers.

Wind loads on photovoltaic panels and heliostats can be analysed by full scale (field) measurements (Geurts and Blackmore, 2016), wind tunnel testing (Pfahl and Uhlemann, 2011; Strobel and Banks, 2014; Stenabaugh et al., 2015), or numerical simulation with Computational Fluid Dynamics (CFD) (Blocken, 2014; Jubayer and Hangan, 2016; Reina and De Stefano, 2017). In the past decades, several wind tunnel investigations have been published to enable heliostat developers to determine the wind loads. Peterka et al. (1989) and Peterka and Derickson (1992) introduced a method for the determination of wind loads on heliostats of arbitrary size and of aspect ratio (height to width of mirror surface) of approximately one. Wind load coefficients were given for an isolated heliostat for any possible elevation angle of the mirror panel and any wind direction. The strong impact of the turbulence intensity on the peak and even on the mean loads was shown by comparison of several BLWT investigations with different longitudinal turbulence intensities. Furthermore, formulas were given to estimate the impact of a wind fence and of heliostat rows upwind to the heliostat (see also (Peterka et al., 1986)). The results of full scale measurements by Sment and Ho (2014) bear resemblance to these formulas regarding drag force. Wu et al. (2010) investigated the effect of small gap (5mm – 40mm) between the facets on the wind loads and considered these to be of negligible impact because the difference was in the range of measurement accuracy. In contrary, wide gaps cannot be neglected (Pfahl et al., 2011b), as a gap of 0.5 m was shown to lead to an increase of the peak hinge moment in the range of 20% compared to a closed mirror panel. The dependency of the wind load coefficients on the aspect ratio of the mirror panel was determined by Pfahl et al. (2011a). The wind load components depend significantly on the aspect ratio of the panel. Therefore the aspect ratio must be considered at the layout of the components of solar trackers. The general assumption that wind loads on heliostats are Reynolds number independent (for Reynolds numbers above a value at which separation at the

edges occurs, (Plate, 1982)) was validated by Pfahl and Uhlemann (2011). Gong et al. (2012) presented a method to determine dynamic effects using time series of the wind pressure distribution on the mirror panel (gained by wind tunnel tests) for a transient finite element (FEM) simulation of structural deformations. A significant impact of dynamic effects was observed especially for orientations with the mirror panel parallel to the wind direction. Approaches to reduce wind loads on heliostats by shock absorbers and fence like structures around the mirror panel were presented by Pfahl et al. (2014). Reductions of the peak wind loads of heliostats in horizontal stow position of 30% and of 40%, respectively, could be reached by these measures.

In these previous investigations, the impact of the mismatch of the turbulent energy spectra between wind tunnel (reduced) scale and full scale was not addressed. Especially for the stow position with low mean load and high peak load values (resulting from turbulence), a correct modelling of the atmospheric boundary layer turbulence is expected to be important. Usually, only the matching of the longitudinal turbulence intensity and spectrum is accounted for. However, for horizontal flat structures the vertical wind load component is presumably of higher impact. For flat building roofs for example, a significant impact of the vertical wind angle of attack on the peak-suction pressures near the roofs corner was measured (Wu et al., 2001).

To achieve similarity of the approach flow in a scale experiment, the profiles of mean wind speed and longitudinal, lateral and vertical turbulence intensity, as well as the turbulent energy spectra should be appropriately scaled. However, in general practice of BLWT measurements of heliostats this is not the case. Banks (2011) noted that in common wind tunnel tests for solar power assemblies, matching of the spectra is poor because of the following reason: Due to their small size, heliostats need to be modelled at larger scales (typical scales are 1:10 – 1:50) which are not in compliance with the typical wind tunnel flow scales (1:100 to 1:300). This large model scale is needed to model the details of the structure in sufficient detail and to locate the model at a height where mean velocity and turbulence intensity are well matched. For heights smaller than the average height of the roughness elements the assumptions leading to the logarithmic vertical mean wind speed profile formula are not valid (Arya, 1982).

Matching of the vertical mean wind speed profile is reached by similarity of the Jensen number (Jensen, 1958):

$$\mathrm{Je} = \frac{H}{z_0}$$

Where H is a characteristic height (here: the height of the panel) and z_0 the aerodynamic roughness length. Hence, for bigger model scales the roughness length must be increased to reach matching of the Jensen number and, as a consequence, matching of the vertical mean wind speed profile. The correct modelling of the vertical mean wind speed profile has a profound effect on the pressure distribution on buildings and on heliostats with vertical orientation of the mirror panel (Jensen, 1958). For heliostats in stow with a panel thickness more than 100 times smaller than the panel width and height it is assumed that it is of less impact. However, when just inserting a large scale heliostat into a model boundary layer configured for smaller scales at a specified roughness length, the turbulence intensity at heliostat height will generally be lower than its target value. Aly and Bitsuamlak (2013) investigated the scale effect on ground mounted solar panels of inclination angles of 25° and 40° and found an impact on the peak values at big model scales (1:5 and 1:10). The peak values of big models were lower than the peak values of the 1:20 model because the big models were located in a region of lower turbulence intensity. Very small models (1:50) led to erroneous results as they were located too close to the ground where the wind conditions were not accurately reproduced.

Matching of the turbulence intensity can be achieved by modifying the roughness elements in the wind tunnel. However, an increased roughness length leads to a shift of the peak of the energy spectrum towards smaller eddy scales (= towards higher frequencies) compared to full scale measurements of same turbulence intensity, see Fig. 63, left, because big eddies corresponding to low frequencies of the spectra do not “fit” into the wind tunnel (Fig. 64) and are missing. For a cube it was shown that this shift has a significant impact on the pressure distribution on the top of the cube (Richards et al., 2007).

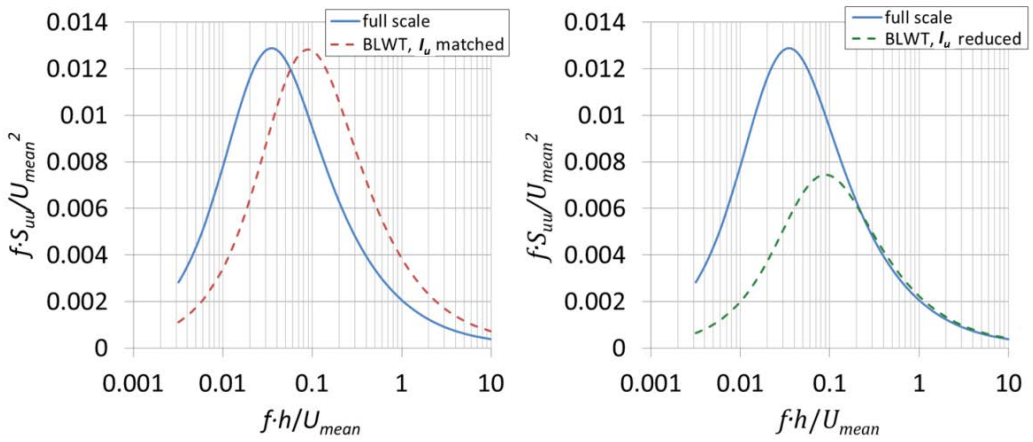

Fig. 63: Left: Comparison of energy spectra of the longitudinal velocity component for large model scale when turbulence intensity is matched (blue line: full scale, red dotted line: BLWT). Right: Reduced turbulence intensity for matching of the spectra for small turbulence length scales (blue line: full scale, green dotted line: BLWT with reduced I_u) (Dyrbye and Hansen, 1997)

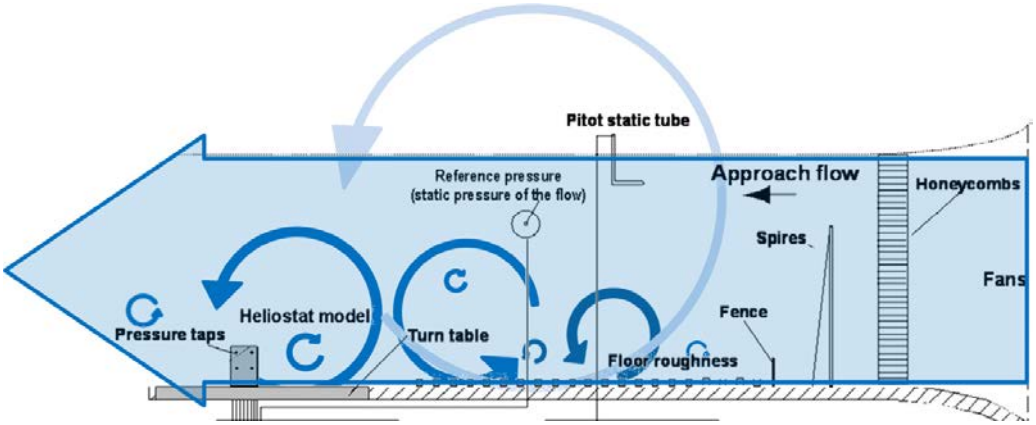

Fig. 64: Schematic of eddies and section through the atmospheric boundary layer wind tunnel. The size restrictions of the tunnel limit the size of eddies that can be simulated.

An approach to obtain proper conditions when working with "too-large" heliostat models is to focus on the spectral characteristics and to attempt to match the high-frequency part of the spectrum (Dyrbye and Hansen, 1997), see Fig. 63, right. This may require to further reduce the turbulence intensity. However, the latter approach leads even more to an underestimation of the impact of larger scales (which cannot be fully modelled due to restricted size of the wind tunnel).

According to Banks (2011) these underestimated larger scales in the BLWT do not need to be properly modelled as long as it is assured that they represent eddies which are big enough to engulf the entire structure and to cause a quasi-steady wind load response of the structure. This modified physical modelling requires a modified evaluation procedure where the quasi-steady gust wind (typically the three-second gust wind) is used as reference wind velocity instead of the mean-hourly or ten-minute-average wind speed. Since this method requires only a correct modelling of the smaller-scale turbulence (with eddies equal to and smaller than the assumed quasi-steady 3 s eddies) it is referred to as “high-frequency spectrum matching method” (Banks, 2011). This approach was applied by Aly (2016) to reduce discrepancies between CFD simulations and BLWT measurements of wind loads on solar panels. The corresponding maximum three-second mean wind speed would have to be taken into account for the calculation of the maximum loads. It can be estimated with (SEI/ASCE 7-02, 2003) or (Durst, 1960) respectively if three-second mean wind speed values of the site are not available. For example, the ratio of the maximum 3 s mean wind speed to the maximum hourly mean wind speed at 10 m above ground in open country is 1.54 (SEI/ASCE 7-02, 2003, Figure C6-2).

The purpose of this study is to investigate the impact of the BLWT scaling mismatch in turbulent energy spectra on lift force and hinge moment of heliostats and PV trackers in stow. Therefore, at first the shift of the longitudinal spectrum (of full scale and BLWT measurements) is avoided by reducing the observation and averaging time to three seconds. By this, only frequencies higher than the frequency corresponding to three seconds are measured at full scale which are not too big for to be simulated by the BLWT. Hence, it is expected that matching of the complete spectrum can be achieved. Then it is investigated whether the remaining differences between the turbulent energy spectra of the BLWT and of the standard atmospheric boundary layer are of significant impact. Therefore wind tunnel tests with different ratios of vertical and longitudinal turbulence intensity and different shapes of the spectra are performed. The tests cover three typical boundary-layer configurations (first results presented by Pfahl et al. (2015)) as well as synthetic situations with pronounced peak frequencies generated by circular cylinders of two different diameters and varied distance to the heliostat. With increased distance the peak frequency reduces as well as the amplitude of the spectra (Roshko, 1992).

In the annex of this section (section 5.2.5), basic definitions and information about spectra, averaging time, wind load coefficients, and admittance

functions are given to enable also readers specialised in solar energy (and not in wind engineering per se) to follow the reasoning.

5.2.2 *Method*

5.2.2.1 Boundary layer wind tunnel configurations

The cross-sectional dimensions of the test section of the atmospheric boundary layer wind tunnel is width x height = 1.80 m x 2.00 m. Roughness elements were placed along an upstream fetch of 8 m (Fig. 65). This length is sufficient to achieve a boundary layer thickness of more than five heliostat heights. For the investigations a heliostat of A = 19 m² with an elevation axis height H = 2.4 m was chosen and a model scale 1:20. In order to gain insight into the relation between heliostat wind loading and turbulence of the approach flow, three roughness configurations with different turbulence characteristics were chosen. For this research, the turbulent characteristics at heliostat height ($z = H$ = 12 cm in the wind tunnel and 2.4 m at full scale) were taken as reference values.

The different turbulence conditions were achieved by successively removing turbulence generating devices from the boundary layer wind tunnel (Fig. 65). The BLWT configurations BL1 and BL2 lead for typical model scales of 1:100 to 1:300 to realistic vertical mean wind speed profiles (Fig. 66) and spectra. BL3 was achieved by maintaining the turbulence-generating devices at the wind tunnel entrance while removing the roughness elements from the wind tunnel bottom. Thus, this configuration does not represent an equilibrium boundary layer but a nearly uniform vertical mean wind speed profile with a comparatively low level of upstream-generated turbulence at heliostat height. To study the dependency on the different turbulence conditions, extensive wind pressure measurements along the upper and lower surface of the heliostat and high resolution (2 kHz) turbulent incident velocity measurements with hot wire anemometers in the absence of the heliostat at its position have been carried out.

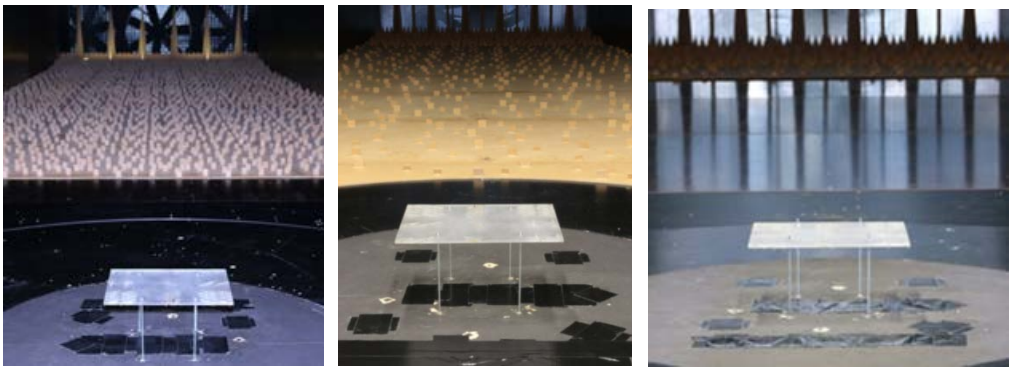

Fig. 65: Spires, fence and roughness elements in wind tunnel to generate boundary layers of 22% (BL1, left), 18% (BL2, middle) and 13% (BL3, without roughness elements, right) longitudinal turbulence intensity I_u at heliostat height $z = H = 12$ cm

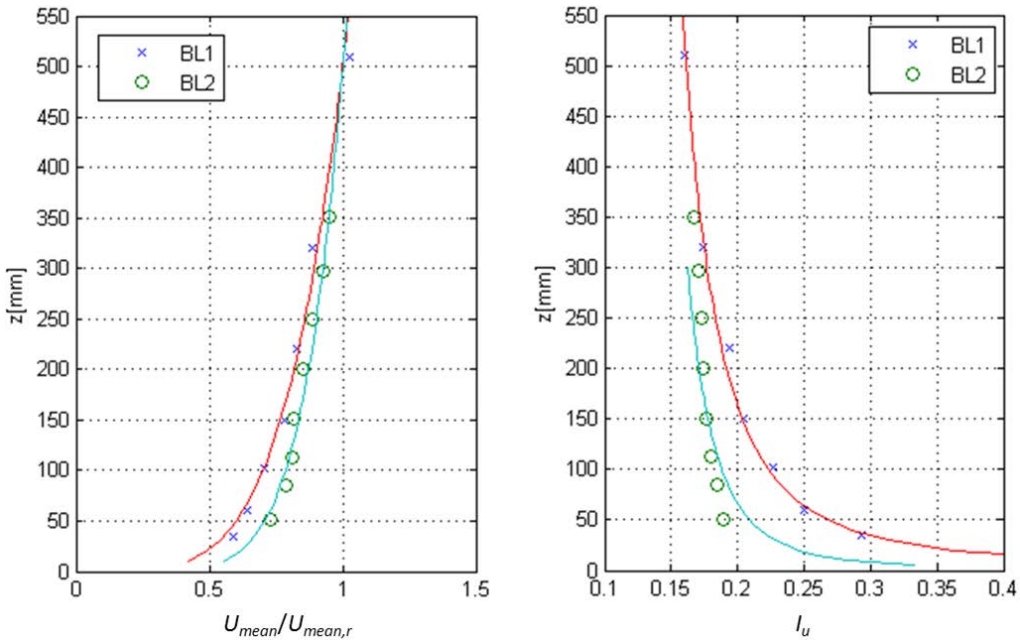

Fig. 66: Velocity profiles (left) and longitudinal turbulence intensity profile (right) for BL1 and BL2

Table 13 gives the measured turbulence intensities of the three BLWT configurations and corresponding values at full scale of aerodynamic roughness length, mean wind speed, turbulent length scales and filtering time. For all configurations a mean wind speed at full scale of 20 m/s at z = 10 m was assumed.

The low frequencies of the standard longitudinal spectra cannot be simulated in the BLWT because of the restricted height of the wind tunnel of 2 m which precludes eddies rotating about the y-axis and bigger than 2 m in diameter to develop. This corresponds to a maximum size of the eddies of D_{max} = 40 m at full scale (scaling factor 1:20). With equations (5.15) and (5.16) and the mean wind speed U_{mean} for elevation axis height H = 2.4 m (BL1: 12.6 m/s, BL2: 14.4 m/s, BL3: 17.6 m/s) an effective filtering time T_{filter} in the range of 3 s (BL1: 3.2 s, BL2: 2.8 s, BL3: 2.3 s) follows (see Table 13). Note that for an averaging time of T_0 = 3 s usually extensive meteorological data are available. For the maximum mean speeds of typical sites in the range of 40 m/s filtering with T_{filter} ≈ 1.5 s would be required but for this averaging time usually no wind speed data are available. However, the following shows that also with T_0 = 3 s good agreement between full scale and BLWT spectra is achieved.

Table 13: Parameters of BLWT configurations BL1, BL2 and BL3 at full scale

Parameter	**BL1**	**BL2**	**BL3**
I_u	21%	18%	13%
I_w	13%	10%	8%
I_w / I_u	0.62	0.58	0.64
z_0 (corresponding to I_u)	8 cm	4 cm	1 cm
$U_{mean,H=2.4m}$ (ESDU 82026, (7.4) and (A1.10))	12.6 m/s	14.4 m/s	17.6 m/s
L_u^x (ESDU 85020, Figure 3a/(A2.14))	18 m	23 m	33 m
L_w^x (ESDU 85020, Figure 3a, (7.2) and (7.4))	1.5 m	1.9 m	2.8 m
T_{filter} (equations (5.2.25) and (5.2.26))	3.2 s	2.8 s	2.3 s

The graphs of the filtering function given by equation (5.2.23) with T_0 = 3 s and with the mean wind speeds for BL1-3 given by Table 13 are shown in Fig. 67.

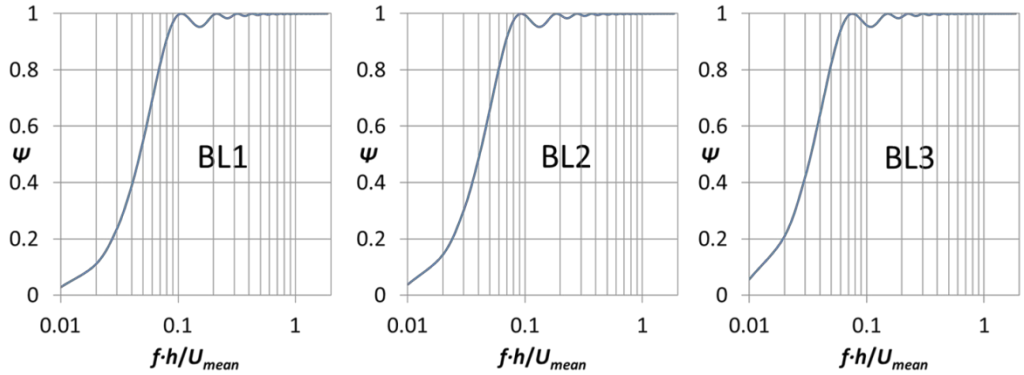

Fig. 67: Filter for reduced observation period T_0 = 3s given by equation (5.2.23) (ESDU 83045)

5.2.2.2 Vortex street generation by circular tubes

To investigate the impact of the ratio I_w/I_u and of the shift of the peak values of the spectra tests in a (non-boundary layer) wind tunnel have been performed. In these tests, vortex streets have been generated by a circular cylindrical tube mounted across the whole wind tunnel width. Tubes of two different diameters *d* were used. It was not intended to achieve turbulence according to the atmospheric boundary layer but flows with pronounced differences in the ratio I_w/I_u. Therefore, the distance of the flat plate to the tube *a* was varied between 60 cm and 220 cm (Fig. 68) and ratios I_w/I_u between 0.71 and 0.93 were achieved. The cross section of the wind tunnel for these measurements is 1.3 m x 1.3 m. No spires, fence and roughness elements were used. For determination of the spectra, turbulent incident velocity measurements were performed at a frequency of 2 kHz with hot wire anemometers in the absence of the heliostat at the heliostat position.

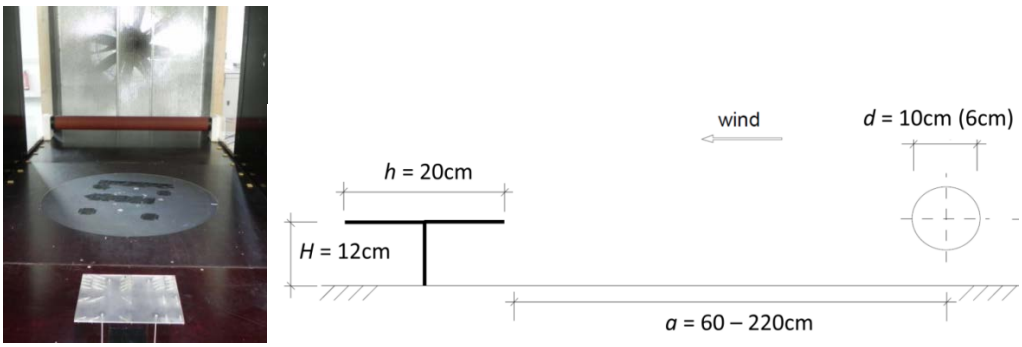

Fig. 68: Test set up for measurements of flat plate in vortex street generated by circular cylindrical tubes

The diameter of the tube *d* and the free stream mean wind speed upstream of the cylinder at the tubes height determine the frequency of the peak value of the spectra. Two diameters *d* = 6 cm and *d* = 10 cm were investigated. *d* = 6 cm was chosen to achieve vortices with a diameter $D_{encl.}$ that safely (150%) encloses the heliostat model mirror panel of *h* = 20 cm completely:

$$D_{encl.} = 1.5h = 30\text{cm} \tag{5.2.1}$$

An eddy may be represented as a mass of fluid with a certain diameter rotating around a centre (Cook, 1985, p.20 et seqq.). The diameter D_{fpeak} of eddies causing the peak frequencies can be estimated:

$$D_{f_{peak}} = \frac{U_{mean}}{f_{peak}}. \tag{5.2.2}$$

With

$$f_{peak} = \text{St}\frac{U_{mean}}{d}, \tag{5.2.3}$$

$$D_{f_{peak}} = D_{encl.}, \tag{5.2.4}$$

From equations (5.2.1), (5.2.2), and $\text{St} = 0.2$ for circular cylinders it follows:

$$d = \text{St}D_{encl.} = 6\text{cm}. \tag{5.2.5}$$

With equations (5.2.1) and (5.2.2) this leads to a normalised frequency of:

$$\frac{f_{peak} \cdot h}{U_{mean}} = \frac{h}{D_{encl.}} = \frac{1}{1.5} = 7 \cdot 10^{-1}. \tag{5.2.6}$$

For the second diameter a value of *d* = 10cm was chosen which leads with equation (5.2.3) to a peak value of the normalised frequency of:

$$\frac{f_{peak}h}{U_{mean}} = \frac{\text{St}\frac{U_{mean}}{d}h}{U_{mean}} = \text{St}\frac{h}{d} = 4 \cdot 10^{-1}. \tag{5.2.7}$$

These values are in good agreement with the measured peak frequencies (Fig. 73; Fig. 74).

5.2.2.3 Pressure distribution on horizontal flat plate

For the investigations a heliostat of *A* = 19 m² and of elevation axis height *H* = 2.4 m was chosen and a model scale 1:20. The dimensions of the sharp edged measurement plate of 2 mm thickness are *b* x *h* = 24 cm x 20 cm for both wind tunnels (see Fig. 65 and Fig. 68). The plate was located at a height *H* = 12 cm. Based on former peak wind load measurements (Gong et al., 2012; Pfahl et al., 2011a), the highest pressure gradients occur within a distance to the upwind edge of ¼ of the facet height *h* and near the sideward

edges. Hence, pressure measurement points were foreseen especially in these regions (see Fig. 69). Two rows of measurement points were located as close as possible to the frontal edge because the highest pressure gradient occurs there. The pressures at the different positions of the panel were measured on the top side and on the bottom side separately and simultaneously with a sample frequency of 2 kHz and correction of the error caused by the damping of the tubes. In total, 70 pressure taps were used. At former measurement campaigns (Pfahl et al., 2011a) it was observed that such a pressure tap density leads to good agreement of pressure taps and force balance measurements, having a sufficient spatial resolution and not too much disturbance of the flow by the pressure tubes.

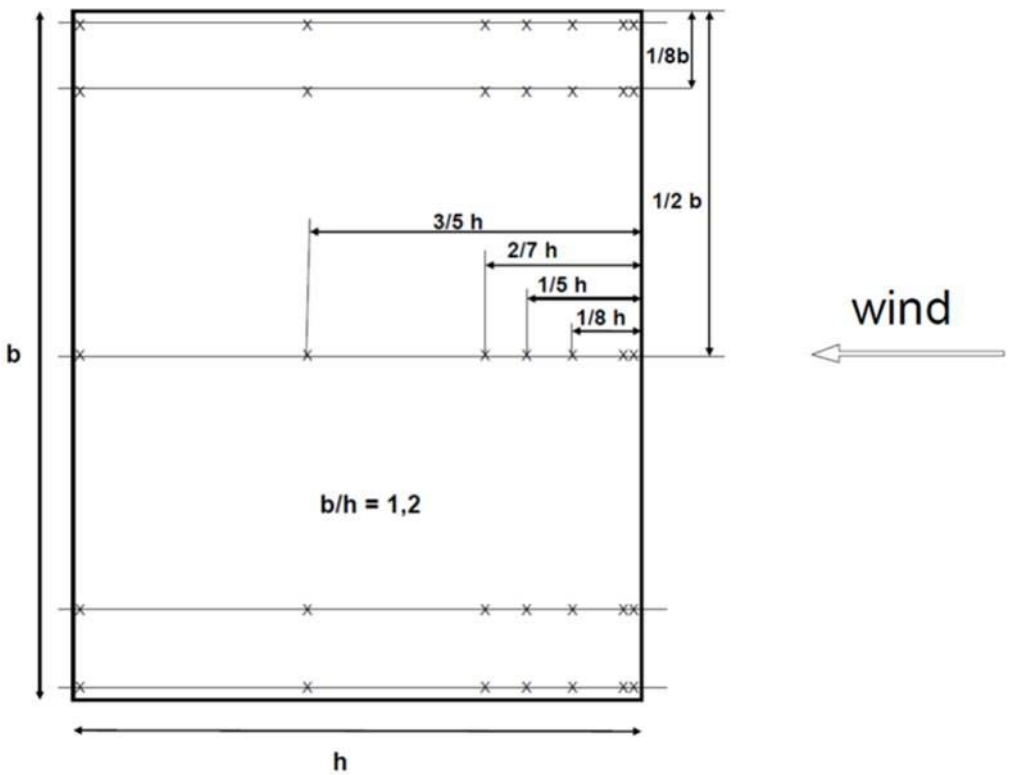

Fig. 69: Distribution of pressure measurement points on flat plate; *b* = 24 cm, *h* = 20 cm

For the determination of the peak values each measurement of 600 s duration was split into 200 windows with measurement period T_0 = 3 s. For each window the peak value was determined. From all peak values the average was calculated to achieve the mean peak value (Aly and Bitsuamlak, 2013). The peak wind load and pressure coefficients for T_0 = 3 s given in the following

are these mean peak net values. The wind load coefficients were calculated by integration of the single net pressure values of the different pressure measuring points weighted with the area they represent.

5.2.3 *Results and Discussion*

5.2.3.1 Results

5.2.3.1.1 Turbulent energy spectra

The graphs with solid lines of Fig. 70 show the turbulent energy spectra of the measured longitudinal (left) and vertical (right) velocity components S_{uu} and S_{ww} of BL1 (upper blue line), BL2 (middle green line) and BL3 (lower red line) at a (heliostat) height of $z = H = 0.12$ m in BLWT. The dashed lines of Fig. 70 show the standard longitudinal energy spectra (for $z = H = 2.4$ m) according to ESDU 85020 having approximately the same turbulence intensity I_u Fig. 70, left, shows (as expected) that the energy of the BLWT longitudinal spectra is shifted towards higher frequencies compared to the full-scale spectra (i.e. the relevant higher longitudinal frequencies contain too much energy). For the BL2 and BL3 vertical spectra also a shift towards higher frequencies compared to the standard spectra occurs, see Fig. 70, right. Hence, the eddies generated by the BLWT roughness elements of BL2 and BL3 are too small.

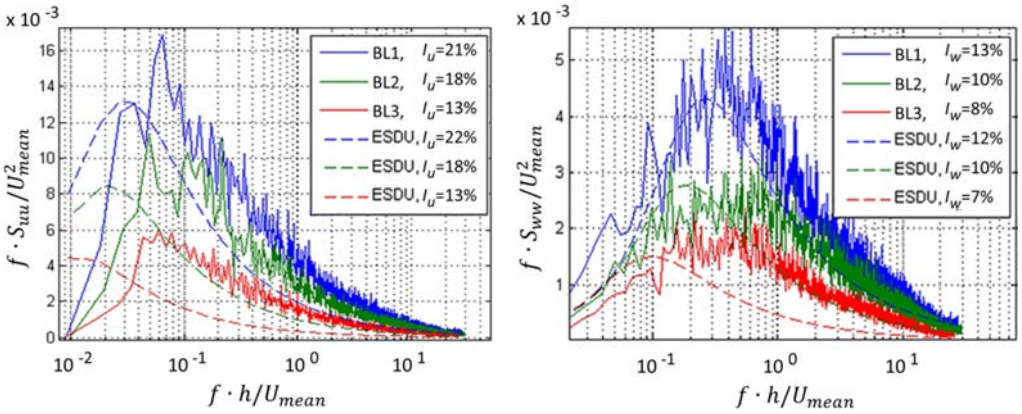

Fig. 70: Measured and standard (ESDU 85020) turbulent energy spectra of longitudinal (left) and corresponding vertical (right) velocity component; the standard spectra are given for T_0 = 1h and are shifted to lower frequencies compared to the BLWT spectra

The vertical spectra (Fig. 70, right) show most of the vertical turbulent energy is captured at normalised frequencies $f^* > 10^{-1}$. This means, eddies which are one order of magnitude bigger (or more) than the heliostat chord length h are of small impact on the vertical spectra. The reason is that the vertical wind

component at the height of the plate of such eddies is small (Fig. 71). Hence, these big turbulence structures impact mainly the longitudinal velocity component at the height of the plate and not the vertical one. The impact of the distance of the vortex core on the wind load coefficients was observed also in other contexts, e.g. helicopter blade wake vortices (Ilie, 2009). The aerodynamic coefficients decrease significantly with increasing distance of the rotating rotor blade to the core of the vortex hitting the rotor blade.

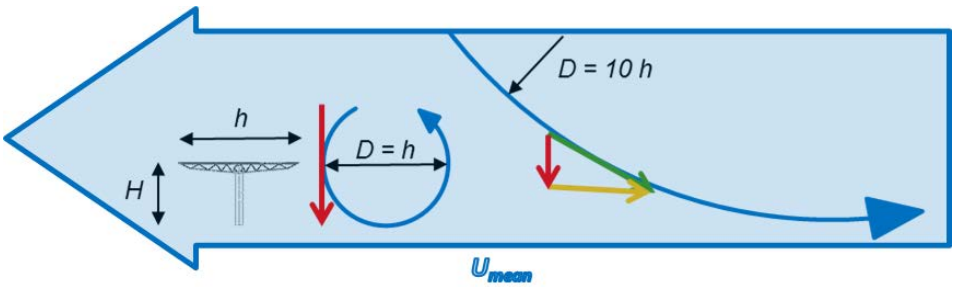

Fig. 71: Vertical velocity component (red) of eddies of diameter *D* equal to chord length *h* ($f^* = 10^0$), (small blue vortex with *D* = *h* and large red vertical component, left), and of eddies of diameter *D* equal 10 times the chord length *h* ($f^* = 10^{-1}$), (section of big blue vortex with *D* = 10 *h* and small red vertical velocity component, right)

An averaging and filtering time of approximately $T_0 = T_{filter} \approx 3$ s corresponds to the spatial BLWT restrictions (see section 5.2.2.1). The corresponding filters (equation (5.2.23)) applied to the ESDU full scale spectra of Fig. 70, dotted graphs, lead to the modified dotted graphs of Fig. 72. After filtering, the full scale and the BLWT longitudinal spectra are in good agreement. The filters are of lower impact on the *w*-spectrum. The reason is that the energy of frequencies corresponding to $T_0 = 3$ s and higher (at full scale) is already low without filtering because of the small vertical velocity component at measurement height. Therefore, I_u is more reduced by the filtering than I_w. As a result, the ratio of vertical to longitudinal turbulence intensity is at full scale for $T_0 = 3$ s in the range of $I_w/I_u = 0.7$ while in the BLWT it is $I_w/I_u = 0.6$ as it should be for $T_0 = 1$ h (ESDU 85020, 4.2, equation (4.5)). Hence, good matching of turbulence intensity and spectra for $T_0 = 3$ s can be achieved with the roughness elements used only either for the longitudinal or for the vertical velocity component, but not for both simultaneously. The standard spectra shown in Fig. 72 are a compromise: Values for I_u of the standard spectra are too low while I_w are too high compared to the BLWT spectra. Furthermore, the BL2 and BL3 vertical spectra are still shifted towards higher frequencies in the relevant frequency range.

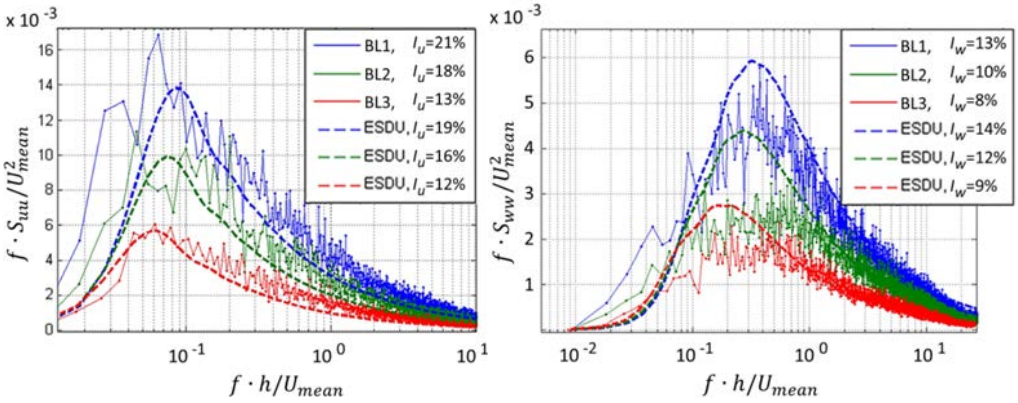

Fig. 72: Measured and standard turbulent energy spectra of longitudinal (left) and corresponding vertical (right) velocity component; the standard values are given for T_0 = 3 s and are in good agreement with the BLWT spectra

Wind tunnel measurements with vortex streets generated by a circular tube (described in section 5.2.2.2) were performed to investigate the remaining mismatches (too low I_w/I_u and shift of the vertical spectrum towards higher frequencies). They provide pronounced differences of the ratios I_w/I_u and of the peak frequencies to enable to analyse the impact of these differences on the wind load coefficients. Directly behind the circular tube the flow is dominated by (circular) eddies with their core centre near the plate's height which means that the vertical component is as large as the longitudinal one (Fig. 71) which results in $I_w/I_u \approx 1$. This value reduces with the distance to the circular tube because some eddies enlarge with distance. The biggest generated eddies can enlarge only in upward direction because the distance of the tubes to the ground is smaller than the radius of these eddies (equation (5.2.1)). The enlarged eddies (causing lower measured frequencies than the smaller eddies directly behind the tube) with their core centre significantly higher than the plate have only a small vertical but a high longitudinal velocity component at height of the plate (Fig. 71). Hence, I_w/I_u reduces with distance a.

As a further consequence, the peak frequency moves towards lower frequencies with increased distance a especially for the u-spectrum, see Fig. 73, left to right and Fig. 74, left to right (which is in good agreement with Shirakashi et al. (1988, Fig. 2)). Two diameters of the circular tube (d = 6 cm and d = 10 cm) were chosen for different values of the peak value frequencies (compare Fig. 73 with Fig. 74). The peak values of the spectra are getting less pronounced with increased distance to the tube a (compare left, middle, and right of Fig. 73 and of Fig. 74 respectively). This is a further difference of the

spectra of the different measurements. Their impact on the wind load coefficients will be discussed in section 5.2.3.2.2.

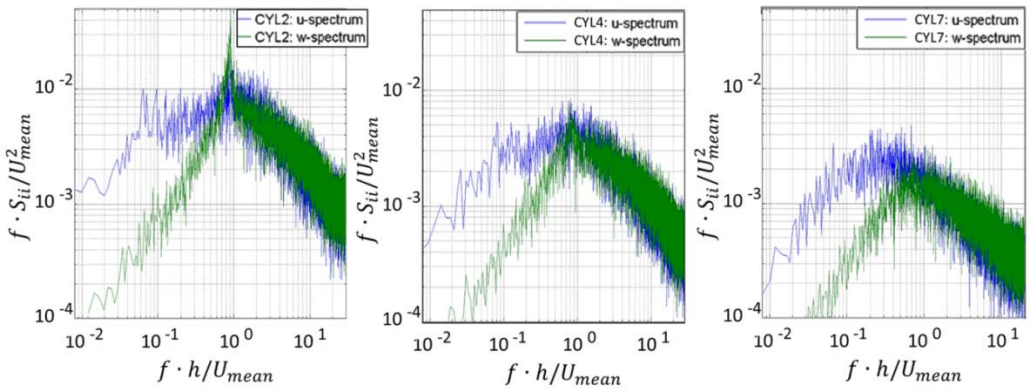

Fig. 73: Turbulent energy spectra of longitudinal (blue) and vertical (green) velocity component for *d* = 6 cm with *a* = 80 cm (left), *a* = 120 cm (middle) and *a* = 220 cm (right)

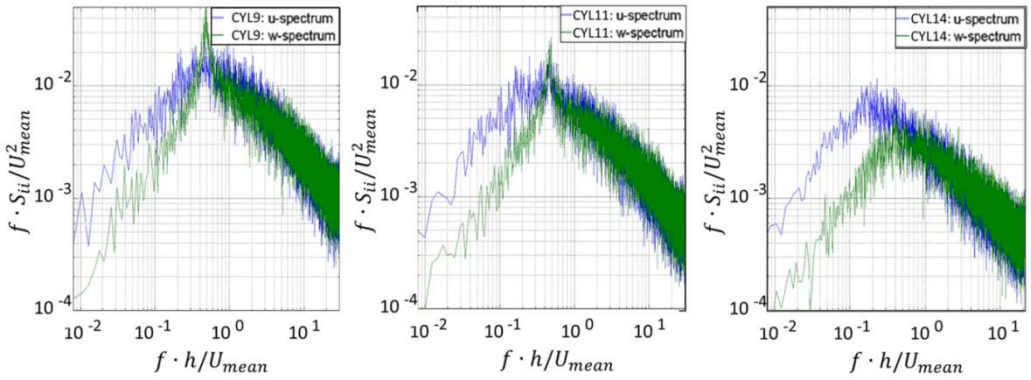

Fig. 74: Turbulent energy spectra of longitudinal (blue) and vertical (green) velocity component for *d* = 10 cm with *a* = 80 cm (left), *a* = 120 cm (middle) and *a* = 220 cm (right)

5.2.3.1.2 Turbulence intensities and wind load coefficients

The measured turbulence intensities and the resulting peak lift and hinge moment coefficients are given in Table 14. The time interval within which the peak wind load coefficients were measured is T_0 = 3 s (at full scale). The peak load coefficients increase with increasing turbulence intensity. The turbulence intensities decrease with the reduction of roughness elements (BL1 – BL3) and with the distance *a* to the circular tube and increase with increasing

diameter *d* of the circular tube. As expected, the ratio I_w/I_u reduces with the distance to the circular tubes *a*.

Table 14: Turbulence intensities and wind load coefficients (mean of absolute values of positive and negative peak values) of BLWT (BL1-3) and vortex street (CYL1-14) measurements for T_0 = 3 s

	d [cm]	***a*** [cm]	I_u [%]	I_w [%]	I_w/I_u	$\lvert c_{Fz}\rvert$	$\lvert c_{MHy}\rvert$
BL1	-	-	21	13	0.62	0.29	0.087
BL2	-	-	18	10	0.58	0.22	0.065
BL3	-	-	13	8.3	0.65	0.20	0.061
CYL1	6	60	23	20	0.89	0.49	0.15
CYL2	6	80	19	15	0.81	0.33	0.11
CYL3	6	100	16	12	0.77	0.25	0.078
CYL4	6	120	14	10	0.76	0.21	0.066
CYL5	6	140	12	9.0	0.76	0.18	0.057
CYL6	6	180	11	8.1	0.74	0.14	0.045
CYL7	6	220	9.8	7.0	0.71	0.13	0.041
CYL8	10	60	26	24	0.93	0.73	0.21
CYL9	10	80	22	20	0.90	0.51	0.15
CYL10	10	100	20	17	0.85	0.42	0.13
CYL11	10	120	18	15	0.82	0.36	0.11
CYL12	10	140	17	14	0.80	0.31	0.097
CYL13	10	180	15	12	0.76	0.25	0.077
CYL14	10	220	15	11	0.72	0.22	0.068

5.2.3.1.3 Pressure distributions

Fig. 75 to Fig. 77 show the peak pressure distributions on the flat plate averaged over its width for wind attacking from the right (note that torque tube and supporting frames and trusses are of impact on the pressure distributions but are neglected in these general investigations). The upper green line gives the distribution for the lower side of the panel, the middle blue one for the upper side and the lower red one the resulting net pressure distribution of both surfaces. Positive values indicate pressure acting in direction of the surface (pressure) and negative values indicate pressure acting away from the surface (suction). The net pressure is related to the upper surface with positive pressure values indicating pressure acting downwards. Positive or negative

peak lift and hinge moment coefficients occur for instances of time when the vertical component of the turbulence structures are attacking the panel from above or from below respectively. The figures show the peak pressure distributions for upward directed vertical wind component attacking the panel from below. The peak hinge moment coefficient results from (positive) pressure at the edge of the bottom side of the panel (positive value of the green line at the right edge) and from suction at the edge of the top side (negative values of the middle blue line). Both leads to an upward directed pressure acting away from the upper surface (negative values of the net pressure, red lower line).

The peak pressure distributions of the BLWT measurements are given by Fig. 75. With reduced turbulence intensities (from left to right) the peak pressure on the surfaces reduces.

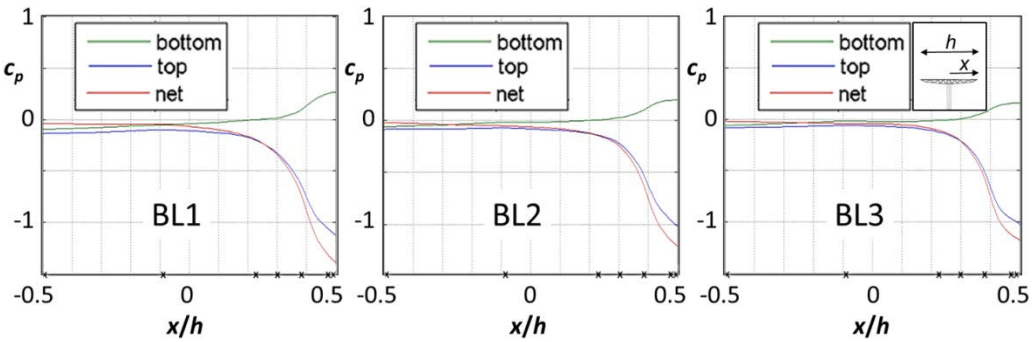

Fig. 75: Mean of all instantaneous pressure coefficient distributions during occurrence of peak hinge moment M_{Hy} (with measuring period T_0 = 3 s) averaged over heliostat width for BL1 (left), BL2 (middle) and BL3 (right) for vortex attacking from below (positive pressure at the bottom, suction/negative pressure at the top); pressure measurement point locations indicated by "x" on the x-axis

Fig. 76 shows the peak pressure distributions of the wind tunnel tests with vortex street generated by a circular tube with d = 6 cm. With the distance to the tube (left to right) the turbulence intensity and the peak pressure distribution reduces as well.

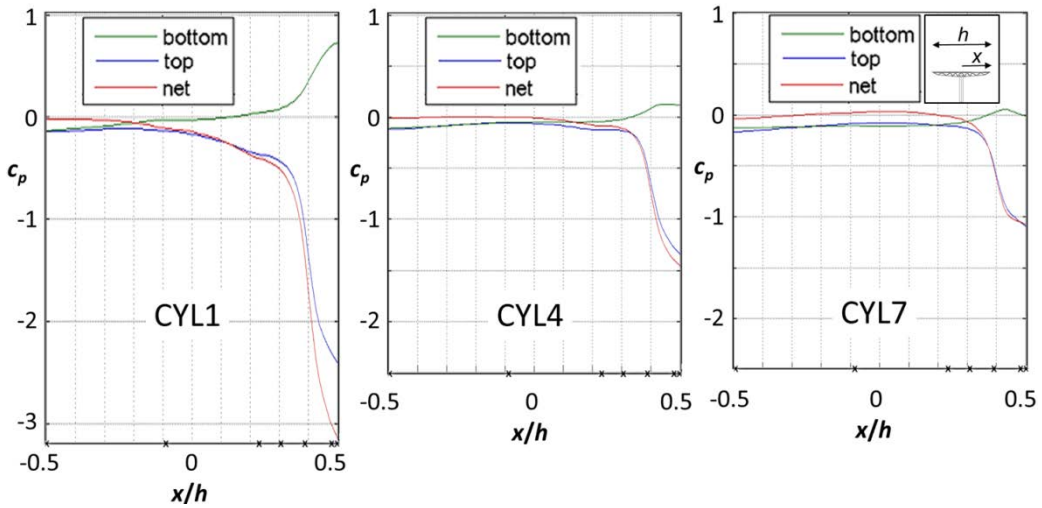

Fig. 76: Mean of all instantaneous pressure coefficient distributions during occurrence of peak hinge moment M_{Hy} (with measuring period T_0 = 3 s) averaged over heliostat width for a = 60 cm (left), a = 120 cm (middle) and a = 220 cm (right) with d = 6 cm for vortex attacking from below (positive pressure at the bottom, suction/negative pressure at the top); pressure measurement point locations indicated by "x" on the x-axis

Fig. 77 shows the peak pressure distributions of the measurements with a circular tube of d = 10 cm. The larger diameter leads to higher turbulence intensities and thus to higher pressure values on the surface (compare Fig. 76 and Fig. 77).

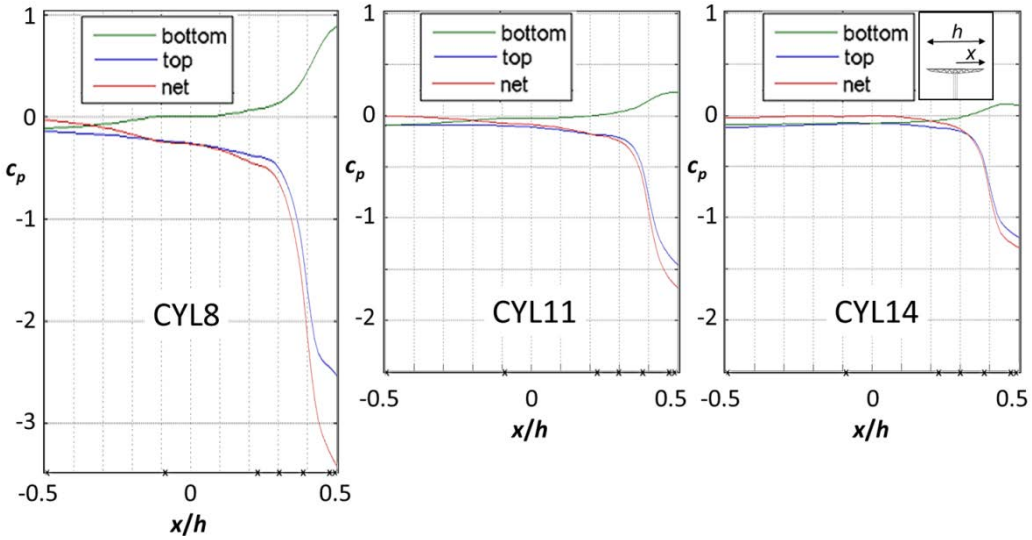

Fig. 77: Mean of all instantaneous pressure coefficient distributions during occurrence of peak hinge moment M_{Hy} (with measuring period T_0 = 3 s) averaged over heliostat width for *a* = 60 cm (left), *a* = 120 cm (middle) and *a* = 220 cm (right) with *d* = 10 cm for vortex attacking from below (positive pressure at the bottom, suction/negative pressure at the top); pressure measurement point locations indicated by "x" on the x-axis

5.2.3.1.4 Aerodynamic admittance functions

The derivatives of the load coefficients with respect to the angle of attack for the admittance functions (5.2.33) and (5.2.34) have been obtained from wind tunnel measurements with slightly varied elevation angle of the panel:

$$\frac{\delta c_{Fz}}{\delta \varphi} = 2.02 \qquad (5.2.8)$$

$$\frac{\delta c_{MHy}}{\delta \varphi} = 0.603 \ . \qquad (5.2.9)$$

Based on these values and the computed ratio of the load and vertical velocity spectra, the admittance functions shown in Fig. 78 have been obtained. As the plots show, they collapse very well for the different turbulence energy spectra of BL1, BL2 and BL3. Hence, the admittance functions do not depend on the turbulent energy spectra and therefore are applicable for the computation of wind load spectra also for other arbitrary turbulence input spectra.

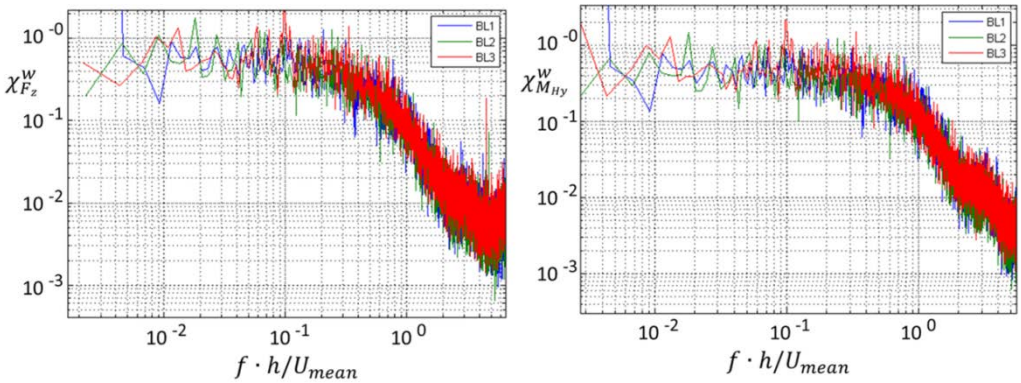

Fig. 78: Aerodynamic admittance functions of the lift (left) and the hinge moment (right) coefficients for the vertical velocity component

5.2.3.2 Discussion

5.2.3.2.1 Impact of turbulence intensity on peak wind load coefficients

It is assumed that for heliostats in stow the vertical velocity fluctuations are decisive regarding peak lift and hinge moment coefficients and not the longitudinal ones because of four reasons:

1. Mirror and PV panels are quite slick. Therefore, the pressure cannot act along the panel but only normal to it. Hence, the pressure vectors on the panels are normal to them.
2. Lift F_z and hinge moment M_{Hy} for trackers in stow result only from the pressure distribution on the panel. Pressures at other locations (mainly pylon) do not affect the hinge moment and are perpendicular to the lift force and therefore do not contribute to the lift force.
3. In stow, the normal pressure vectors on the panel are vertical.
4. The vertical velocity fluctuations are decisive for the vertical pressure vectors.

This assumption is confirmed by the admittance functions of lift and hinge moment coefficients of the vertical spectrum (Fig. 78). For a normalised frequency $f^* < 0.2$ the admittance functions are close to 1. Hence, vertical velocity fluctuations of frequencies corresponding to eddies five times bigger than the heliostat indeed directly impact lift and hinge moment. The angle of attack varies linearly with the instantaneous vertical velocity component while the longitudinal one is negligible (equation (5.2.31)). For smaller eddies the probability to enclose the heliostat completely reduces. Therefore, the value of the admittance functions decreases with increasing frequency.

The wind load coefficients depend mainly on the vertical velocity fluctuations. As a consequence, they collapse well on a continuous graph for varied vertical turbulence intensity I_w (Fig. 79) while they do not collapse well for varied longitudinal turbulence intensity (Fig. 80).

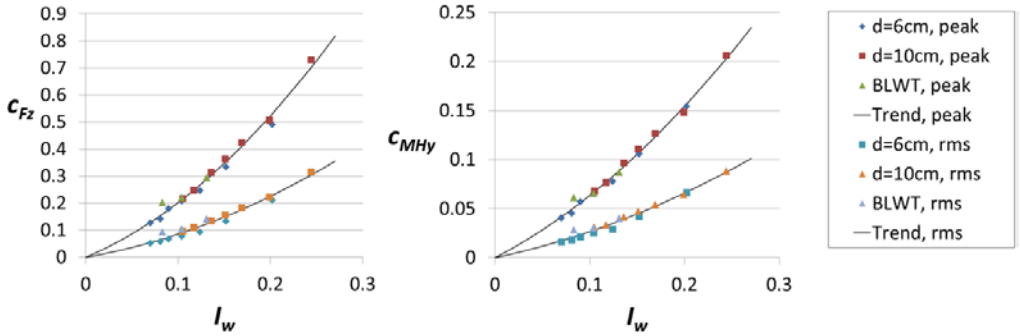

Fig. 79: Lift (left) and hinge moment (right) coefficients in stow position for T_0 = 3 s and varied I_w; upper graphs: peak values, lower graphs: rms values

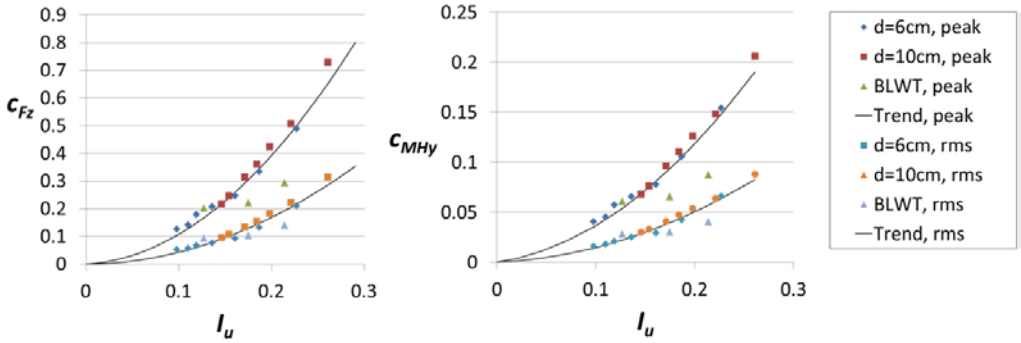

Fig. 80: Lift (left) and hinge moment (right) coefficients in stow position for T_0 = 3 s and varied I_u; upper graphs: peak values, lower graphs: rms values

The wind load coefficients collapse well on a continuous graph for varied I_w despite the shapes of the spectra and the values of the peak frequencies of the measurements are quite different (Fig. 72 to Fig. 74). Hence, it can be concluded that the wind load coefficients depend to a large extent only on I_w independently of the spectra mismatches (for the ratio I_w/I_u between 0.6 and 0.9 and for a shift of the peak frequencies within the range studied here).

5.2.3.2.2 Comparison of pressure distributions

The shape of the spectra has no impact on the wind load coefficients but on the pressure distributions. This becomes clear when spectra of same vertical turbulence intensity I_w (and therefore also same wind load coefficients) but different shapes are compared. For example, CYL4, CYL14 and BL2 are of

same vertical turbulence intensity I_w (Table 14). The vertical spectrum (green lower spectrum) of CYL4 (Fig. 73, middle) is more peaked than the one of CYL14 (Fig. 74, right) which is again more peaked than the one of BL2 (Fig. 72, right, solid middle green line). The BL2 vertical spectrum has the lowest peak value frequency and the lowest peak value which means that the eddies of peak energy are comparably big but contain low turbulence energy while the CYL4 spectrum has the smallest peak energy eddies (highest peak value frequency) but these contain highest turbulence energy. The small peak eddies of high energy of CYL 4 hitting the edge of the panel are causing high pressure/suction at the edge but cannot reach deeply into the panel (see Fig. 76, middle) while the bigger eddies of lower energy of BL2 cause a wider pressure/suction region but will cause less pressure/suction directly at the edge (Fig. 75, middle). The vertical spectrum and therefore also the pressure distribution of CYL 14 (Fig. 77, right) are in between those of BL2 and CYL4. The height and the width of the pressure/suction region at the edge seem to compensate each other regarding the wind load coefficients. That explains why the wind load coefficients are not sensitive to the shape of the spectra but depend mainly on I_w.

5.2.3.2.3 Statistical independence for T_0 < 10min

Usually, T_0 should be between 10 min and 1 h to account for the “spectral gap” (Van der Hoven, 1957) between wind events caused by large-scale meteorological changes and wind events caused by upwind obstacles/terrain roughness (Cook, 1985). For this reason, physical and statistical independence of the maximum annual mean wind speed (caused by large-scale meteorological effects) of the solar tower plant’s site and the peak wind load coefficients determined in BLWTs (modelling the upwind terrain roughness) is assumed which is a precondition of extreme value statistics of wind engineering for the determination of peak loads (Cook and Mayne, 1980). Hence, for T_0 = 3 s statistical independence is usually not given. An exception are lift and hinge moment coefficients for the stow position with horizontal panel. As shown, they depend mainly on the vertical velocity fluctuations (see section 5.2.3.2.1). The vertical velocity fluctuations of turbulence structures of one order of magnitude (or more) bigger than the panel (which corresponds in our case to $T_0 \approx 3$ s) are of small impact on the wind load coefficients (Fig. 71). In this regard, statistical independence of the wind load coefficients and the maximum 3-s-mean wind speed is given.

Furthermore, the smaller turbulence structures (with significant vertical velocity component) do not depend directly on the increase of longitudinal wind

velocity due to bigger eddies enclosing them. If the smaller structures would depend directly on bigger structures, the vertical spectrum should have a significant value for the peak frequency (of low value) of the longitudinal spectrum for T_0 = 1 h (or T_0 = 10 min respectively). However, this is not the case: S_{ww} is very low at the frequency of highest S_{uu} (Fig. 70).

Of course, the higher the turbulent energy of the low frequencies the higher is also the energy of the frequencies of relevant size. However, the energy of a big eddy is not decisive for the energy of smaller eddies (of relevant scale) which the big eddy encloses and transports. Decisive is the energy of former big eddies which had decomposed into these smaller eddies. Hence, during the 3 s period in which the maximum 3 s mean velocity occurs smaller eddies of all possible kind and different rotational speed may occur independently of the turbulence structure causing this wind event of maximum longitudinal velocity.

As a consequence, statistical independence of the wind load coefficients and the maximum 3-s-mean wind speed can be assumed and extreme value statistics can be applied.

5.2.3.2.4 Variation of I_w with heliostat size

The height of the panel in stow position H is approximately half the chord length of the panel h (for standard heliostats and PV trackers) plus the distance to the ground for upright orientation which is assumed to be 0.2 m in the present study. Table 15 gives the resulting panel heights and corresponding I_w (Fig. 81) for different panel sizes and a typical aspect ratio (width to height) of 1.2. The wind load coefficients are normalised by the panel area A (equations (5.2.27) and (5.2.28)) which could lead to the conclusion that they are independent of it. However, Table 15 and Fig. 81 respectively show how the turbulence intensity (which is decisive for lift and hinge moment, see Table 14 or Fig. 79) varies with height and therefore with the size of the heliostats. Hence, the heliostat size has to be taken into account for the determination of the peak wind loads in stow position. For example, the peak wind load coefficients for a heliostat of 8 m² (and I_w = 11.4%) are approximately 20% higher than for a heliostat of 120 m² (and I_w = 9.7%). Therefore, the wind load coefficients for stow position would have to be also normalised by I_w to be independent of the heliostat size.

Table 15: Panel height *H* and corresponding vertical turbulence intensities I_w for different panel sizes *A* of aspect ratio 1.2, mirror panel 0.2 m above ground and T_0 = 3 s (values in brackets extrapolated)

panel size *A* [m²]	8	16	32	64	120
panel height *H* [m]	1.5	2.0	2.8	3.9	5.2
vertical turbulence intensity I_w [%]	(11.4)	(10.9)	10.4	10.0	9.7

5.2.4 *Conclusions*

The objective of the investigations was to clarify the impact of scaling mismatches in turbulent energy spectra on the wind load coefficients.

By reducing the averaging time T_0 to a value corresponding to the size of the BLWT, the frequency shift of the spectra is avoided because only turbulence structures smaller than the BLWT have to be modelled. For the used BLWT with 2 m height an averaging time at full scale of $T_0 \approx 3$ s results. By filter functions corresponding to 3 s indeed good agreement of the full scale standard longitudinal spectra and the BLWT spectra could be achieved.

For the special case of the lift force and hinge moment coefficients of a flat plate in longitudinal turbulent flow and the given height, statistical independency of the maximum annual peak wind speed and the wind load coefficients can be assumed for $T_0 = 3$ s and extreme value statistics can be applied. The reason is that mainly the vertical velocity component is decisive for the loads and that the turbulent energy of small eddies with a significant vertical velocity component does not depend directly on eddies corresponding to $T_0 = 3$ s or larger.

For loads for which the longitudinal velocity fluctuations are decisive (especially drag of upright panel normal to wind direction), matching of the longitudinal spectrum is important. Then statistical independence is not given for an averaging time $T_0 < 10$ min and the method of reduced averaging time T_0 described by Banks (2011) may not be applied. It would be necessary to investigate whether the statistical dependency is of significant impact on the extreme peak values, for example by comparing the dispersion of full scale and BLWT measurements.

For the roughness elements applied in our experiments only matching either of the longitudinal or of the vertical turbulence intensity could be achieved. Furthermore, vertical spectra are still shifted somewhat towards smaller frequencies. The impact of these remaining differences between full scale standard spectra and BLWT spectra on lift and hinge moment coefficients were investigated by wind tunnel measurements with different ratios of the

vertical and longitudinal turbulence intensity I_w/I_u, different frequencies of the peak values, and spectra of different shapes. For all these measurements, the wind load coefficients collapse for varied I_w well on one continuous graph. By this and by analysing admittance functions it could be shown that the wind load coefficients depend mainly on the vertical turbulence intensity I_w and not on the longitudinal one I_u (at least for I_w/I_u between 0.6 and 0.9 and for a shift of the peak frequencies within the relevant range). Hence, for measurements of the peak wind load coefficients in stow position a match of I_w is decisive and sufficient. For the published wind tunnel measurements of heliostats usually I_w is matched. Hence, their results are valid although a significant shift of the longitudinal spectrum is given.

The dependency of the main loads in stow position mainly on I_w and not on the complete spectrum would allow a simpler modelling of the inflow just by vortex streets, for example generated by circular tubes as done in our experiments. However, for application of extreme value statistics (for the determination of the peak wind load coefficients (Cook and Mayne, 1980)) the dispersion of the wind load coefficients is needed and the mismatches of the spectra may have an impact on it.

Wind load coefficients for heliostats are usually normalised by the mirror area. This could lead to the conclusion that they are applicable to any heliostat size and that only the roughness length z_0 has to be considered. However, by the presented results of the BLWT tests it becomes clear that the increase in turbulence intensity for lower heliostat heights leads to significantly higher peak load coefficients for the stow position. Especially in recent years with a trend to smaller heliostats this is getting more important. Hence, for wind tunnel investigations of heliostats the turbulence intensity must correspond to both, to the heliostat size and to the roughness length z_0 of the surrounding of the heliostat field. For the stow position general validity of the wind load coefficients may could be reached by normalizing them, e.g. with I_w. This would have to be analysed in a separate study.

It can be concluded that wind tunnel tests of heliostats in stow position lead to realistic lift and hinge moment coefficients despite of mismatches in turbulent energy spectra (investigated in this study) as long as the vertical turbulence intensity at elevation axis height is matched. In principle, these results can be applied to any horizontal flat plate like structure of similar aspect ratio like for example (horizontal) canopy roofs. For high aspect ratios (like bridge decks) the vortices may not completely enclose the structure which could lead to different results.

5.2.5 *Annex: Definitions*

5.2.5.1 Boundary layer turbulent energy spectra

The spectral density function of the *u*-component (and similarly of the *w*-component) is defined by (Panofsky and Dutton, 1984, 3.7):

$$S_{uu}(\omega) = \frac{1}{\pi}\int_{-\infty}^{\infty} R_{uu}(\tau)e^{i\omega\tau}d\tau \text{ , } \omega = 2\pi f \qquad (5.2.10)$$

with the autocorrelation function

$$R_{uu}(\tau) = E\{u(t)u(t+\tau)\} = \frac{1}{2T}\int_{-T}^{T} u(t)u(t+\tau)dt \text{ for } T \to \infty \text{ .} \qquad (5.2.11)$$

S_{uu} is proportional to the square of the mean wind speed. Hence, for more general validity, the spectra is normalised by U_{mean}^2. Often S_{uu} is normalised by σ_u^2. However, then the impact of different turbulence intensities on the spectra cannot be investigated (Richards et al., 2007). A spectrum normalised by σ_u^2 can be transformed into a spectrum normalised by U_{mean}^2 by the square of the turbulence intensity as factor:

$$I_u^2 = \frac{\sigma_u^2}{U_{mean}^2} \text{ .} \qquad (5.2.12)$$

The mean wind speed at panel height *H* is used to define a normalised frequency for the turbulent energy spectra:

$$f^* = f\frac{h}{U_{mean}} \text{ .} \qquad (5.2.13)$$

Thereby, a normalised frequency of f^* = 1 represents eddies/wavelengths approximately of the size of the heliostat chord length *h* if Taylor hypothesis is assumed to be valid.

Formulas for the spectra of the atmospheric boundary layer are given by ESDU 85020, B4.1 to B4.4 or by Harris (1990) respectively. In combination with equations (5.2.12) and (5.2.13) the normalised turbulent energy is defined as follows:

$$\frac{f\cdot S_{uu}}{U_{mean}^2} = I_u^2\left(\beta_1\frac{2.987f^*\gamma_u}{[1+(2\pi f^*\gamma_u)^2]^{5/6}} + \beta_2\frac{1.294f^*\gamma_u}{[1+(\pi f^*\gamma_u)^2]^{5/6}}F_1\right) \qquad (5.2.14)$$

$$\frac{f\cdot S_{ww}}{U_{mean}^2} = \frac{\sigma_w^2}{U_{mean}^2}\left(\beta_1\frac{2.987[1+(8/3)(4\pi f^*\gamma_w)^2]f^*\gamma_w}{[1+(4\pi f^*\gamma_w)^2]^{11/6}} + \beta_2\frac{1.294f^*\gamma_w}{[1+(2\pi f^*\gamma_w)^2]^{5/6}}F_2\right) \qquad (5.2.15)$$

with

$$F_1 = 1 + 0.455e^{-0.76f^*\gamma_u\alpha^{1.8}} \quad (5.2.16)$$

$$F_2 = 1 + 2.88e^{-0.218f^*\gamma_w\alpha^{1.9}} \quad (5.2.17)$$

$$\gamma_u = \frac{L_u^x}{h\alpha} \quad (5.2.18)$$

$$\gamma_w = \frac{L_w^x}{h\alpha}\,. \quad (5.2.19)$$

Because *H* is very small compared to the gradient height it follows (ESDU 85020, B5):

$$\propto = 0.535 \quad (5.2.20)$$

$$\beta_1 = \beta_2 = 0.5\,. \quad (5.2.21)$$

5.2.5.2 Frequency filtering by averaging time T_0

The spectra depend on the time interval T_0 within which the spectra are measured. A finite T_0 filters frequencies with wavelengths longer than the wavelength corresponding to T_0. This filtering is described by (ESDU 83045, p. 27):

$$S_{ii}(f^*, T_0^*) = S_{ii}(f^*)\Psi(f^*, T_0^*) \quad \text{with} \quad (5.2.22)$$

$$\Psi(f^*, T_0^*) = 1 - \frac{\sin^2(\Pi f^* T_0^*)}{(\Pi f^* T_0^*)^2} \quad \text{and} \quad (5.2.23)$$

$$T_0^* = T_0\frac{U_{mean}}{h}\,. \quad (5.2.24)$$

To approximate the values of the lowest frequency that can be modelled in a wind tunnel the turbulence is assumed to be a superposition of circular eddies. The circular eddies are causing velocity fluctuations of frequencies that are approximated by

$$f_{D_{max}} \sim \frac{U_{mean}}{D_{max}} \quad (5.2.25)$$

The size of the circular eddies is restricted by the height of the boundary layer (Tennekes and Lumley, 1972, p. 12) which again is restricted by the BLWT height. The height restriction acts like a filter for eddies of this height/diameter or lager and for corresponding or lower frequencies respectively.

The effective filtering time is approximated by the time interval an eddy of diameter D_{max} needs to pass a certain point:

$$T_{filter} \sim T_{D_{max}} = \frac{1}{f_{D_{max}}} = \frac{D_{max}}{U_{mean}}\,. \quad (5.2.26)$$

The effective filtering time at full scale can be calculated by the corresponding maximum eddy diameter (D_{max} divided by the model scale) divided by the mean wind speed at elevation axis height H at full scale. Therefore, a mean wind speed must be defined to which the filtering time is related. In the present study, an hourly mean wind speed of 20m/s at 10 m height is assumed (according to the standard reference wind speed of ESDU 83045 and ESDU 85020). The mean speed at elevation axis height can be calculated regarding the vertical mean wind speed profile which depends on the surface roughness length of the surrounding terrain z_0 (ESDU 82026, equations (7.4) and (A1.10)).

5.2.5.3 Wind load coefficients

The force and moment coefficients are lower for the heliostat in stow position (horizontal mirror plane) than for the elevated positions because of the small area of wind attack. Nevertheless, the peak lift force F_z and the peak hinge moment M_{Hy} reach their highest values for stow conditions because of the high storm wind speed (typically about 42 m/s 3-s-peak value at 10 m height) compared to the maximum wind speed when heliostats stop operation and move into the horizontal safety stow position (typically about 18 m/s 3s-peak value at 10 m height). For horizontal flat plates in flows with little turbulence these wind loads would be almost zero. Mainly the turbulence of the flow leads to an instantaneous vertical velocity component which, in combination with flow separations at the leading edge, is causing the peak loads. Hence, the correct matching of the turbulence spectra is of importance for these wind load components. Their coefficients are defined by (Peterka et al., 1989):

$$F_z = c_{Fz} \frac{\rho}{2} U_{mean}^2 A \qquad (5.2.27)$$

$$M_{Hy} = c_{MHy} \frac{\rho}{2} U_{mean}^2 A h \ . \qquad (5.2.28)$$

5.2.5.4 Wind and turbulence intensity profiles

The mean wind speed and the turbulence intensity vary with height. For the wind speed the logarithmic vertical mean wind speed profile is assumed (Panofsky and Dutton, 1984, 6.2). The turbulence intensity reduces with height because of increased distance to the rough surface causing the turbulence. Fig. 81 shows the vertical turbulence intensity profile according to ESDU 85020 and ESDU 83045. For the investigations of horizontal panels matching of the wind speed and turbulence intensity mainly at panel height (= elevation axis height H) is decisive because of the small extent of the panel in vertical direction.

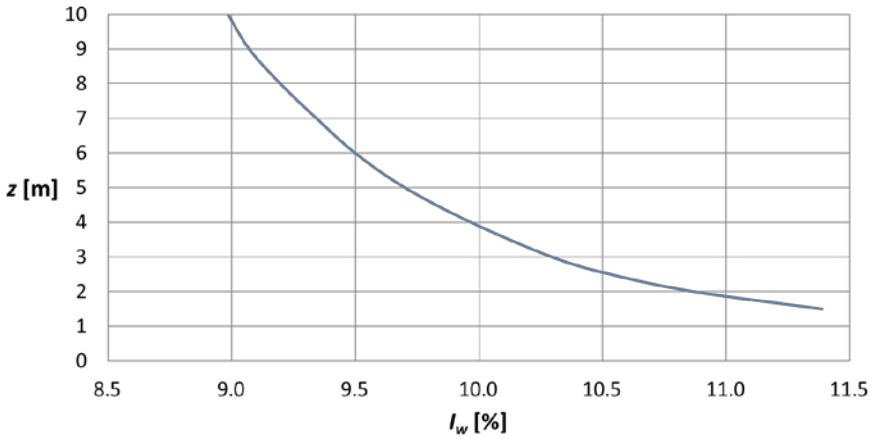

Fig. 81: Vertical turbulence intensity I_w profile (for T_0 = 3 s, z_0 = 3 cm and $U_{mean,10m}$ = 20 m/s) according to ESDU 85020 and ESDU 83045 (values below 3 m extrapolated)

5.2.5.5 Aerodynamic admittance

Following quasi-steady theory, both the lift and momentum coefficient of an arbitrary object (here: a plate) can be regarded as a linear function of the angle of attack φ (Rasmussen et al., 2010):

$$c_{Fz} = c_{Fz,\varphi=0} + \frac{\delta c_{Fz}}{\delta \varphi} \cdot \varphi \qquad (5.2.29)$$

$$c_{MHy} = c_{MHy,\varphi=0} + \frac{\delta c_{MHy}}{\delta \varphi} \cdot \varphi \; . \qquad (5.2.30)$$

For the stow position, the effective angle of wind attack corresponds to the instantaneous ratio of the vertical to the horizontal wind velocity (Fig. 82).

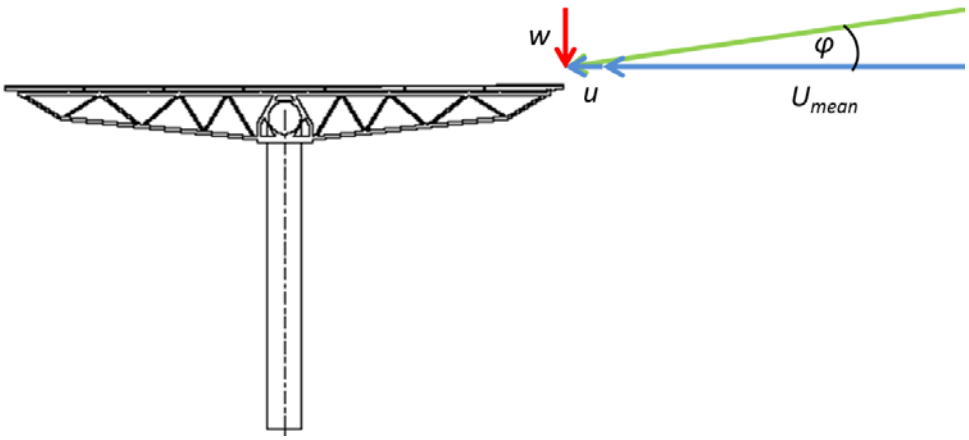

Fig. 82: Instantaneous angle of wind attack

Assuming generally small turbulence ($u \ll U_{mean}$), this leads to:

$$\varphi \cong \frac{w}{U_{mean}+u} \cong \frac{w}{U_{mean}} . \tag{5.2.31}$$

With $c_{Fz,\varphi=0} = 0$ and $c_{MHy,\varphi=0} = 0$ it follows:

$$c_{Fz} \cong \frac{\delta c_{Fz}}{\delta \varphi} \cdot \frac{w}{U_{mean}} \tag{5.2.32}$$

$$c_{MHy} \cong \frac{\delta c_{MHy}}{\delta \varphi} \cdot \frac{w}{U_{mean}} . \tag{5.2.33}$$

Equations (5.2.32) and (5.2.33) transformed into the spectral domain are:

$$S_{c_{Fz}c_{Fz}} \cong \left(\frac{\delta c_{Fz}}{\delta \varphi}\right)^2 \cdot \frac{S_{ww}}{U_{mean}^2} \cdot \chi_{Fz}^{w} \tag{5.2.34}$$

$$S_{c_{MHy}c_{MHy}} \cong \left(\frac{\delta c_{MHy}}{\delta \varphi}\right)^2 \cdot \frac{S_{ww}}{U_{mean}^2} \cdot \chi_{MHy}^{w} . \tag{5.2.35}$$

Thus, a linear relation is established between the force and moment spectra and the spectra of vertical velocity fluctuations. The frequency-dependent functions χ_{Fz}^{w} and χ_{MHy}^{w} are the so-called aerodynamic admittance functions. They represent the frequency-dependent impact of the vertical fluctuations on the wind load coefficients which cause a variation of the angle of attack. High frequencies representing small eddies which not enclose the complete heliostat will be of low impact. For larger eddies it is assumed that their vertical velocity component is decisive for the load coefficients. This assumption shall be confirmed by the determination of the admittance functions. For the low frequency end ($f \rightarrow 0$) the admittance functions are expected to be $\chi_{F,M}^{w} = 1$ if the assumption is valid.

Acknowledgements

The authors thank David Banks from CPP for the valuable discussions, Bert Blocken from Eindhoven University of Technology for his advices for improvement of the paper, and the Federal Ministry for Economic Affairs and Energy (BMWi) for its financial support of the investigations which were part of the project “AutoR” (code 0325629C).

5.3 Gust Duration

Partly reproduced from [Pfahl, A., Brucks, A., Holze, C., 2014. "Wind Load Reduction for Light-Weight Heliostats". Energy Procedia 49, 193-200].[6]

5.3.1 *Introduction*

It can be assumed that the fluctuations of the wind velocity are a superposition of eddies with different sizes and, hence, frequencies (Geurts, 1997). An eddy may be represented as a mass of fluid rotating around a centre (Appendix B.2). For high peak loads, eddies with a size in the order of magnitude of width and height of the heliostat are decisive. Eddies which are significantly smaller than the mirror panel have only local impact. Eddies significantly larger than the panel size have their high speed core regions above the heliostat. The rotational speed, and therefore the energy that can be transmitted, reduces strongly with the distance to the eddy's core (Cook, 1985, p. 20 et seqq.). Hence, the vertical velocity component at panel height of significantly larger eddies is lower which leads to lower hinge moments for horizontal panel compared to eddies of heliostat's size with higher vertical wind velocity component. Hence, the size of eddies causing the peak moment are of same order of magnitude as the chord length of the mirror panel which is about double the heliostat's height (Fig. 71).

With these assumptions it can be concluded that the duration of peak loads is limited to the duration an eddy of relevant size needs to pass the heliostat. In this study, the size of the eddy causing the peak hinge moment and its duration is determined. If short enough, the peak loads could be reduced by shock absorbers.

The dimensionless pressure coefficients c_p are lowest when the heliostat is in stow position (horizontal mirror panel). Nevertheless, most of the wind load components reach their highest values for stow conditions because of the high storm wind speed compared to operational wind speed. Therefore, in the present study, the stow position is studied in detail. (Only for the azimuth drive the wind loading during operation (moment about vertical axis) is decisive.)

Wind loads can be reduced by wind fences for high field densities (Peterka et al., 1986) (see section 4.1). The field density decreases with increasing distance from the tower because usually the heliostats are positioned in a staggered configuration to avoid optical blocking. For low field densities, the

[6] The full scale measurements were defined to a large extent and its results proofed and analysed by the main author. The preparation and execution of the measurements were performed by the co-authors.

benefits of wind fences regarding peak loads wear off from the third row on. Therefore, the maximum loads in a heliostat field are similar to the ones of an isolated heliostat, even if a wind fence is installed. Hence, the isolated heliostat without fence in stow position is the most relevant load case and is investigated in this study.

5.3.2 *Method*

The higher the resolution of a wind load measurement the higher are the peak values because also peaks of smaller duration but higher value will be detected. To determine the required resolution it is commonly assumed that only gusts larger than the structure are relevant because smaller gusts do not encompass the whole structure and are therefore only of local impact and cannot lead to the peak loading of the complete structure in the design relevant stow position. Often a value of 2-3 seconds is used (Peterka and Derickson, 1992, p. 5). However, this value might be appropriate for large buildings but not for small heliostats. For the investigated heliostat with a chord length of h = 2.5 m and for wind speeds of 10 m/s for example the duration of gusts that encompass the complete heliostat is only 2.5 m / 10 m/s = 0.25 seconds. Therefore, the high resolution (200 Hz) pressure measurements of this study were sufficient.

The full scale measurements were performed on an isolated heliostat set up (Fig. 83) in an “area with low vegetation such as grass and isolated obstacles (trees, buildings) with separations of at least 20 obstacle heights” (EN 1991-1-4, 2005, Appendix A) in the upwind main flow direction which complies with area category II.

Fig. 83: left: Heliostat (size 8m²) in the field, municipality Lilienthal, Germany. The chosen coordinate system according to Peterka is drawn on the facet. In the background: telescopic mast with sensors. Right: The heliostat is equipped with 84 differential pressure ports. (1) facet, (2) supporting structure, (3) elevation inclination, (4) pylon, (5) pedestal, (6) pressure tubing and instrumentation boxes, (7) pressure ports.

The heliostat and its test equipment were set up in Lower Saxony, municipality Lilienthal, at a countryside area almost without any houses, trees and bushes, or other objects that could disturb the wind (Lat 53°9'59.66 N, Long 8°50'0.40 E), see Fig. 84. Main wind direction is west.

Fig. 84: Location of full scale measurements (source: Google Maps)

For the performed full-scale tests the single isolated 8 m² (2.5 m x 3.2 m) heliostat was equipped with 84 differential pressure gauges (Fig. 83, right; Fig. 85) to collect time series of the differential pressure distribution of the panel. Strain gauges for the measurement of the hinge moment were not foreseen because measureable deformation of the pylon occurs only for rare high wind speeds.

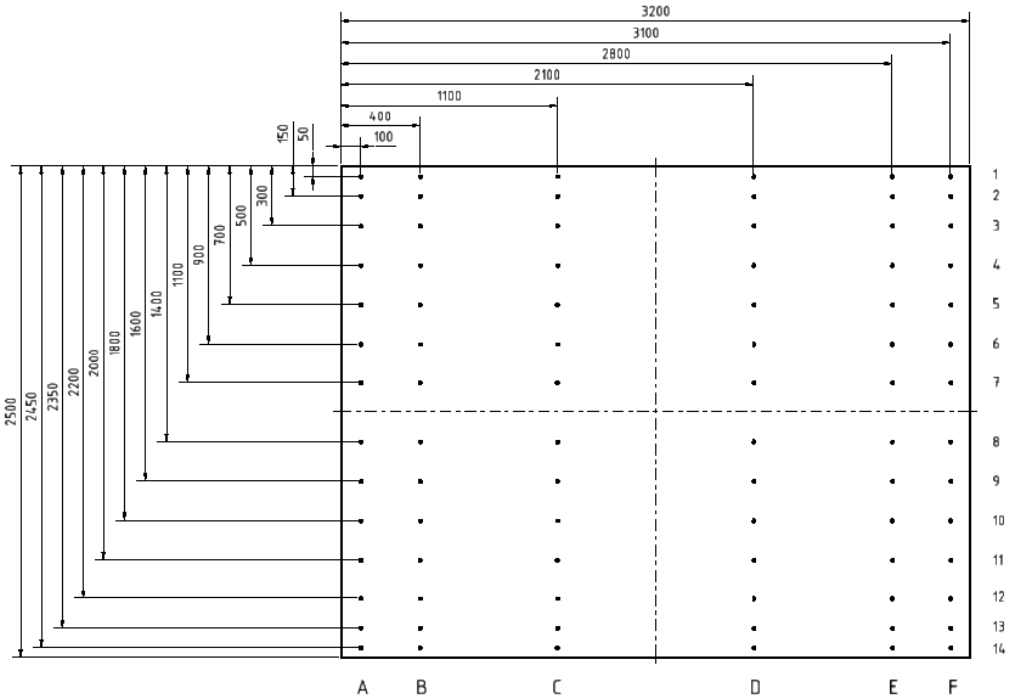

Fig. 85: Positions of pressure ports of full scale measurements, values in mm

The chosen coordinate system for azimuth and elevation follows (Peterka, 1988). The orientation of the coordinate system with respect to the heliostat and the geographic orientation are shown in Fig. 83, left. The heliostat facet (mirror surface) was facing the prevailing westerly winds with compass reading 308°. This angle was fixed during measurements.

The measurement procedure was as follows:

1. Calibration of pressure sensors
2. Start of data recording with a sample frequency of 200 Hz
3. Data acquisition for at least 83 s
4. Data storage on hard disk
5. Back to step 2 until 10 min are completed.

The measurement system consisted of: PC Pentium IV, 3.2 GHz, NI PCI 6255, 2 x 80 channels, 1.25 MS/s, 16-bit resolution; software: NI Labview 8.5; pressure sensors: Sensor Technics, HCLA series between +/- 2.5 mbar and +/-12.5 mbar; measurement tube length 5m, inner and outer diameter of tubes 1.2 mm and 2.7 mm respectively; wind direction sensor: Thies Clima 4.3150.00.161; wind low inertia cup anemometer: Thies Clima 4.3350.00.161.

5.3.3 *Results and Discussion*

With the pressure distribution the time dependent behaviour of the hinge moment coefficient c_{MHy} (moment about horizontal primary axis, definition according to Peterka and Derickson (1992)) for stow position was calculated as weighted summation of the point pressures following the method described by Hosoya et al. (2008). Fig. 86 shows the 10 s time interval at which the maximum peak value of a 10 min measurement occurred (at about t = 7 s). It seems that an eddy of Δt = 1.3 s duration (between 6.3 s and 7.6 s) caused the peak. The mean wind velocity at this time interval was U_{mean} = 5.5 m/s. This leads to an eddy size of $D = U_{mean} * \Delta t$ = 5.5 m/s * 1.3 s = 7.2 m which is of same order of magnitude as the chord length of h = 2.5 m as assumed (three times bigger) and of the integral length scale $L^x_u \approx$ 3 m for z_0 = 0.015 (open country (Peterka, 1992)) and for a height of $z = H$ = 2 m (extrapolated from (ESDU 85020, 1985), Figure 3a). For storm conditions with for example U_{peak} = 40 m/s peak wind speed and U_{mean} = 25 m/s mean wind speed at z =10 m height and resulting U_{mean} = 19.6 m/s mean wind speed at z = 2 m height (equation (3.1.1)) a gust duration of $\Delta t = D / U_{mean}$ = 7.2 m / 19.6 m/s = 0.37 s results. Only about half of this time the gust leads to higher hinge moment (compared to the mean hinge moment). Hence, the duration of the peak hinge moment would be in the range of Δt = 0.2 s.

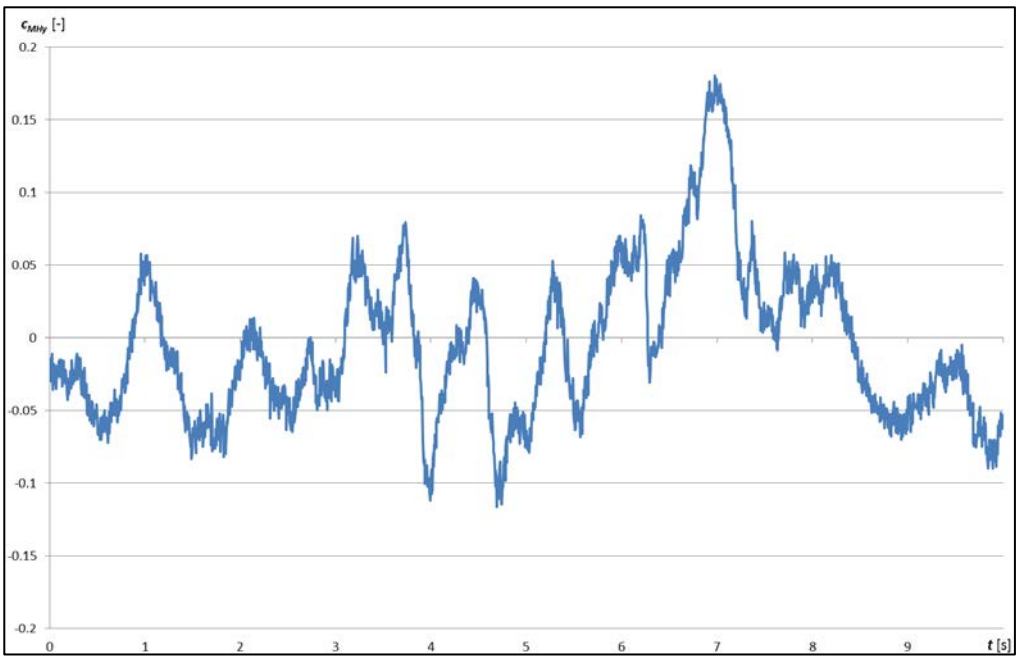

Fig. 86. Hinge moment coefficient over time, elevation 0° (stow position)

Table 16 shows the pressure coefficient distribution at the moment in time of maximum hinge moment coefficient (t = 6.995 s). Wind direction was β = 47°.

Table 16: pressure coefficient distribution at the moment in time of maximum hinge moment coefficient

	A	B	C	D	E	F
1	5.5	4.9	2.7	4.1	3.1	1.7
2	2.1	3.4	3.0	3.1	2.4	1.7
3	2.0	0.1	2.3	2.3	1.7	1.1
4	3.0	0.8	1.4	0.4	0.1	0.1
5	3.7	1.0	0.5	-0.6	0.6	0.3
6	2.0	0.9	0.4	0.5	0.7	0.3
7	1.8	0.3	0.4	0.7	0.6	0.3
8	1.8	0.7	0.7	0.6	0.4	0.1
9	1.4	0.4	0.7	0.5	0.3	0.5
10	0.6	0.7	0.0	0.4	0.3	0.4
11	1.0	0.4	0.4	0.3	0.5	0.2
12	1.0	0.3	0.6	0.2	-0.1	0.4
13	0.6	0.0	0.3	0.1	0.2	0.0
14	0.5	0.0	0.2	0.1	0.4	0.4

The pressure coefficient distribution of Table 16 leads to a hinge moment coefficient c_{MHy} = 0.18 and to a lift coefficient c_{Fz} = 1.0 which is in the same range as the values given by Peterka and Derickson (1992) for wind direction β=0° which confirms the measurements.

5.3.4 *Conclusions*

The diameter of the eddy causing the peak hinge moment of a 10 min full scale measurement could be determined. It is about double as big as the chord length. This confirms the assumption that gusts of a duration corresponding to a size of same order of magnitude as the chord length lead to the peak hinge moments. Hence, the peak hinge moment is not of arbitrary duration but limited. For the sample case of an 8 m² heliostat the duration at storm is in the range of 0.2 s. For such short duration it seems to be feasible to use shock absorbers to reduce the peak loads significantly. This may help to reduce the cost of facets, bearings, locking devices, pylon, and foundation.

6 Summary and Outlook

General

For the structural dimensioning of heliostats, wind loading and deformation due to gravity are decisive which lead to the following three dimensioning criteria:

1. Tracking accuracy: It is mainly defined by backlash of the drives. If the wind loads caused by turbulence overcome the breakaway torque the mirror panel fluctuates which cannot be compensated by the control and a tracking error results.
2. Optical accuracy: Deformations during operation are mainly caused by gravity. The impact of the wind on the optical accuracy is usually negligible which is a new finding that simplifies the design process significantly.
3. Durability: The heliostat must resist the wind loads during operation and in stow position during storms. For this, the wind load coefficients must be known as precisely as possible to enable a cost effective dimensioning.

Methods to determine the tracking and the optical accuracy with a high precession are already developed. Therefore, in the thesis the third point is further investigated. The investigations are divided into four main influencing factors: heliostat design, general heliostat properties, position within heliostat field, and boundary layer wind properties.

Impact of wind loads on heliostat design

Several approaches aim to reduce the wind loads: By encasing the heliostat the wind loads could be eliminated completely. However, this is costly and leads to additional losses. Regarding the vertical mean wind speed profile, the wind loads are low close to the ground. Hence, the panels can be lowered for stow position to reduce the maximum wind loads. Therefore, a new patented heliostat concept was developed with the possibility to stow the mirror panel close to the ground by which cost reductions of up to 25% can be achieved. Furthermore, it is possible to reduce the loads on the drives by rims in combination with a locking device for stow position. A new kind of rim drive heliostat was developed and was selected for a small solar tower demonstration plant which is under construction.

Impact of general heliostat properties on wind loads

The impact of two heliostat properties on the wind loads was investigated: The aspect ratio of the panel and the width between panels, which are both

fundamental for the heliostat design. The dependencies of the different wind load components on the aspect ratio were determined for the first time and formulas to calculate these dependencies are given. By measured pressure distributions on the panel explanations were found for the aspect ratio dependencies. In literature it was stated that up to a portion of 15% of openings the mirror panel can be treated as a solid surface area. However, for a wide gap between two mirror panels an increase of the hinge moment of 20% was measured (for both: operational mode and in stow position) and an explanation for this increase was found.

Wind loads within heliostat field

Economically, it is an important question whether a wind fence should be used to protect a heliostat field. BLWT measurements showed that for high field densities (near the central tower) the wind loads can be reduced significantly by wind fences while for low field densities (typical for regions far from the tower) the impact is small. Hence, wind fences seem not worthwhile for identical heliostats for the complete field which is usually the case. Similar results had been obtained before for heliostats in operation but not for the stow position which is the design relevant case. For some locations within a heliostat field higher drag and lift forces compared to an isolated heliostat are mentioned in literature but no reason for it is given. By BLWT measurements it was found that an increase at the windward corners of the field occurs where the wind speed is increased when the flow passes around the field.

Impact of wind properties on heliostat wind loads

It was validated for the first time that usual BLWT investigations lead to realistic results although the high Reynolds numbers of storms cannot be reached. Therefore, wind tunnel measurements with high Reynolds numbers in a high pressure wind tunnel were performed for a heliostat in stow position. Bending of the model could not be avoided because of the extremely high loads at the high Reynolds numbers. However, the impact of the bending on the wind loads could be determined and it could be concluded that the increase of the wind load coefficient with increasing wind speed was caused only by the deformation of the heliostat model and not by the increased wind speed. Hence, the wind loads are not Reynolds number dependent.

The longitudinal turbulent energy spectrum of BLWT is shifted towards higher frequencies because eddies bigger than the wind tunnel dimensions cannot be simulated. This problem is relevant especially for large model scales that are required for heliostat investigations. The problem can be solved by reducing the averaging time to 3 s. Then bigger eddies are still not captured by the wind tunnel but by the maximum wind speed that has to be considered for the

calculations of the maximum wind loads. It is shown that also for such a short averaging time statistical independence of maximum wind speed and wind load coefficients can be assumed which is a precondition of the extreme value statistics for the determination of the peak wind load coefficients. This independency results from the fact that the wind load coefficients depend to a large extent on the vertical turbulence intensity and not on the longitudinal turbulence intensity. Also the shape of the spectra is of small impact. For the published wind tunnel measurements of heliostats usually the vertical turbulence intensity is matched. Hence, their results are valid although a significant shift of the longitudinal spectrum is given which was validated for the first time. By the presented results of the BLWT tests it became also clear that the increase of the turbulence intensity for lower heliostat heights (due to the turbulence intensity profile) leads to significantly higher peak load coefficients for stow position.

The vertical velocity component of an eddy at heliostat panel's height depends on the size of the eddy. With increasing eddy size its vertical component near the ground reduces. Hence, the size of eddies that may cause the peak loads is limited and therefore also the duration of the peak loads which was verified for the first time by full scale measurements. Due to the limited duration it is possible to reduce the peak loads by shock absorbers which will be investigated by the project MAHWIN (0324213B) based on these findings and financed by the Federal Ministry for Economic Affairs and Energy (BMWi).

The presented investigations do not include dynamic effects. Furthermore, it was not investigated whether the remaining spectra mismatches of the turbulent energy spectra in BLWT tunnels are of impact on the dispersion which is needed for the extreme value statistics of the peak loads. This will be investigated by the project MAHWIN as well. Furthermore, full scale measurements should be performed for further validation of the BLWT measurements of isolated heliostats and of heliostats within a field.

In the appendix, a new figurative explanation of the theory of extreme value statistics for the determination of the wind load peak values and the correlation between eddy diameters and turbulent energy spectra is given. It may help especially readers from the solar energy community to whom these fundamental theories of wind engineering might be new to understand them.

Acknowledgments

The measurements in the high pressure wind tunnel were performed by Heiko Uhlemann (DNW German Dutch Wind Tunnels) and the team of the HDG Göttingen. Many thanks for their persistent work till all problems with the extraordinary high loads that occurred at the high Reynolds numbers could be solved. All other wind tunnel investigations were performed by Michael Buselmeier and Martin Zaschke and their colleagues (Wacker Engineers). I am grateful for their excellent work and for many valuable discussions with them and with Professor Jürgen Wacker who furthermore helped me to find the right supervisor for the thesis.

The daily supervisor Dr Chris Geurts insisted that the thesis contains new findings not only for the solar energy community but also regarding fluid mechanics in general. Although it increased the duration of the thesis I am grateful for leading the work thus to more fundamental research. I thank Professor Bert Blocken very much for becoming the first supervisor of the dissertation and for his encouragement and excellent advices.

I thank Professor Hans Müller-Steinhagen who supervised the work at the beginning. Professor Robert Pitz-Paal, the second supervisor, always supported the idea of investigating wind loads on solar collectors although this was a completely new field for our institute. I thank him for his patience but also for urging me finally to complete the thesis. I thank my supervisor and head of our department Dr Reiner Buck for his open mind regarding new promising ideas and regarding the employment also of people with somewhat unusual CV. I thank him as well for his sharp-witted comments on new ideas which were important to reconsider thinks more deeply and to find promising concepts and for enabling me to work on heliostats which was also a new field for our institute. Thanks also to my colleagues Stefano Giuliano for leading our group and Dr Felipe Vasquez who worked together with me on wind loads, he especially on dynamic effects.

We had many valuable discussions with Dr Carsten Holze from ToughTrough. I thank him and his team, especially for the full scale measurements. The presentation of Dr David Banks (CPP Wind Engineering Consultants) at the ICWE13 and discussions with him was decisive for starting investigations about spectra which are the core of the thesis. Thanks also to Dr Bo Gong (The Key Laboratory of Solar Thermal Energy and Photovoltaic System, IEE-CAS) for interesting exchanges on our works.

The investigations became only possible with the financial support of the German Federal Ministry for the Environment, Nature Conservation and

Nuclear Safety (BMU) (projects HELIKO (16UM0081), HELIANT (03UM0067) and HydroHelio (0325123B)), the Federal Ministry for Economic Affairs and Energy (BMWi) (HelFer (0325458A) and AutoR (0325629A-C)), the DLR division ‘‘Energy’’ (high pressure wind tunnel measurements) and the DLR Technology Marketing (KOSMOS).

I am grateful to my teachers at school and university, especially Mrs Röll from primary school and Mr Johann from secondary school. Partly responsible for the thesis are also my classmates from upper school by calling me “The Doctor”. I am deeply grateful to my parents and to Gino, to my grandparents and to my brother and sister. I thank especially my wife Christiane and our daughters Elisabeth, Johanna, Luise, Maria and Susanne. They all sustained it when I was more than others physically and sometimes also mentally not at home because of the thesis. There are many which are often forgotten but which are very important that such a work can be written like Mrs Ibrahim and her team from the cantina and the cleaning stuff – and mainly Jesus.

References

Ahlborn, B., Lefrancois, M., King, H.D., 1998. “The Clockwork of Vortex Shedding”. Phys. Essays 11, 144–154.

Ahlborn, B., Seto, M.L., Noack, B.R., 2002. “On Drag, Strouhal Number and Vortex-Street Structure”. Fluid Dynamics Research 30, 379-399.

Aly, A.M., 2016. “On the evaluation of wind loads on solar panels: The scale issue”. Solar Energy 135, 423-434.

Aly, A. M., Bitsuamlak, G., 2013. “Aerodynamics of Ground-Mounted Solar Panels: Test Model Scale Effects”. Journal of Wind Engineering and Industrial Aerodynamics 121, 250-260.

Antonia, R.A., Zhou, Y., Matsumura, M., 1993. Spectral Characteristics of Momentum and Heat Transfer in the Turbulent Wake of a Circular Cylinder. Experimental Thermal and Fluid Science 6, 371-375.

Arya, S. P., 1982, Atmospheric Boundary Layers Over Homogenous Terrain, in: Plate, E. J., ed., 1982. Engineering Meteorology, Studies in Wind Engineering and Industrial Aerodynamics, Vol. 1, Elsevier, Amsterdam - Oxford - New York.

Banks, D., 2013. “Measuring Peak Wind Loads on Solar Power Assemblies”. Proc. ICWE13, Amsterdam.

Basu, R.I., Vickery, B.J., 1983. “Across-Wind Vibrations of Structure of Circular Cross-Section. Part II. Development of a Mathematical Model for Full-Scale Application”. Journal of Wind Engineering and Industrial Aerodynamics, 12, 75-97.

Berenguel, M., Rubio, F.R., Valverde, A., Lara, P.J., Arahal, M.R., Camacho, E.F., López, M., 2004, “An Artificial Vision-Based Control System for Automatic Heliostat Positioning Offset Correction in a Central Receiver Solar Power Plant”, Solar Energy 76, pp. 563-575.

Blocken, B., 2014. “50 Years of Computational Wind Engineering: Past, Present and Future”, Journal of Wind Engineering and Industrial Aerodynamics 129, 69-102.

Brightsource Energy, 2011. www.brightsourceenergy.com/media_room.

Brightsource Energy, 2012, http://www.brightsourceenergy.com/image-downloads, accessed June 28, 2012.

Cheung, J.C.K., Melbourne, W.H., 2005. “Spanwise Deck Sectional Force Correlation of Bridge in Motion in Turbulent Flow”. Proceedings of the Sixth Asia-Pacific Conference on Wind Engineering, Seoul, Korea, 150-157.

Clean Technica, March 2017. “SolarReserve Bids 24-Hour Solar At 6.3 Cents In Chile”, https://cleantechnica.com/2017/03/13/solarreserve-bids-24-hour-solar-6-3-cents-chile/, accessed April 6, 2018.

Cook, N.J., Mayne, J.R., 1979, “A Novel Working Approach to the Assessment of Wind Loads for Equivalent Static Design”, Journal of Wind Engineering and Industrial Aerodynamics, 4, 149-164.

Cook, N.J., Mayne, J.R., 1980, “A Refined Working Approach to the Assessment of Wind Loads for Equivalent Static Design”, Journal of Wind Engineering and Industrial Aerodynamics, 6, 125-137.

Cook, N.J., 1985, “The Designer’s Guide to Wind Loading of Building Structures – Part 1: Background, Damage Survey, Wind Data and Structural Classification”, Butterworths, London.

Cook, N.J., 1990, “The Designer’s Guide to Wind Loading of Building Structures – Part 2: Static Structures”, Butterworths, London.

CSP today, 2013, “CSP Today Industrial Applications Guide: Desalination and Enhanced Oil Recovery”, http://csptoday.com/csp/pdf/CSP-Desalination0813_Sevilla_EN.pdf, accessed February 28, 2015.

Davenport, A.G., 1967, “The Dependence of Wind Loads on Meteorological Parameters”, Proceedings International Conference on Wind Effects on Buildings and Structures, Ottawa, Vol 1, pp 19-82.

Deflandre, J., Matarasso, P., and Traisnel, J.-P., 1978, “Heliostats,” U.S. Patent No. US4129360.

DIN 1055-4, 2005, German standard. “Action on Structures – Part 4: Wind Loads”, Berlin.

Durst, C.S., 1960. “Wind Speeds Over Short Periods of Time”. The Meteorological Magazine 89, pp. 181-186.

Dyrbye, C., Hansen, S.O., 1997. “Wind Loads on Structures”. Wiley & Sons, Chichester, England, p. 186.

Emes, M.J., Arjomandi, M., Nathan, G.J., 2015, “Effect of heliostat Design Wind Speed on the Levelised Cost of Electricity from Concentrating Solar Thermal Power Tower Plants”, Solar Energy 115, 441-451.

ESDU 82026, 1993. “Strong Winds in the Atmospheric Boundary Layer, Part I: Mean-Hourly Wind Speeds”. London, England.

ESDU 83045, 2002, “Strong Winds in the Atmospheric Boundary Layer Part 2: Discrete Gust Speeds”. London, England.

ESDU 85020, 1985. “Characteristics of Atmospheric Turbulence Near the Ground, Part II: Single Point Data for Strong Winds (Neutral Atmosphere)”. London, England.

ESDU 89050, 1990. “Boundary Walls, Fences and Boardings: Mean and Peak Wind Loads and Overturning Moments”. Engineering Science Data, Wind Engineering Series, 2b, London.

EN 1991-1-4, 2005, “Eurocode 1: Actions on Structures – Part 1-4: General Actions - Wind Actions”, Technical Committee CEN/TC250 Structural Eurocodes.

Fage, A.., Warsap, J.H., 1929. “The Effects of Turbulence and Surface Roughness on the Drag of a Circular Cylinder”. British Aeronautical Research Concil, Rept1179, 248-255, London.

Fisher, R.A., Tippett, L.H.C., 1928, “The Frequency Distribution of the Largest or Smallest Member of a Sample”, Proceedings of the Cambridge Philosophical Society, 24, 180-190.

Försching, H.W., Melzer, E., Schewe, G., 1981. “Ein neuer Windkanal für gebäudeaerodynamische und aeroelastische Untersuchungen bei Reynoldszahlen bis 10^7“, Konstruktiver Ingenieurbau Berichte, 35/36, 127-133.

Fröhlich, J., 2006[1]. “Large Eddy Simulation turbulenter Strömungen“, Teubner, Wiesbaden.

Gary, J., Turchi, C., Sieger, N., 2011, “CSP and the DOE Sunshot Initiative”, Proc. SolarPACES 2011 conference, Granada.

Geurts, C., 1997. “Wind-Induced Pressure Fluctuations on Building Facades“, Dissertation, Eindhoven.

Geurts, C., Blackmore, P., 2013. “Wind Loads on Stand-off Photovoltaic Systems on Pitched Roofs”, Journal of Wind Engineering and Industrial Aerodynamics 123, 239-249.

GlassPoint Solar Inc., http://www.glasspoint.com/, accessed February 28, 2015.

Gomes, L., Vickery, B.J., 1977. “On the Prediction of Extreme Wind Speeds from the Parent Distribution”, Journal of Wind Engineering and Industrial Aerodynamics, 2, 21-36.

Gonzáles, R.S., Flamant, G., 2014, “Technical and Economic Feasibility Analysis of Using Concentrated Solar Thermal Technology in the Cement Production Process: Hybrid Approach—A Case Study”, Journal of Solar Energy Engineering 136.

Gong, B., Li, Z., Wang, Z., Wang, Y., 2012, “Wind Induced Dynamic Response of Heliostat”, Renewable Energy, 38 (1), pp. 206-213.

Gong, B., Wang, Z., Li, Z., Zang, C., Wu, Z., 2013, “Fluctuating Wind Pressure Characteristics of Heliostats”, Renewable Energy, 50, pp. 307-316.

Gumbel, E.J., 1958, “Statistics of Extremes”, Columbia University Press, New York.

Hosoya, N., Peterka, J.A., Gee, R.C., Kearney, D., 2008. “Wind Tunnel Test of Parabolic Trough Solar Collectors”, NREL Subcontract Report NREL/SR-550-32282, Golden, Colorado.

Hucho, W.H., 2002. “Aerodynamik der stumpfen Körper“, Braunschweig/Wiesbaden.

Huss, S., Traeger, Y.D., Shvets, Z., Rojansky, M., 2011, “Evaluating Effects of Wind Loads in Heliostat Design”, Procedings SolarPACES 2011 conference, Granada.

INP-ENSEEIHT, 2015,
http://hmf.enseeiht.fr/travaux/CD0506/mci/reports/avb1/marl.htm, accessed March 7, 2015.

Isyumov, N. (Ed.), 1999. “Wind Tunnel Studies of Buildings and Structures”. ASCE Manuals and Reports on Engineering Practice No. 67, Virginia.

Jensen, M., 1958, The Model Law for Phenomena in Natural Wind, Ingeniøren, International Edition 2, 121–128, Denmark.

Jubayer, C.M., Hangan, H., 2016. „A Numerical Approach to the Investigation of Wind Loading on an Array of Ground Mounted Solar Photovoltaic (PV) Panels”, Journal of Wind Engineering and Industrial Aerodynamics 153, 60-70.

Von Kármán, T., Rubach, H., 1912. “Ueber den Mechanismus des Fluessigkeits- und Luftwiderstandes“. Phys. Z. XIII, 49–59.

Kolb, G.J., Jones, S.A., Donnelly, M.W., Gorman, D., Thomas, R., Davenport, R., R. Lumia, 2007, “Heliostat Cost Reduction Study”, SANDIA Report SAND2007-3293.

Leder, A., Geropp, D., 1993. “Analysis of Unsteady Flow Past Bluff Bodies”. Journal of Wind Engineering and industrial aerodynamics, 49, 329-338.

Letchford, C.W., Holmes, J.D., 1994. “Wind Loads on Free Standing Walls in Turbulent Boundary Layers”. Journal of Wind Engineering and Industrial Aerodynamics, 51, 1-27.

Liedke, P, Lewandowski, A., Pfahl, A., Hölle, E., “Precise Low Cost Chain Gears for Heliostats”, Procedings SolarPaces 2015 conference, Cape Town.

Liedke, P., Pfahl, A., Vásquez-Arango, J.F., Hölle, E., 2017. “3rd Generation Rim Drive Heliostat with Monolithic Sandwich Panel”, SolarPACES 2017 conference, abstract submitted.

Mancini, T. R., 2000, “Catalog of Solar Heliostats”, SolarPACES Technical Report No. III-1/00.

Mathey, F, Cokljat, D., Bertoglio, J.P., Sergent, E., 2006. “Assessment of the vortex method for Large Eddy Simulation inlet conditions”. Progress in Computational Fluid Dynamics, 6, 58-67.

Mayne, J.R., Cook, N.J., 1978, “On Design Procedures for Wind Loading”, Building Research Establishment, Current Paper, CP25/78.

NBE-AE/88, 1988. Spanish standard. “Acciones en la edificación”.

Neelamani, S., and Al-Awadi, L., 2011, “Extreme Winds in Kuwait Including the Effect of Climate Change”, Fundamental and Advanced Topics in Wind Power, Dr. Rupp Carriveau (Ed.), ISBN: 978-953-307-508-2, InTech, DOI: 10.5772/18447. Available from: http://www.intechopen.com/books/fundamental-and-advanced-topics-in-wind-power/energy-dissipation-minimization-in-superconducting-circuits1, accessed March 22, 2015.

NIST, National Institute of Standards and Technology, http://www.itl.nist.gov/div898/winds/nondirectional.htm, values of Albuquerque NM, accessed March 22, 2015.

Padmanathan, P., head of ACWA Power, http://reneweconomy.com.au/2015/saudi-power-giant-sees-solar-taking-on-base-load-fossil-fuels-57218, accessed February 28, 2015.

Panofsky, H.A., J.A. Dutton, 1984. “Atmospheric Turbulence – Models and Methods for Engineering Applications”. John Wiley and Sons, New York.

Pérez-Rábago, C., González-Aguilar, J., Prakash, R., Sachan, S., Goel, N., and Romero, M., 2012, “Development and Optical Characterization of a Heliostat to be Used in Thermosolar Electric Stations in India,” SolarPACES 2012 Conference, Marrakesh, Morocco, September 11–14.

Peterka, J.A., Hosoya, N., Bienkiewicz, B., Cermak, J.E., 1986, “Wind Load Reduction for Heliostats”, Report SERI/STR-253-2859, Solar Energy Research Institut, Golden, Colorado.

Peterka, J. A., Tan, Z., Bienkiewicz, B., Cermak,J. E., 1988. “Wind Loads on Heliostats and Parabolic Dish Collectors”,SERI/STR-253-3431.

Peterka, J.A., Tan, Z., Cermak, J.E., Bienkiewicz, B., 1989. “Mean and Peak Wind Loads on Heliostats”. Journal of Solar Energy Engineering, 111, 158-164.

Peterka, J.A., Derickson R.G., 1992. “Wind Load Design Methods for Ground Based Heliostats and Parabolic Dish Collectors”. Report SAND92-7009, Sandia National Laboratories, Springfield.

Pfahl, A., Buck, R., and Rehschuh, K., 2008, “Method for Controlling the Orientation of a Heliostat on a Receiver, Heliostat Apparatus and Solar Power Plant”, International Patent WO2008/058866A1.

Pfahl, A., 2011. “Schwenkvorrichtung und Heliostat“, German Patent Application 102011056341.

Pfahl, A., Buselmeier, M., Zaschke, M, 2011a. “Wind Loads on Heliostats and Photovoltaic Trackers of Various Aspect Ratios”. Solar Energy 85, 2185-2201.

Pfahl, A., Buselmeier, M., Zaschke, M., 2011b. “Determination of Wind Loads on Heliostats”. Proc. SolarPACES 2011 conference, Granada.

Pfahl, A., Uhlemann, H., 2011. “Wind Loads on Heliostats and Photovoltaic Trackers at Various Reynolds Numbers”. Journal of Wind Engineering and Industrial Aerodynamics 99, 964-968.

Pfahl, A., Randt, M., Holze, C., Unterschütz, S., 2013, “Autonomous Light-Weight Heliostat With Rim Drives,” Solar Energy, 92, pp 230–240.

Pfahl, A., 2014, “Survey of Heliostat Concepts for Cost Reduction”, Solar Energy Engineering 136.

Pfahl, A., Brucks, A., Holze, C., 2014. “Wind Load Reduction for Light-Weight Heliostats”, Energy Procedia 49, 193-200.

Pfahl, A., Randt, M., Meier, F., Zaschke, M., Geurts, C.P.W., Buselmeier, M., 2015a. “A Holistic Approach for low Cost Heliostat Fields”. Energy Procedia.

Pfahl, A., Buck, R., Gross, F., Liedke, P., 2015b. „Solarvorrichtung“, German Patent Application 20 2015 103 236.6, 2015061818581600DE.

Pfahl, A., Buck, R., Gross, F., 2016. „Solarvorrichtung, Verfahren zur Herstellung eines Formteils und Verfahren zur Herstellung eines Formgebungselements“, German patent application 102016210569.8.

Pfahl, A., Coventry, J., Röger, M., Wolfertstetter, F., Vasquez, F., Gross, F., Arjomandi, M., Schwarzbözl, P., Geiger, M., Liedke, P., 2017a. “Progress in Heliostat Development”. Solar Energy (152), 3-37.

Pfahl, A., Gross, F., Liedke, P., Hertel, J., Rheinländer, J., Mehta, S., Vásquez-Arango, J.F., Giuliano, S., Buck, R., 2017b. “Reduced to Minimum Cost: Lay-Down Heliostat with Monolithic Mirror-Panel and Closed Loop Control”. SolarPACES 2017 conference.

Pfahl, A., Zaschke, M., Geurts, C.P.W., Buselmeier, M., 2018. “Impact of Turbulent Energy Spectra Characteristics on Wind Loading of Heliostats and PV Trackers in Stow”. Journal of Wind Engineering and Industrial Aerodynamics, under review.

Plate, E.J., 1982. “Wind Tunnel Modelling of Wind Effects in Engineering”, in: Plate, E.J. (Ed.), Engineering Meteorology, Studies in Wind Engineering and Industrial Aerodynamics, 1, Elsevier, Amsterdam – Oxford – New York, pp. 573-639.

Rebolo, R., Lata, J., Vázquez, J., 2011. “Design of Heliostats Under Extreme and Fatigue Wind Loads”, In: Proceedings SolarPACES 2011, Granada.

Reina, G.P., De Stefano, G., 2017. “Computational Evaluation of Wind Loads on Sun-Tracking Ground-Mounted Photovoltaic Panel Arrays”, Journal of Wind Engineering and Industrial Aerodynamics 170, 283-293.

Ricklin, P., Slack, M., Rogers, D., Huibregtse, R., 2014. “Commercial Readiness of eSolar Next Generation Heliostat”, Energy Procedia 49.

Ries, A., 2017. Linearantrieb mit einer Spindel, German patent application 10 2017 001 550.3.

Roshko, A., 1992. “Instability and Turbulence in Shear Flows”. In: Bodner, S.R., Singer, J., Solan, Z., Hashin, Z., “Theoretical and Applied Mechanics“,

Proceedings of the XVIIIth International Congress of Theoretical and Applied Mechanics, Haifa, Israel.

Sakamoto, H., Arie, M., 1983. “Flow Around a Normal Plate of Finite Width Immersed in a Turbulent Boundary Layer”. Trans ASME, Journal of Fluids Engineering, 105, 98-104.

Sankrithi, M., 2012, “Low-Cost Heliostatic Mirror With Protective Inflation Stabilizable Surface Element Means,” U.S. Patent No. 8127760B2.

Sayre, R.K., 1980, “Heliostat Assemblies”, US Patent US4209231A.

Schewe, G., 1983. “On the Force Fluctuations Acting on a Circular Cylinder in Crossflow from Subcritical up to Transcritical Reynolds numbers”. Journal of Fluid Mechanics, 133, 265-285.

Schlichting, H., Truckenbrodt, E. 1969. “Aerodynamik des Flugzeuges, Zweiter Band: Aerodynamik des Tragflügels (Teil 2), des Rumpfes, der Flügel-Rumpf-Anordnung und der Leitwerke“, Springer Verlag, Berlin/Göttingen/Heidelberg.

Schwarzbözl, P., Pitz-Paal, R., Schmitz, M., 2009. “Visual HFLCAL - A Software Tool for Layout and Optimization of Heliostat Fields”. In: Proceedings SolarPACES 2009, Berlin.

Scruton, C., 1981. “An Introduction to Wind Effects on Structures“. Engineering design guides 40, Oxford University Press.

SEI/ASCE 7-02, 2003, Minimum Design Loads For Buildings and Other Structures, ASCE/SEI, 298.

Sergent, E., 2002. “Vers une Méthodologie de Couplage entre la Simulation des Grandes Echelles et les Modèles Statistiques“, PhD Thesis, L’Ecole Centrale de Lyon.

Shirakashi, M., Yamaguchi, S., Mochimaru, Y., Yamane, R., 1988. “Coherent Structure in the Turbulent Wake Behind a Circular Cylinder”, Fluid Dynamics Research 4, 25-37, North-Holland.

Siegmeier, O., 2017. „Entwurf und Strukturoptimierung einer neuartigen Sandwichfacette für Heliostate“, master thesis, sbp-sonne, Technical University Berlin.

Siegmeier, O., et al. 2017. Cantilever-sandwich concentrator patent pending.

Sment, J., Ho, C.K., 2014. “Wind Patterns Over a Heliostat Field“. Energy Procedia 49, 229-238.

Spalart, P.R., 2000. “Strategies for Turbulence Modelling and Simulations”. International Journal of Heat and Fluid Flow, 21, 252-263.

Stenabaugh, S.E., Iida, Y., Kopp, G.A., Karava, P., 2015. “Wind Loads on Photovoltaic Arrays Mounted Parallel to Sloped Roofs on Low-Rise Buildings”, Journal of Wind Engineering and Industrial Aerodynamics 139, 16-26.

Strobel, K., Banks, D., 2014. “Effects of Vortex Shedding in Arrays of Long Inclined Flat Plates and Ramifications for Ground-Mounted Photovoltaic Arrays”, Journal of Wind Engineering and Industrial Aerodynamics 133, 146-149.

Taylor, G., 1938, “The spectrum of turbulence,” Proceedings of the Royal Society of London, 1938.

Tennekes, H., Lumley, J.L., 1972, A First Course in Turbulence, The MIT Press, Cambridge, Massachusetts, and London.

Teufel, E., Buck, R., Pfahl, A., Böing, G., Kunert, J., 2008, “Dimensioning of Heliostat Components Under Wind and Gravity Load: the Map Approach”, Proc. SolarPACES 2008 conference, Las Vegas, Nevada.

Torresol Energy, 2017, http://www.torresolenergy.com/TORRESOL/image-library/en?initdate=&enddate=&categoria=cw4e4122c7d262d, accessed January 2017.

Ulmer, S., 1998, “Influences of Cost Reduction Measures on the Beam Quality of a Large-Area Heliostat”, Diploma thesis, IER, University Stuttgart, Stuttgart, Germany.

Van der Hoven, I., 1957, “Power Spectrum of Horizontal Wind Speed in the Frequency Range from 0.0007 to 900 cycles per hour”, Journal of Meteorology, 14, 160-164.

Vásquez-Arango, J.F., 2016. “Dynamic Wind Loads on Heliostats”, PhD Thesis, DLR, Uni Aachen.

Vásquez-Arango, J.F., Buck, R., Pitz-Paal, R., 2015. “Dynamic Properties of a Heliostat Structure Determined by Numerical and Experimental Modal Analysis”, Journal of Solar Energy Engineering, 137 (5), 051001-051001. DOI: 10.1115/1.4030846.

Vieweger, G., 1989. “The Kryo-Kanal Köln – KKK”, DLR internal report, Cologne.

Wieringa, J., 1989. “Shapes of Annual Frequency Distributions of Wind Speed Observed on High Meteorological Masts”, Boundary-Layer Meteorology, 47, 85-110.

Wang Y.G., Li, Z.N., Gong, B., Li, Q.S., 2008. “Wind Pressure and Wind-Induced Vibration of Heliostat”, Key Engineering Materials, 400-402, 935-940.

Weinrebe, G., 2000, “Technische, ökologische und ökonomische Analyse von solarthermischen Turmkraftwerken”, PhD Thesis, Intitut für Energiewirtschaft und Rationelle Energieanwendung, Universität Stuttgart.

Wu, Z., Wang, Z., 2008. “Numerical Study of Wind Loads on Heliostat”. Progress in Computational Fluid Dynamics, 8, 503-509.

Wu, Z., Gong, B., Wang, Z., Li, Z., Zang, C., 2010. “An Experimental and Numerical Study of the Gap Effect on Wind Load on Heliostat”, Renewable Energy, 35, 797-806.

Zhang, H.-Q., Noack, B.R., Eckelmann, H., 1994. “Numerical Computation of the 3-D Cylinder Wake”. Technical Report, 3/1994, Max-Planck-Institut fuer Stroemungsforschung, Goettingen.

Appendix A: Extreme Value Statistics

Nomenclature

$1/a_c$	[-]	dispersion of c_{peak}
$1/a_U$	[m/s]	dispersion of $\widehat{U}_{mean}$
A	[m²]	mirror/PV panel surface
c	[-]	wind load coefficient
F	[N]	wind force
F_z	[N]	lift force
H	[m]	height of mirror/PV panel in stow position
I_u	[-]	turbulence intensity of longitudinal wind component at height H
l	[m]	characteristic lever arm length
k_1	[-]	constant of Weibull distribution
k_2	[-]	exponent of Weibull distribution
M	[Nm]	wind moment
M_c	[-]	mode of c_{peak} (value of highest probability)
M_{Hy}	[Nm]	hinge moment
M_U	[m/s]	mode of $\widehat{U}_{mean}$ (value of highest probability)
n	[-]	exponent of power law of mean wind speed profile
N	[-]	amount of samples
P	[-]	cumulative distribution function (CPF)
Q	[-]	probability of exceedance
p		probability density function (PDF) [1/product of dimensions of parameters]
T	[a]	return period of $\widehat{U}_{mean}$
T_0	[s]	averaging time: observation period over which atmospheric wind speeds are measured (as mean values of this time interval) and measuring period for the determination of the peak wind load coefficient respectively
U_{mean}	[m/s]	mean wind speed
$\widehat{U}_{mean}$	[m/s]	maximum annual mean wind speed
y_c	[-]	reduced wind load coefficient variate: $y_c = a_c(c_{peak,} - M_c)$
z	[m]	coordinate, vertical
ρ	[kg/m³]	density of air

BLWT	Boundary Layer Wind Tunnel
CPF	Cumulative Probability Function
CSP	Concentrating Solar Power
PDF	Probability Density Function
PV	Photo-Voltaic

A.1 Background and Task

Extreme value statistics is required for the determination of peak wind loads. The peak loads result from wind velocity fluctuations which have mainly two reasons (Mayne and Cook, 1978):

1. Climatic phenomena causing fluctuating pressure differences and thus acceleration of the air.
2. Ground roughness which disturbs the flow causing eddies.

By fluctuating climatic conditions wind arises. In interaction of the wind with the ground roughness vortices are generated. These are causing additional fluctuations but of higher frequencies. Usually, the fluctuations caused by the climate have a return period of one hour and more while the fluctuations caused by ground roughness have a return period of 10 min or less. Hence, fluctuations with frequencies corresponding to return periods between 10 min and 1 h are for most locations of comparably low power. This frequency band of low power is the so called “spectral gap” (Van der Hoven, 1957; Gomes and Vickery, 1977; Wieringa, 1989).

The rotational speed of eddies caused by the ground roughness increases proportional to the mean wind speed. Hence, the turbulent energy increases as well proportional to the mean speed in square. Therefore, turbulent energy spectra are usually normalised by the mean speed in square.

Because all velocity components increase proportional to the mean wind speed all wind loads increase proportional to the dynamic pressure of the mean wind speed (also wind loads which depend mainly on transversal velocity components like the lift force for horizontal plate). The impact of the turbulence intensity in interaction with the shape of the obstacle is quantified by specific peak wind load coefficients. The area of wind attack, or in the case of heliostats or PV trackers, the surface of the panel, is usually of linear impact. Therefore, all in all the wind loads can be expressed by formulas similar to the following and valid for a specific turbulence intensity:

$$F = c_F \frac{\rho}{2} U_{mean}^2 A \qquad \text{(A1)}$$

$$M = c_M \frac{\rho}{2} U_{mean}^2 A l \quad \text{(A2)}$$

with wind force *F*, wind moment *M*, wind load coefficient *c*, mean wind speed U_{mean}, panel surface *A,* and effective lever arm *l*.

To determine the wind load coefficients the interaction of the turbulent flow with the obstacle is usually simulated in boundary layer wind tunnels (BLWTs). The turbulent flow must be similar to the one at full scale. Than all fluctuations caused by the ground roughness of the site are captured by the BLWT tests. The impact of fluctuations caused by the climate is captured by the mean wind speed.

For the calculation of the maximum loads the maximum mean wind speed of the site has to be taken into account. If absolutely no failure would be risked the structures would have to become extremely strong and thus heavy and expensive because wind loads are stochastic values and may have extremely high values for extremely low probabilities. Therefore, it is common practice in wind engineering to determine wind load coefficients which leads to a rate of one failure every 50 years in average. Additionally, a safety factor has to be accounted for corresponding to the importance of the structure. For buildings this factors is of course very high so the risk of failure is very low. The maximum mean wind speed with 50 years return period is given for many countries by wind speed maps of national wind load standards.

The maximum mean wind loads with 50 years return period can be easily calculated with the maximum annual mean wind speed (with as well 50 years return period gained by wind speed maps), the mean wind load coefficient determined by BLWT tests, and equations (A1) and (A2). However, the mean wind loads are of minor relevance because the structures must of course resist also the peak wind loads caused by gusts. The determination of the maximum peak wind loads with 50 years return period is more complex because not only the annual maximum mean wind speed but also the peak wind load coefficients have a certain probability of occurrence. The task is to find the value of the peak wind load coefficient that leads in combination with the 50 year wind speed (which is usually known) to wind load values with a return period of 50 years. Therefore, extreme value statistics is needed. An appropriate method for it was found by (Cook and Mayne, 1980) and is described in the following. It takes advantage of the fact that maximum mean wind speed and maximum peak wind load coefficients are physically and therefore also statistically independent which is a precondition to calculate their joint probability. This is in general the case for an averaging time corresponding to a value within the “spectral gap”, which means between 10

min and 1 h. In particular, it is also the case for the hinge moment and lift force coefficients for a heliostat in stow position and an averaging time corresponding to the wind tunnel dimensions (see section 5.2.3.2.3).

A.2 Single Extreme Value Distribution

For the calculation of the wind loads with 50 years return period, the maximum annual mean wind speed with an annual probability of occurrence of Q = 1/50 has to be known. Values for it are given by many national wind load standards. The determination of these values is based on wind speed data. Thereby, the probability function of the annual extreme mean wind speed (averaged over one hour) is used. However, it cannot be determined directly because values of hundreds of years would be required. Fortunately, it can be determined indirectly because the probability function of the hourly mean wind speed is of a type (Weibull distribution) for which the probability density function of the extreme values is known (Fisher Tippett Type I distribution). When the function type of the extreme values is known, the extreme value distribution can be determined already with some few extreme values and their probability of occurrence (Mayne and Cook, 1978). This is shown in the following.

The mean wind speeds are Weibull distributed (Davenport, 1967). The corresponding cumulative distribution function (CPF) is:

$$P(U_{mean}) = 1 - e^{-\left(\frac{U_{mean}}{k_1}\right)^{k_2}} \tag{A3}$$

with probability P, the constant k_1 and the exponent k_2 of the Weibull distribution.

The corresponding Fisher Tippett Type I distribution (Fisher and Tippett, 1928) of the annual maximum mean wind speed is the following:

$$P(\hat{U}_{mean}) = e^{-e^{-a_U(\hat{U}_{mean} - M_U)}} \tag{A4}$$

with the annual maximum mean wind speed $\hat{U}_{mean}$, dispersion of $\hat{U}_{mean}$ $1/a_U$, and mode of $\hat{U}_{mean}$ M_U. The mode M_U is the $\hat{U}_{mean}$ of highest probability. The dispersion $1/a_U$ is a measure how much $\hat{U}_{mean}$ varies about M_U (parallels can be seen between the mode and the mean value of Gaussian distributions and between the dispersion and the standard deviation of Gaussian distributions).

The cumulative annual probability of occurrence is calculated by

$$P(\hat{U}_{mean}) = 1 - \frac{1}{T} \tag{A5}$$

with return period T (usually 50 years).

With (A4) and (A5) the annual maximum mean wind speed with return period T can be calculated:

$$\widehat{U}_{mean,T} = M_U - \frac{1}{a_U} ln\left(-\ln(1-\frac{1}{T})\right) \quad \text{(A6)}$$

however, for this mode M_U and dispersion $1/a_U$ must be known. These values can be determined on the base of a data set of $\widehat{U}_{mean}$ for several years N. The procedure is the following (Cook, 1985, C.3.2):

1. The N $\widehat{U}_{mean}$ are listed from the lowest to the highest.
2. The cumulative probability of the lowest $\widehat{U}_{mean}$ is $(\widehat{U}_{mean,lowest}) = 1/(N+1)$, for the second lowest $2/(N+1)$ and so on.
3. $a_U\left(\widehat{U}_{mean} - M_U\right) = -\ln(-\ln\left(P\left(\widehat{U}_{mean}\right)\right))$ can be calculated for each $P(\widehat{U}_{mean})$.
4. $\widehat{U}_{mean}$ is plotted over $a_U\left(\widehat{U}_{mean} - M_U\right)$ to achieve the so called Gumbel Plot (Gumbel, 1958). The graph is fitted by a straight line.
5. The $\widehat{U}_{mean}$ value at $a_U\left(\widehat{U}_{mean} - M_U\right) = 0$ is the mode M_U, the slope of the line the dispersion $1/a_U$.

An example Gumbel plot is given by Fig. 87 (annual maximum mean wind data of Albuquerque with averaging time T_0 = 3 s (NIST, 2015) reduced by power law with exponent n = 0.15 to a height of 2.4 m). With the graph it follows M_U = 23.0 m/s and $1/a_U$ = 2.58 m/s. With these values and (A6) the annual maximum mean wind speed with a return period of 50 years can be calculated: $\widehat{U}_{mean,T=50\ \text{years}}$ = 33.1 m/s.

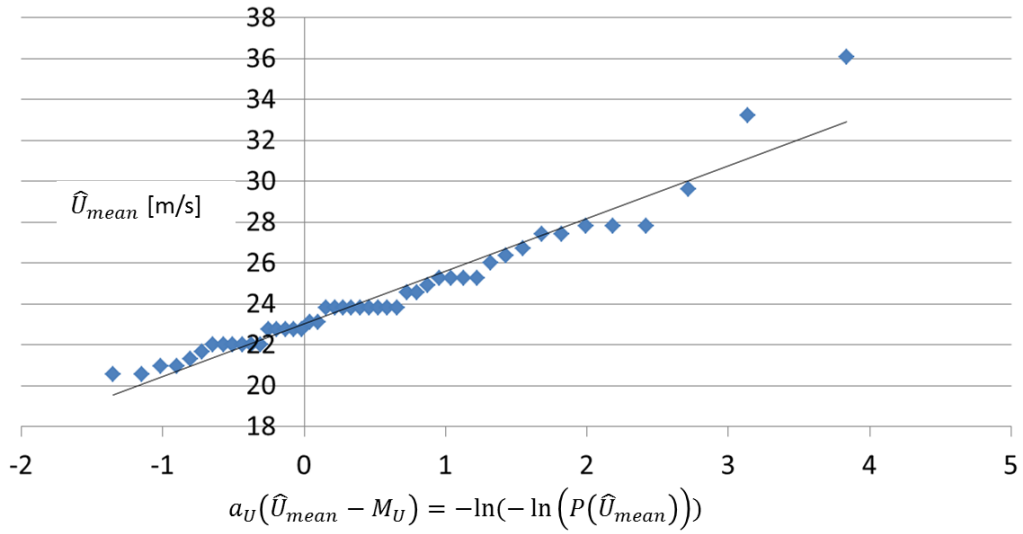

Fig. 87: Gumbel plot of annual maximum mean wind speed for T_0 = 3s and 2.4m height, Albuquerque, NM for the years 1933-1977 (NIST, 2015)

The higher the slope of the CPF for a certain $\hat{U}_{mean}$ the higher is its "probability density" ($\Delta P/\Delta \hat{U}_{mean}$). Hence, the probability density function (PDF) corresponds to the derivation of the CPF (Mayne and Cook, 1978, C4):

$$p(\hat{U}_{mean}) = \frac{\mathrm{d}}{\mathrm{d}\hat{U}_{mean}} P(\hat{U}_{mean}) = \frac{\mathrm{d}}{\mathrm{d}\hat{U}_{mean}} e^{-e^{-a_U(\hat{U}_{mean}-M_U)}} \quad \text{(A7)}$$

$$= -e^{-e^{-a_U(\hat{U}_{mean}-M_U)}} \frac{\mathrm{d}}{\mathrm{d}\hat{U}_{mean}} e^{-a_U(\hat{U}_{mean}-M_U)}$$

$$= e^{-a_U(\hat{U}_{mean}-M_U)} e^{-e^{-a_U(\hat{U}_{mean}-M_U)}} \frac{\mathrm{d}a_U(\hat{U}_{mean}-M_U)}{\mathrm{d}\hat{U}_{mean}}$$

$$= a_U e^{-a_U(\hat{U}_{mean}-M_U)} e^{-e^{-a_U(\hat{U}_{mean}-M_U)}}$$

Fig. 88 shows the measured (blue line, NIST, 2015) and corresponding calculated CPF (red line, according to equation (A4) and to the method described above) and the corresponding PDF (green line, according to equation (A7).

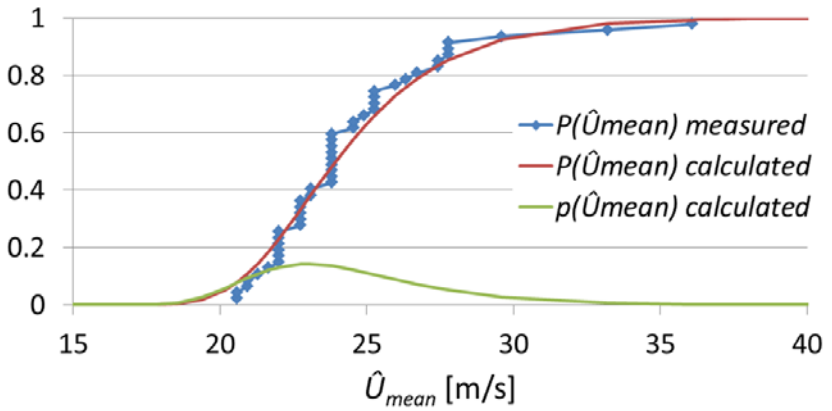

Fig. 88: Cumulative probability function (CPF) $P(\hat{U}_{mean})$, measured (blue, (NIST, 2015)) and calculated (red) and calculated probability density function (PDF) $p(\hat{U}_{mean})$ (green)

The PDF of peak wind load coefficients is as well of a type to which a Fisher-Tippett Type I distribution for extreme values corresponds (Mayne and Cook, 1978, 6). Hence, the PDF of the peak wind load coefficients can be determined in the same way as the PDF of $\hat{U}_{mean}$. As an example, the Gumbel plot of the 3s peak lift coefficient c_{Fz} for a flat plate with surface A = 19 m² at H = 2.4 m in longitudinal flow with turbulence intensity I_u = 21% at panel height H is given (Pfahl et al., 2015a). By the graph it follows mode M_c = 0.225 and dispersion $1/a_c$ = 0.0616 m/s.

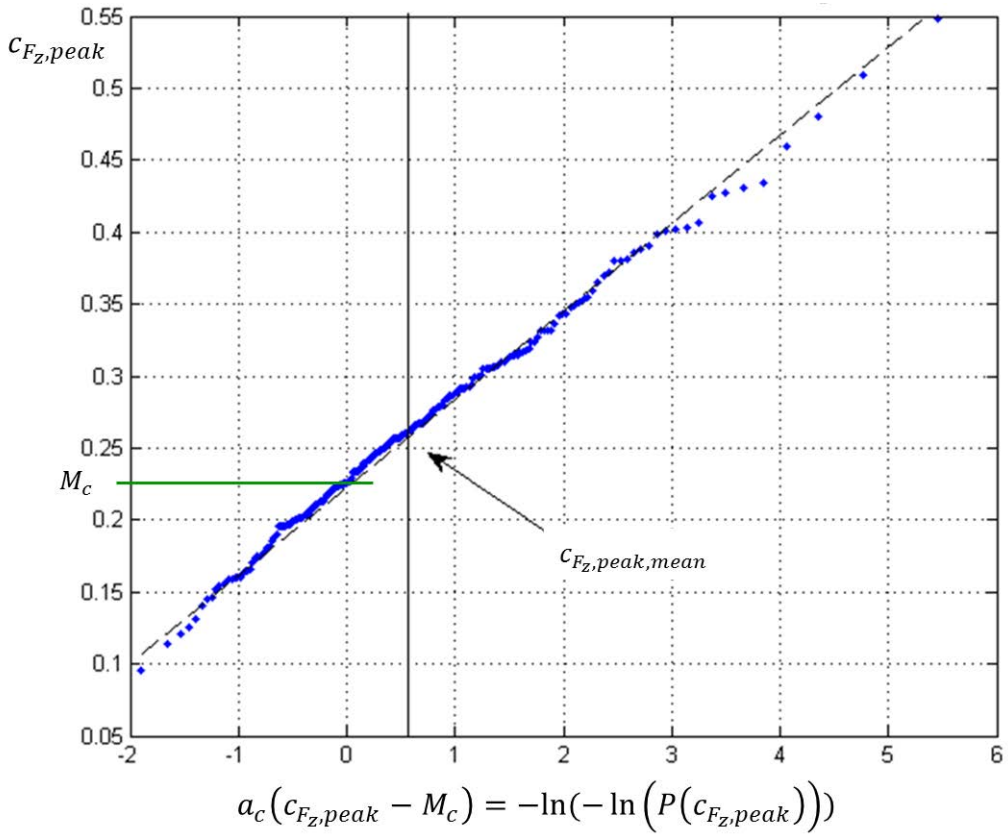

Fig. 89: Gumbel plot of 3s peak lift coefficient c_{F_z} for a flat plate with surface *A* = 19m² and aspect ratio 1.2 in longitudinal flow with turbulence intensity I_u = 21% at panel height *H* (Pfahl et al., 2015a)

A.3 Joint Extreme Value Distribution

For the calculation of the annual probability of a certain wind load value the probability distribution of the maximum annual mean wind speed and of the peak wind load coefficient are used. The probability density for the case that in a certain year a certain value of $\hat{U}_{mean}$ occurs and that during the averaging time interval T_0 of this maximum annual mean wind speed a peak wind load coefficient c_{peak} of a certain value occurs is (Mayne and Cook, 1978, 8.2):

$$p(c_{peak}, \hat{U}_{mean}) = p(c_{peak})p(\hat{U}_{mean}) \quad \text{(A8)}$$

The probability density of a certain peak wind force F_{peak} occurring for a certain $\hat{U}_{mean}$ is calculated by

$$p(F_{peak}, \hat{U}_{mean}) = p(F_{peak} = c_{peak}\frac{\rho}{2}\hat{U}_{mean}^2 A)p(\hat{U}_{mean}) \quad \text{(A9)}$$

with

$$p(F_{peak} = c_{peak}\frac{\rho}{2}\hat{U}_{mean}^2 A) = p(c_{F_{peak}} = \frac{F_{peak}}{\frac{\rho}{2}\hat{U}_{mean}^2 A})\frac{1}{\frac{\rho}{2}\hat{U}_{mean}^2 A} \quad \text{(A10)}$$

By the factor $\frac{1}{\frac{\rho}{2}\hat{U}_{mean}^2 A}$ the integration of $p(F_{peak}, \hat{U}_{mean})$ for fixed $\hat{U}_{mean}$ over all F_{peak} (area below graph) becomes 1 as generally required. This factor can be explained as follows: The result of an integration between two values of the peak wind forces $F_{peak,1}$ and $F_{peak,2}$ for $p(F_{peak})$ has to be equal to the result of an integration of $p(c_{peak} = \frac{F_{peak}}{\frac{\rho}{2}\hat{U}_{mean}^2 A})$ between the corresponding wind load coefficients $c_{peak,1}$ and $c_{peak,2}$. Hence, to compensate the differences of ($F_{peak,2}$ – $F_{peak,1}$) and ($c_{peak,2}$ – $c_{peak,1}$) at the calculations of the areas below the graphs the factor has to be equal to the ratio of these differences. With equation (A1) it follows:

$$\frac{p(F_{peak},\hat{U}_{mean})}{p(c_{peak},\hat{U}_{mean})} = \frac{c_{peak,2}-c_{peak,1}}{F_{peak,2}-F_{peak,1}} = \frac{(F_{peak,2}-F_{peak,1})/(\frac{\rho}{2}\hat{U}_{mean}^2 A)}{F_{peak,2}-F_{peak,1}} = \frac{1}{\frac{\rho}{2}\hat{U}_{mean}^2 A} = \frac{\mathrm{d}c_{peak}}{\mathrm{d}F_{peak}} \quad \text{(A11)}$$

For $\hat{U}_{mean} = M_U$ this is illustrated by Fig. 90. This factor leads for the integration of $p(F_{peak}, \hat{U}_{mean})$ (for varied $\hat{U}_{mean}$) over all possible F_{peak} and $\hat{U}_{mean}$ (volume below graph) as well to a value of 1.

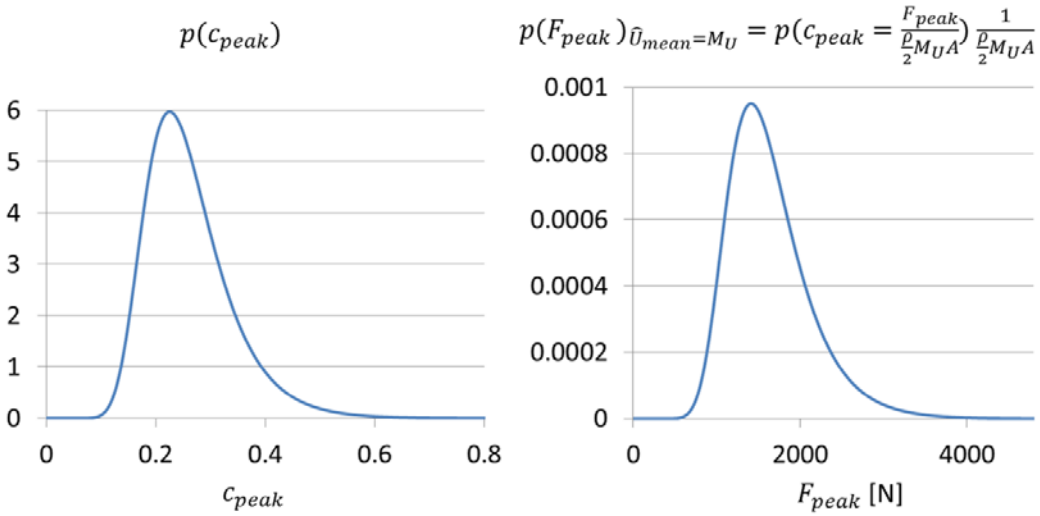

Fig. 90: PDF of wind load coefficient c_{peak} and of corresponding peak force F_{peak} for example case of fix $\hat{U}_{mean} = M_U$ (mode of wind speed); by the factor $\frac{1}{\frac{\rho}{2}M_U A}$ the integral of $p(F_{peak})_{\hat{U}_{mean}=M_U}$ (area below graph) is also 1 as required

Hence, it follows:

$$p(F_{peak}, \widehat{U}_{mean}) = p(c_{F_{peak}}, \widehat{U}_{mean}) \frac{\mathrm{d}c_{peak}}{\mathrm{d}F_{peak}} = p(c_{F_{peak}} = \frac{F_{peak}}{\frac{\rho}{2}\widehat{U}_{mean}^2 A}) p(\widehat{U}_{mean}) \frac{1}{\frac{\rho}{2}\widehat{U}_{mean}^2 A} \quad \text{(A12)}$$

An illustration of $p(F_{peak}, \widehat{U}_{mean})$ is given by Fig. 91 for the wind speed and wind load coefficient examples given in section A.2.

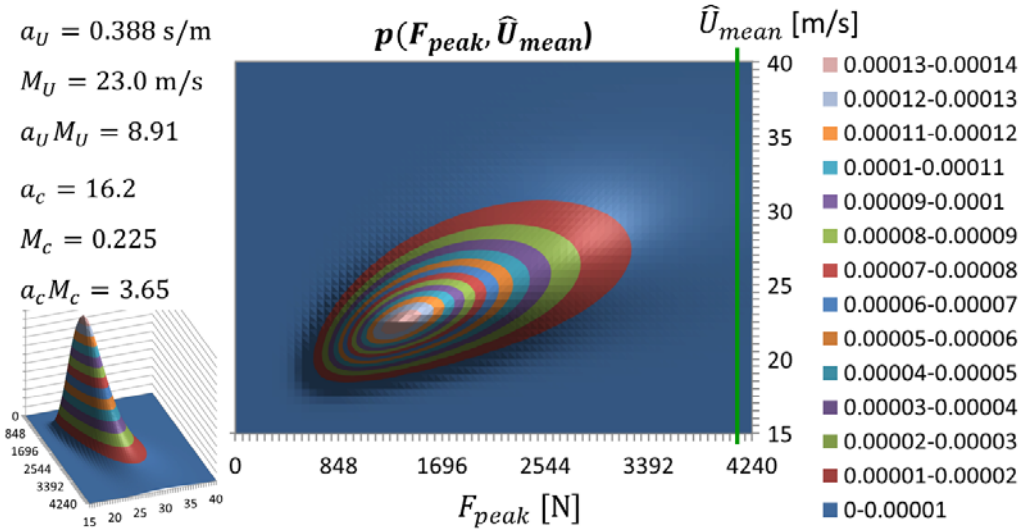

Fig. 91: $p(F_{peak}, \widehat{U}_{mean})$ for example wind speed and wind load coefficient distributions given in section A.2; green vertical line indicates F_{peak} with an annual probability of 0.02

The probability density of a certain wind force F_{peak} results from the integration of equation (A12) for this F_{peak} over all possible $\widehat{U}_{mean}$:

$$p(F_{peak}) = \int_0^\infty p(F_{peak}, \widehat{U}_{mean}) \, \mathrm{d}\widehat{U}_{mean} \quad \text{(A13)}$$

To find the probability that a certain wind force F^*_{peak} is exceeded equation (A13) must be integrated starting from F^*_{peak} over all possible higher wind forces:

$$1 - P(F^*_{peak}) = Q(F^*_{peak}) = \int_{F^*_{peak}}^\infty p(F_{peak}) \, \mathrm{d}F_{peak} \quad \text{(A14)}$$

The probability function of F_{peak} exceedance $Q(F_{peak})$ for the given example is illustrated by Fig. 92.

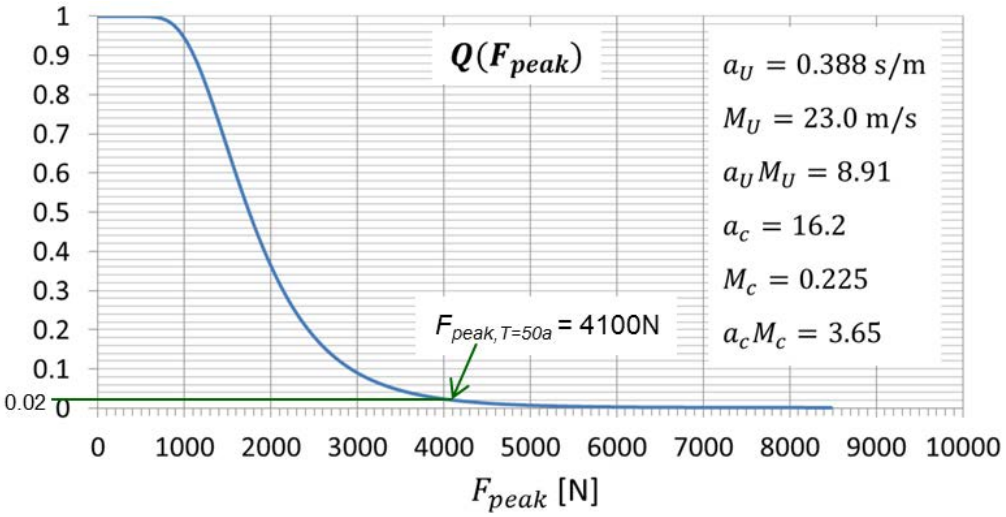

Fig. 92: Probability function of F_{peak} exceedance $Q(F_{peak})$ for given values

By the graph the peak load for any return period $F_{peak,T}$ can be determined with

$$Q(F_{peak}) = \frac{1}{T} \tag{A15}$$

For example, from Fig. 92 the peak force that is exceeded with a return period of T = 50 years is $F_{peak,T=50a}$ = 4100N. Hence, the volume below the graph of Fig. 91 on the right hand side of the vertical green line through F_{peak} = 4100N is Q = 1/50 = 0.02.

A.4 Second (and More) Highest Annual Mean Wind Speed

The shape of $p(F_{peak}, \hat{U}_{mean})$ depends on $a_U M_U$ and $a_c M_c$. Hence, for constant $a_U M_U$ and $a_c M_c$ the shape stays the same and $F_{peak,T}$ is proportional to M_U^2 and to M_c respectively which is illustrated in the following. Because of this fact a method could be developed by which the peak wind loads of a certain return period can be determined without the need of any integration (Cook and Mayne, 1979) and by which also the impact of the second (and more) highest annual mean speed can be taken into account (Cook and Mayne, 1980).

At the example of Fig. 93 M_c is doubled and a_c is of half value for constant $a_c M_c$. The shape of $p(F_{peak}, \hat{U}_{mean})$ is equal but the values of F_{peak} are doubled because of the doubled c_{peak} values. By this, the area below the graph is doubled as well. However, the volume below the graph is still 1 (as required) because the corresponding values of $p(F_{peak}, \hat{U}_{mean})$ are only of half value (height of the graph given by the column on the right).

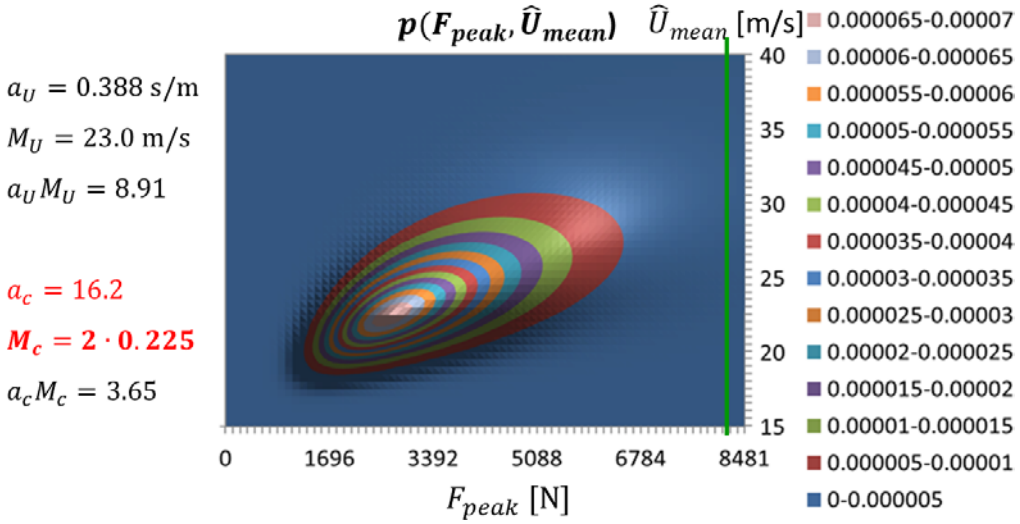

Fig. 93: $p(F_{peak}, \hat{U}_{mean})$ for doubled M_c and same $a_U M_U$, M_u and $a_c M_c$ compared to Fig. 91

The line indicating the area with probability 0.02 must stay at the same position (related to the shape of the PDF), see green line of Fig. 93. Because F_{peak} is doubled in general it is also doubled at the position of the 0.02 probability line and it follows $F_{peak,T=50a}$ = 8200N which is confirmed by the value gained by $Q(F_{peak})$ (Fig. 94). Hence, it could be shown that $F_{peak,T}$ is proportional to M_c.

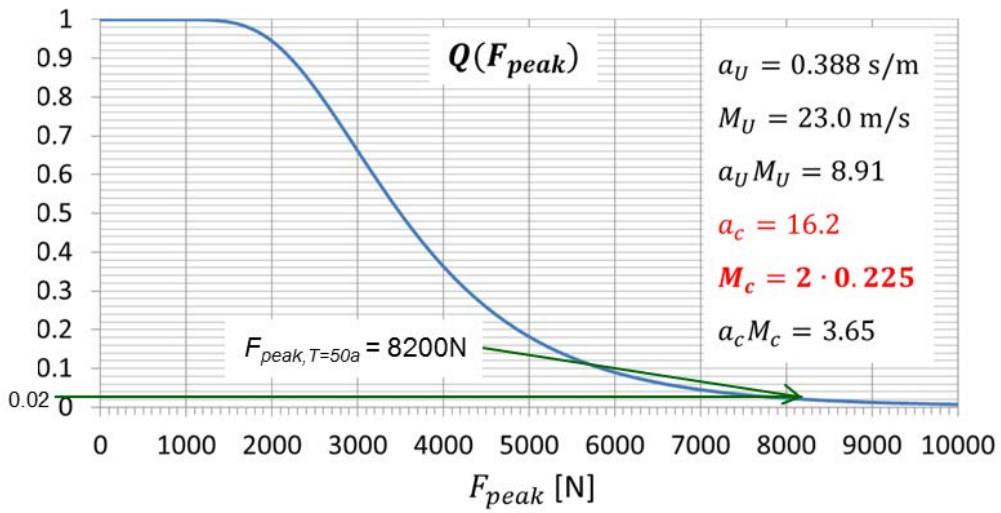

Fig. 94: Probability function of F_{peak} exceedance $Q(F_{peak})$ for doubled M_c

F_{peak} is doubled as well by increasing M_U (and therefore all $\hat{U}_{mean}$ values) by a factor of $\sqrt{2}$ because $F_{peak} \sim \hat{U}_{mean}^2$, compare (A1). All in all the area below the graph $p(F_{peak}, \hat{U}_{mean})$ is stretched by a factor of $2\sqrt{2}$. By the same factor the values of $p(F_{peak}, \hat{U}_{mean})$ are reduced (values of column on the right) to get a value of 1 for the volume below the graph.

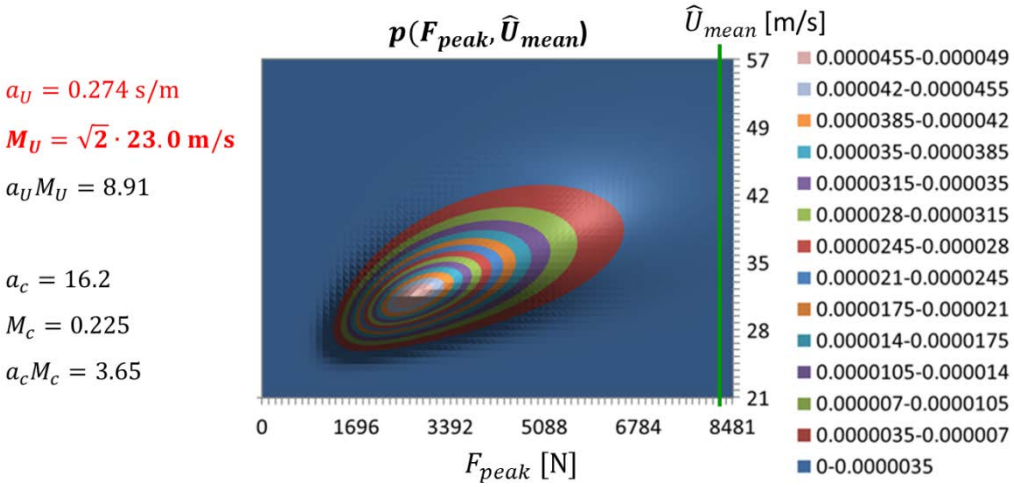

Fig. 95: $p(F_{peak}, \hat{U}_{mean})$ for $\sqrt{2}$ higher M_U and same $a_U M_U$, M_c and $a_c M_c$ compared to Fig. 91

As F_{peak} is doubled in general $F_{peak,T=50a}$ is doubled as well, compare the green 0.02 probability line at F_{peak} = 8200N of Fig. 95 and Fig. 96. Hence, it could be demonstrated that $F_{peak,T}$ is proportional to M_U^2.

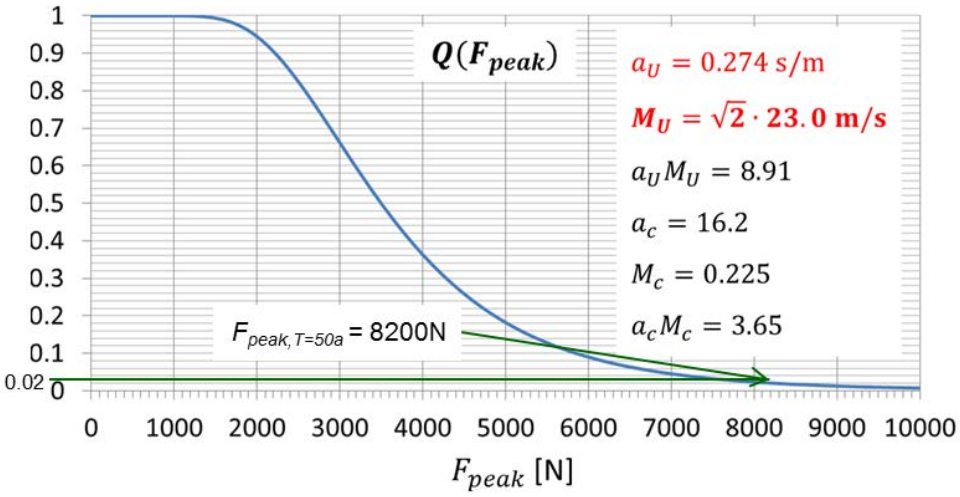

Fig. 96: Probability function of F_{peak} exceedance $Q(F_{peak})$ for $\sqrt{2}$ higher M_U

Usually, the peak load coefficients are needed which in combination with the maximum annual mean wind speed of 50 years return period $\hat{U}_{mean,T=50a}$ (which is usually available by the wind load standards) give with equation (A1) or (A2) respectively the wind load for T = 50 years. This value is achieved by

$$c_{F_{peak,T=50a}} = \frac{F_{peak,T=50a}}{\frac{\rho}{2}\hat{U}^2_{mean,T=50a}A} \tag{A16}$$

From all this it follows that for constant $a_U M_U$ and $a_c M_c$ peak wind load of a certain return period $F_{peak,T}$ is proportional to M_c and to M_U^2. Hence, if $F_{peak,T}$ is known for certain $a_U M_U$ and $a_c M_c$ values $F_{peak,T}$ can be determined for any other values of M_U and M_c (for same $a_U M_U$, $a_c M_c$ and T) without the need of integrations of equations (A13) and (A14). Because of this fact, (Cook and Mayne, 1979) are able to provide diagrams for different T by which the values of $y_{c,T} = a_c\left(c_{peak,T} - M_c\right)$ are given for varied $a_U M_U$ and $a_c M_c$. With this value the required peak wind load coefficient can be determined:

$$c_{peak,T} = \frac{y_{c,T}}{a_c} + M_c \tag{A17}$$

The method described above accounts only for the annual maximum mean wind speeds. However, it could be possible that in one year not the maximum mean wind speed lead to the maximum wind loads but the second (or more) highest annual mean wind speed. This could happen if during T_0 of the maximum mean wind speed a comparably low wind load coefficient occurs while at the second (or more) highest annual mean wind speed a sufficiently higher one. The determination of the diagrams of $y_{c,T}$ taking also the probability of such events into account is not possible by integration anymore and numerical methods using random values (Monte Carlo method) are required (Cook and Mayne, 1980). Corresponding tables for y_c of wider range are provided by Cook (1990).

Appendix B: Eddy Diameters and Turbulent Energy Spectra

Abstract

In this section it is tried to give a figurative explanation of the turbulent energy spectra based on the model of the turbulent flow as a superposition of eddies of different sizes and hence, frequencies (Geurts, 1997, p. 30). At first, equations are given by which the full scale spectra can be calculated (Von Karmann Spectra modified according to the results of full scale measurements). Then the Rankine model of the velocity distribution within vortices is described. The correlation between the diameter of the vortices and the frequency of the sinusoidal signal of the wind speed fluctuations caused by them is explained by the flow field behind a circular tube generating a vortex street. Finally, it is shown how a pure sinusoidal signal would impact the autocorrelation function and by this the spectral density function.

Nomenclature

$d_{cylinder}$	[cm]	diameter of circular cylindrical tube
D_{eddy}	[m]	diameter of eddy
f	[1/s]	frequency of wind speed fluctuation
f^*	[1/s]	normalised frequency of wind speed fluctuation ($f^* = fh/U_{mean}$)
F_1, F_2	[-]	auxiliary variables for modified von Karman equations
K	[m²/s]	circulation
r	[m]	radius
R_{uu}	[m²/s²]	autocorrelation function of u in x-direction
R_{ww}	[m²/s²]	autocorrelation function of w in z-direction
S_{uu}, S_{ww}	[m²/s]	spectral density functions of u and w-components
Sr	[-]	Strouhal number
t	[s]	time
T	[s]	time (limit of integration)
T_{return}	*[s]*	return period
u	[m/s]	fluctuating horizontal longitudinal wind component
$\hat{u}$	[m/s]	amplitude of sinusoidal wind speed signal
U_{mean}	[m/s]	mean horizontal longitudinal wind component for T_0
V	[m/s]	tangential velocity within a vortex
w	[m/s]	fluctuating vertical wind component

β_1, β_2	[-]	factors in modified von Karman equations
$\Delta\omega$	[1/s]	angular frequency difference
γ_u, γ_w	[-]	auxiliary variables for modified von Karman equations
φ	[rad]	phase shift φ of cosine signal
σ_u	[m/s]	standard deviation of wind fluctuations in longitudinal direction
τ	[s]	time shift between two signals
ω	[1/s]	angular frequency = $2\pi f$

BLWT	boundary layer wind tunnel
PV	Photo-Voltaic

B.1 Boundary Layer Turbulent Energy Spectra

For the determination of wind loads by a BLWT the spectra of the wind tunnel must match the spectra of the atmospheric boundary layer of the site where the heliostats or PV trackers are located. The spectral density functions of the *u*- component in the BLWT (and similar the *v*- and *w*-components) are determined by Panofsky and Dutton (1984, 3.7) with the angular frequency

$$\omega = 2\pi f \tag{B1}$$

$$S_{uu}(\omega) = \frac{1}{\pi}\int_{-\infty}^{\infty} R_{uu}(\tau) e^{i\omega\tau} d\tau \tag{B2}$$

The autocorrelation function is calculated by

$$R_{uu}(\tau) = E\{u(t)u(t+\tau)\} = \frac{1}{2T}\int_{-T}^{T} u(t)u(t+\tau)dt \tag{B3}$$

with $T \rightarrow \infty$.

(The inverse transform of equation (B2) is $R_{uu}(\tau) = \frac{1}{2}\int_{-\infty}^{\infty} S_{uu}(\omega) e^{-i\omega\tau} d\omega$. The factors ½ and 1/π of equation (B2) are needed to reach a complete inverse transform.)

Equation (B2) can be simplified:

$$S_{uu}(\omega) = \frac{1}{\pi}\int_{-\infty}^{\infty} R_{uu}(\tau)[\cos\omega\tau + i\sin\omega\tau] d\tau \tag{B4}$$

Because of stationarity it follows

$$R(\tau) = R(-\tau) \tag{B5}$$

and equation (B4) can be written as

$$S_{uu}(\omega) = \frac{2}{\pi}\int_{0}^{\infty} R_{uu}(\tau)\cos\omega\tau\, d\tau \tag{B6}$$

Formulas for the spectra of the atmospheric boundary layer are given by ESDU 85020, B4.1 to B4.4.

$$\frac{f \cdot S_{uu}}{U_{mean}^2} = \frac{\sigma_u^2}{U_{mean}^2}\left(\beta_1 \frac{2.987 f^* \gamma_u}{[1+(2\pi f^* \gamma_u)^2]^{5/6}} + \beta_2 \frac{1.294 f^* \gamma_u}{[1+(\pi f^* \gamma_u)^2]^{5/6}} F_1\right) \quad \text{(B7)}$$

$$\frac{f \cdot S_{ww}}{U_{mean}^2} = \frac{\sigma_w^2}{U_{mean}^2}\left(\beta_1 \frac{2.987\left[1+(8/3)(4\pi f^* \gamma_w)^2\right] f^* \gamma_w}{[1+(4\pi f^* \gamma_w)^2]^{11/6}} + \beta_2 \frac{1.294 f^* \gamma_w}{[1+(2\pi f^* \gamma_w)^2]^{5/6}} F_2\right) \quad \text{(B8)}$$

B.2 Rankine Vortex

An eddy may be represented as a mass of fluid rotating around a centre (Cook, 1985, p.20 et seqq.). Particles that change their distance to the centre would conserve their angular momentum if viscosity could be neglected. In this case, the product of tangential velocity *V* and the distance to the centre *r*, the circulation *K*, is a constant value at any point of the vortex:

$$K = Vr = constant \quad \text{(B9)}$$

However, towards the centre, the velocity gradient would increase and therefore viscosity cannot be neglected especially near the centre. In viscid flow, any slip between annular elements is resisted by a viscous torque which leads to a constant value of the angular velocity *ω* which is the quotient of velocity *V* and distance to the centre *r*:

$$\omega = \frac{V}{r} = constant \quad \text{(B10)}$$

For large distances, velocity and thus Reynolds number increases and inertia dominates viscosity. Hence, far from the centre, the vortex model neglecting viscosity is more appropriate while near the centre the model for viscid flow. This combined vortex model is called Rankine vortex (see Fig. 97) and is in relatively good agreement with real vortices.

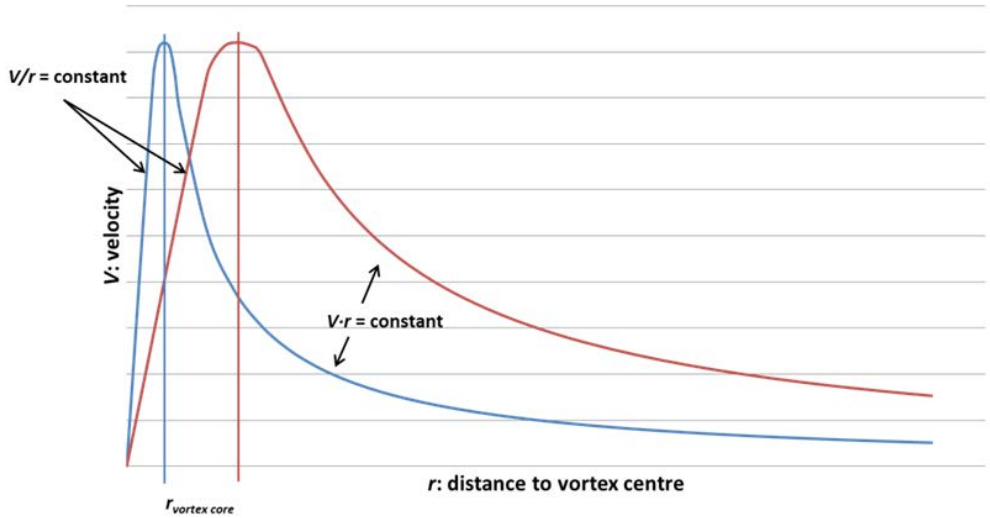

Fig. 97: Two Rankine vortices with different core radii

B.3 Vortex Diameters and Frequencies

Von Kármán and Rubach (1912) developed a model for vortex streets. The vortices develop into two lines. Within one line the vortices are of same rotational direction but of opposite rotational direction to the vortices of the other line. The distance between the vortices is defined by stability considerations. The resulting periodicity was validated by many measurements (e.g. (Ahlborn et al., 1998)) and simulations (e.g. (Zhang et al., 1995). A phenomenological model for the vortex shedding process was analytically derived by Ahlborn et al. (2002).

The flow field behind a circular cylinder generating a vortex street is visualised by Fig. 98 to explain how the frequencies of the longitudinal and vertical velocity fluctuations correspond to the diameter of the vortices of the flow. The background colours give the longitudinal velocity component field *u*. Yellow to red is indicating velocity above the approach wind speed and green to dark blue velocity below it. The streamlines are given by the black lines. The blue circles with arrows indicate the diameter of maximum tangential speed of an eddy. When in direction with the main flow, highest *u* occurs (red regions) while when against the flow low *u* results (light blue regions). The dashed blue lines represent the outer diameter of an eddy. Eddies of upper and lower row may overlap for regions of same tangential flow direction (Ahlborn et al., 2002, Fig. 1). Eddies of same row cannot overlap because their tangential flow direction is contrary. Therefore, their distances to each other correspond to their diameters. The most intensive fluctuations of the vertical velocity component *w* occur in the centre plane (green line) with highest gradients of

the streamlines. The highest fluctuations of *u* occur in the planes through regions of high (red) and low (light blue) *u* (indicated by dashed purple lines). The fluctuations of *u* and *w* are of same frequency with a phase shift of +/- π/2 (Fig. 98, below) (Antonia et al., 1993).

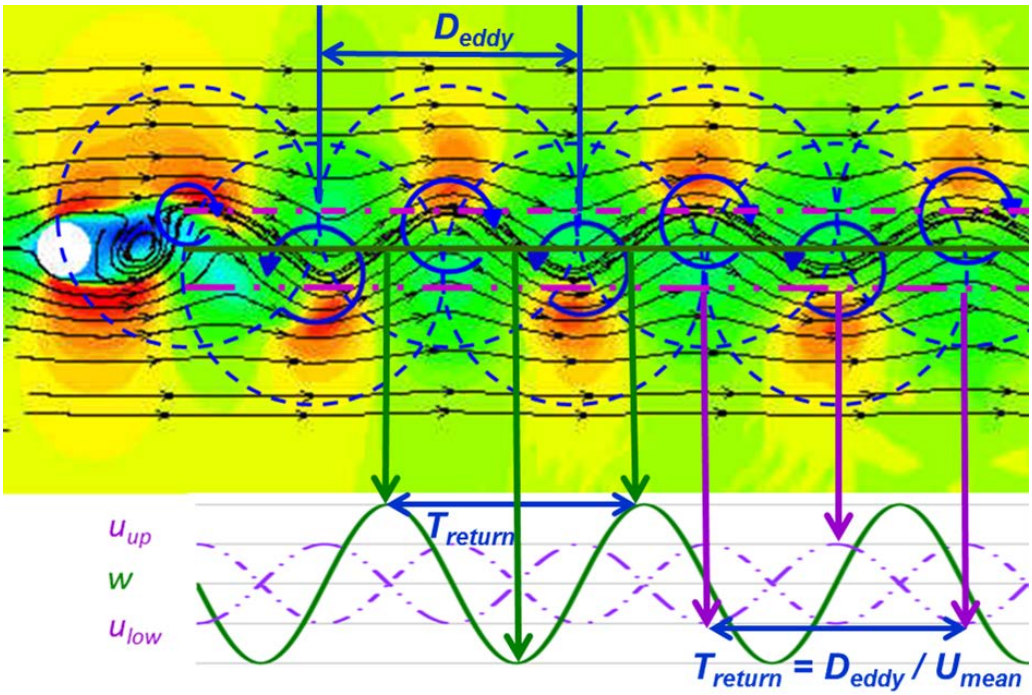

Fig. 98: Top: Von Karman vortex street visualisation of longitudinal velocity component *u* field (background colours) and streamlines (black) (INP-ENSEEIHT, 2015), diameter of highest velocity of generated vortices (blue circles with arrows) and their outer diameter (dashed circles), planes of maximum longitudinal (upper and lower dashed purple line) and of maximum vertical (central green line) velocity fluctuations; Below: Maximum fluctuations of longitudinal (dashed purple lines) and vertical (green line) velocity components *u* and *w*.

The return period T_{return} of the peak fluctuations corresponds to the time an eddy needs to pass a certain point with its outer diameter (Fig. 98):

$$T_{return} = \frac{D_{eddy}}{U_{mean}} = \frac{1}{f} \,. \qquad \text{(B11)}$$

Hence, the diameter of eddies corresponding to a certain frequency can be calculated by

$$D_{eddy} = \frac{U_{mean}}{f_{eddy}} \,. \qquad \text{(B12)}$$

The frequencies of the peak fluctuations correspond to the separation frequency which can be calculated by

$$f_{peak} = f_{separation} = \mathrm{Sr}\frac{U_{mean}}{d} \tag{B13}$$

With a Strouhal number of

$$\mathrm{Sr} = 0.2 \tag{B14}$$

for circular cylinders and with equations (B11) and (B13) the ratio of the diameter of the eddies D_{eddy} to the diameter of the circular cylinder generating these eddies $d_{cylinder}$ follows (compare diameter of circular (white) cylinder with outer diameter of eddies (dashed blue lines) of Fig. 98):

$$\frac{D_{eddy}}{d_{cylinder}} = \frac{1}{\mathrm{Sr}} = 5. \tag{B15}$$

B.4 Spectral Density Function

Wind speed measurement signals can be regarded as a superposition of an infinitesimal amount of sinusoidal signals of varied angular frequency ω and different amplitudes. In the following, the spectral density function is explained by investigating the ideal case of a vortex street causing a pure cosine signal (which is not possible in reality) with angular frequency ω and amplitude $\hat{u}$:

$$u(t) = \hat{u}\cos\omega t. \tag{B16}$$

The spectral density functions of the *u*- and of the *w*-component are defined by the Fourier transform of their autocorrelation functions (see section B.1).With equation (B16) the autocorrelation function (B3) becomes

$$R_{uu}(\tau) = \frac{\hat{u}^2}{2T}\int_{-T}^{T}\cos\omega t\cos\omega(t+\tau)dt. \tag{B17}$$

Fig. 99 illustrates how $\cos(\omega t)\cdot\cos(\omega(t+\tau))$ varies with $\omega\tau$. The integral of $\cos(\omega t)\cdot\cos(\omega(t+\tau))$ is equal to the area which is enclosed by the graph and the abscissa and becomes 0 for $\omega\tau = \pi/2$ and $\omega\tau = 3\pi/2$ because areas of positive and negative sign are of same absolute value and cancel each other out. The maximum value result for $\omega\tau = 0$ (and 2π) and the minimum one for $\omega\tau = \pi$ because all areas are positive or negative respectively.

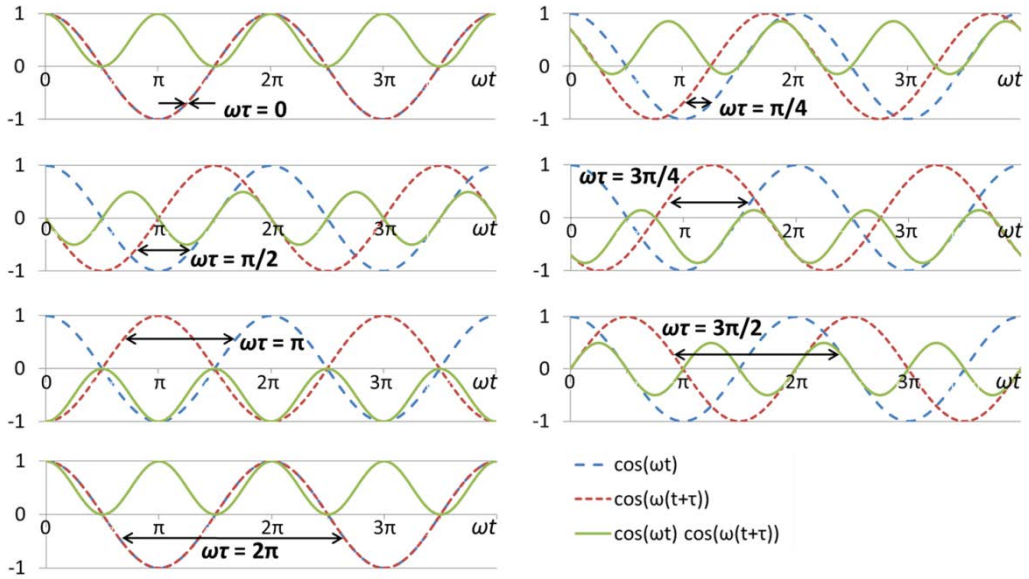

Fig. 99: Illustration of cos(*ωt*)·cos(*ω*(*t*+*τ*)) for different *ωτ*

For $\omega\tau = \pi$ the autocorrelation function (B3) equals the definition of the variance (square of the standard deviation):

$$R_{uu}(\tau = 0) = \frac{1}{2T}\int_{-T}^{T} u^2(t)dt = \sigma_u^2 \qquad \text{(B18)}$$

The results would be the same for any phase shift *φ* of the cosine signal

$$u(t) = \hat{u}\cos(\omega t + \varphi) \qquad \text{(B19)}$$

because the area below the integral of cos(*ωt*+*φ*)·cos(*ω*(*t*+*τ*)+*φ*) is independent of *φ*.

All in all it results that the autocorrelation function transfers any sinusoidal oscillation (equation (B19)) into a cosine function of same frequency with the variance as amplitude:

$$R_{uu}(\tau) = \frac{\hat{u}^2}{2T}\int_{-T}^{T} \cos(\omega t + \varphi)\cos(\omega(t+\tau)+\varphi)dt = \sigma_u^2 \cos\omega\tau. \qquad \text{(B20)}$$

The Fourier transform (B6) would be infinite for a pure sinusoidal correlation function (B20) for the angular frequency *ω*:

$$S_{uu}(\omega) = \frac{\sigma_u^2}{\pi}\int_0^{\infty} \cos\omega\tau\cos\omega\tau\, d\tau. \qquad \text{(B21)}$$

($S_{uu}(\omega)$ represents the turbulent energy. However, it would not be infinitesimal because the width of *ω* is infinitesimally small.)

For all other angular frequencies *ω* + Δ*ω* the Fourier transform is

$$S_{uu}(\omega + \Delta\omega) = \frac{\sigma_u^2}{\pi} \int_0^\infty \cos(\omega\tau) \cos((\omega + \Delta\omega)\tau)\, d\tau = 0 \qquad \text{for } \Delta\omega \neq 0 \qquad \text{(B22)}$$

because positive and negative sections of the integral (areas enclosed by graph and abscissa) would cancel each other out, see Fig. 100.

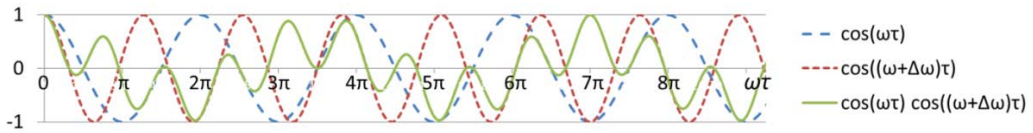

Fig. 100: Illustration of cos(ωτ)·cos((ω+Δω)τ))

At real, no sinusoidal oscillation of only one frequency exist but a mixture of an infinitesimal amount of frequencies. A main reason for it is that eddies continuously dissociate into smaller ones. Therefore, the autocorrelation functions do not look like the graphs given in Fig. 99 but rapidly tend against zero. Nevertheless, figuratively speaking, eddies of a certain size and frequency will give a certain contribution to the autocorrelation function (B3) for this frequency so it becomes somewhat “more similar” to a cosine function of this frequency. Hence, they also contribute to the value of the spectral density function (B6) at this frequency. In this way, the spectral density function “detects” the contribution of a certain frequency and adds it to the value of the total turbulent energy.

Curriculum Vitae

Andreas Pfahl was born on 24-01-1967 in Frankfurt/Main Germany. After obtaining the university-entrance diploma in 1986 at the Georg Kerschensteiner Schule in Bad Homburg Germany, he studied Mechanical Engineering at the Technical University Darmstadt and Stuttgart University in Germany. In 1994 he graduated within the DLR Institute of Technical Thermodynamics on two-phase flows in solar trough receivers with direct evaporation. Afterwards, he studied Catholic Theology at the Philosophical-Theological University Sankt-George in Frankfurt/Main Germany and graduated in 2000. Since 2001 he is employed at the German Aerospace Center (DLR). His research at the Institute of Solar Research led to several publications and several of his inventions are patented. From 2011 he started part-time PhD research at Eindhoven University of Technology in the Netherlands, the results of which are presented in this dissertation.

List of Publications

2018 Pfahl, A., Rheinländer, J., Krause, A., Buck, R., Giuliano, S., Hertel, J., *Test of the First Lay-Down Heliostat with Monolithic Mirror-Panel and Closed Loop Control*. Conference abstract submitted.

2018 Pfahl, A., Zaschke, M., Geurts, C.P.W., Buselmeier, M., *Impact of Turbulent Energy Spectra Characteristics on Wind Loading of Heliostats and PV Trackers in Stow*. Journal paper manuscript submitted.

2017 Pfahl, A., Gross, F., Liedke, P., Hertel, J., Rheinländer, J., Mehta, S., Vásquez-Arango, J.F., Giuliano, S., Buck, R., *Reduced to Minimum Cost: Lay-Down Heliostat with Monolithic Mirror-Panel and Closed Loop Control*. Proc. SolarPACES 2017 conference, Santiago de Chile.

2017 Pfahl, A., Coventry, J., Röger, M., Wolfertstetter, F., Vasquez, F., Gross, F., Arjomandi, M., Schwarzbözl, P., Geiger, M., Liedke, P., *Progress in Heliostat Development*. Solar Energy 152, 3-37.

2016 Liedke, P, Lewandowski, A., Pfahl, A., Hölle, E., *Precise Low Cost Chain Gears for Heliostats*, Proc. SolarPACES 2015 conference, Cape Town, AIP Conference Proceedings 1734, 020014; https://doi.org/10.1063/1.4949038.

2015 Pfahl, A., Bezerra, P.H.S., Hölle, E., Liedke, P., Teramoto, E.T., Hertel, J., Lampkowski, M., Oliveira, C.E.L., *Heliostat Tailored to Brazil*, ISES Solar World Congress 2015.

2015 Pfahl, A., Randt, M., Meier, F., Zaschke, M., Geurts, C.P.W., Buselmeier, M., *A Holistic Approach for low Cost Heliostat Fields*. Energy Procedia 69, 178-187.

2014 Pfahl, A., Brucks, A., Holze, C., *Wind Load Reduction for Light-Weight Heliostats*, Energy Procedia 49, 193-200.

2014 Pfahl, A., *Survey of Heliostat Concepts for Cost Reduction*, Solar Energy Engineering 136, 014501, 1-9.

2013 Pfahl, A., Randt, M., Holze, C., Unterschütz, S., *Autonomous Light-Weight Heliostat With Rim Drives*, Solar Energy 92, 230-240.

2012 Pfahl, A., Randt, M., Kubisch, S., Holze, C., Brüggen, H., *Autonomous Light-Weight Heliostat with Rim Drives*, Proc. SolarPACES 2012 conference, Marrakesh.

2012 Holze, C., Brüggen, H., Misseeuw, R., Cosijns, B., Albers, R., Isaza, D., Buck, R., Pfahl, A., *Laminated Solar Thin Glass Mirror Solution for Cost Effective CSP Systems*, Proc. SolarPACES 2012, Marrakesh.

2012 Buck, R., Pfahl, A., Roos, T.H., *Target Aligned Heliostat Field Layout for Non-Flat Terrain*, Proc. SASEC 2012 conference, Cape Town.

2011 Pfahl, A., Buselmeier, M., Zaschke, M., *Determination of Wind Loads on Heliostats*, Proc. SolarPACES 2011 conference, Granada.

2011 Pfahl, A., Buselmeier, M., Zaschke, M, 2011. *Wind Loads on Heliostats and Photovoltaic Trackers of Various Aspect Ratios*. Solar Energy 85, 2185-2201.

2011 Pfahl, A., Uhlemann, H., *Wind Loads on Heliostats and Photovoltaic Trackers at Various Reynolds Numbers*. Journal of Wind Engineering and Industrial Aerodynamics 99, 964-968.

2011 Kubisch, S., Randt, M., Buck, R., Pfahl, A., Unterschütz, S., *Wireless Heliostat and Control System for Large Self-Powered Heliostat Fields*. Proc. SolarPACES 2011 conference, Granada.

2010 Buck, R., Wurmhöringer, K., Lehle, R., Göttsche, J., Pfahl, A., *Development of a 30m² Heliostat with Hydraulic Drive*. Proc. SolarPACES 2010 conference, Perpignan.

2008 Teufel, E.; Buck, R.; Pfahl, A.; Böing, G.; Kunert, J.; *Dimensioning of Heliostat Components under Wind and Gravity Load: the Map Approach*. SolarPACES 2008, Las Vegas, Nevada.

2008 Amsbeck, L., Buck, R., Pfahl, A., Uhlig, R., *Optical Performance and Weight Estimation of a Heliostat With Ganged Facets*. Solar Energy Engineering 130, Issue 1, 011010.

2008 Pfahl, A., *Die Größe der Menschen und die kleine Welt der Physik*, in: W. Härle (Hg.) *Ethik im Kontinuum. Beiträge zur relationalen Erkenntnistheorie und Ontologie* (MThSt 97), Marburg, 29-38.

Patents

2016 Pfahl, A., Buck, R., Liedke, P., Gross, F., *Solar Device*. International patent WO 2016202941 A2, 2016.

2015 Prahl, C., Pfahl, A., Röger, M., *Heliostat für Solarkraftwerke oder Solarkonzentratoren.* German patent application 10 2015 202 084.3.

2012 Pfahl, A., *Schwenkvorrichtung und Heliostat.* European patent EP2012/075232.

2008 Pfahl, A., Buck, R., Rehschuh, K., *Method for controlling the orientation of a heliostat on a receiver, heliostat apparatus and solar power plant.* International patent WO2008/058866A1.

2005 Buck, R., Pfahl, A., *Heliostat and process for adjusting the reflecting surfaces of a heliostat.* European patent EP000001635128A2.

Bouwstenen is een publicatiereeks
van de Faculteit Bouwkunde,
Technische Universiteit Eindhoven.
Zij presenteert resultaten van
onderzoek en andere activiteiten op
het vakgebied der Bouwkunde,
uitgevoerd in het kader van deze
Faculteit.

Bouwstenen en andere proefschriften van de
TU/e zijn online beschikbaar via:
https://research.tue.nl/

Kernredactie
MTOZ

Reeds verschenen in de serie
Bouwstenen

nr 1
Elan: A Computer Model for Building Energy Design: Theory and Validation
Martin H. de Wit
H.H. Driessen
R.M.M. van der Velden

nr 2
Kwaliteit, Keuzevrijheid en Kosten: Evaluatie van Experiment Klarendal, Arnhem
J. Smeets
C. le Nobel
M. Broos
J. Frenken
A. v.d. Sanden

nr 3
Crooswijk: Van 'Bijzonder' naar 'Gewoon'
Vincent Smit
Kees Noort

nr 4
Staal in de Woningbouw
Edwin J.F. Delsing

nr 5
Mathematical Theory of Stressed Skin Action in Profiled Sheeting with Various Edge Conditions
Andre W.A.M.J. van den Bogaard

nr 6
Hoe Berekenbaar en Betrouwbaar is de Coëfficiënt k in x-ksigma en x-ks?
K.B. Lub
A.J. Bosch

nr 7
Het Typologisch Gereedschap: Een Verkennende Studie Omtrent Typologie en Omtrent de Aanpak van Typologisch Onderzoek
J.H. Luiten

nr 8
Informatievoorziening en Beheerprocessen
A. Nauta
Jos Smeets (red.)
Helga Fassbinder (projectleider)
Adrie Proveniers
J. v.d. Moosdijk

nr 9
Strukturering en Verwerking van Tijdgegevens voor de Uitvoering van Bouwwerken
ir. W.F. Schaefer
P.A. Erkelens

nr 10
Stedebouw en de Vorming van een Speciale Wetenschap
K. Doevendans

nr 11
Informatica en Ondersteuning van Ruimtelijke Besluitvorming
G.G. van der Meulen

nr 12
Staal in de Woningbouw, Korrosie-Bescherming van de Begane Grondvloer
Edwin J.F. Delsing

nr 13
Een Thermisch Model voor de Berekening van Staalplaatbetonvloeren onder Brandomstandigheden
A.F. Hamerlinck

nr 14
De Wijkgedachte in Nederland: Gemeenschapsstreven in een Stedebouwkundige Context
K. Doevendans
R. Stolzenburg

nr 15
Diaphragm Effect of Trapezoidally Profiled Steel Sheets: Experimental Research into the Influence of Force Application
Andre W.A.M.J. van den Bogaard

nr 16
Versterken met Spuit-Ferrocement: Het Mechanische Gedrag van met Spuit-Ferrocement Versterkte Gewapend Betonbalken
K.B. Lubir
M.C.G. van Wanroy

nr 17
De Tractaten van Jean Nicolas Louis Durand
G. van Zeyl

nr 18
Wonen onder een Plat Dak: Drie Opstellen over Enkele Vooronderstellingen van de Stedebouw
K. Doevendans

nr 19
Supporting Decision Making Processes: A Graphical and Interactive Analysis of Multivariate Data
W. Adams

nr 20
Self-Help Building Productivity: A Method for Improving House Building by Low-Income Groups Applied to Kenya 1990-2000
P. A. Erkelens

nr 21
De Verdeling van Woningen: Een Kwestie van Onderhandelen
Vincent Smit

nr 22
Flexibiliteit en Kosten in het Ontwerpproces: Een Besluitvormingondersteunend Model
M. Prins

nr 23
Spontane Nederzettingen Begeleid: Voorwaarden en Criteria in Sri Lanka
Po Hin Thung

nr 24
Fundamentals of the Design of Bamboo Structures
Oscar Arce-Villalobos

nr 25
Concepten van de Bouwkunde
M.F.Th. Bax (red.)
H.M.G.J. Trum (red.)

nr 26
Meaning of the Site
Xiaodong Li

nr 27
Het Woonmilieu op Begrip Gebracht: Een Speurtocht naar de Betekenis van het Begrip 'Woonmilieu'
Jaap Ketelaar

nr 28
Urban Environment in Developing Countries
editors: Peter A. Erkelens
George G. van der Meulen (red.)

nr 29
Stategische Plannen voor de Stad: Onderzoek en Planning in Drie Steden
prof.dr. H. Fassbinder (red.)
H. Rikhof (red.)

nr 30
Stedebouwkunde en Stadsbestuur
Piet Beekman

nr 31
De Architectuur van Djenné: Een Onderzoek naar de Historische Stad
P.C.M. Maas

nr 32
Conjoint Experiments and Retail Planning
Harmen Oppewal

nr 33
Strukturformen Indonesischer Bautechnik: Entwicklung Methodischer Grundlagen für eine 'Konstruktive Pattern Language' in Indonesien
Heinz Frick arch. SIA

nr 34
Styles of Architectural Designing: Empirical Research on Working Styles and Personality Dispositions
Anton P.M. van Bakel

nr 35
Conjoint Choice Models for Urban Tourism Planning and Marketing
Benedict Dellaert

nr 36
Stedelijke Planvorming als Co-Produktie
Helga Fassbinder (red.)

nr 37
Design Research in the Netherlands
editors: R.M. Oxman
M.F.Th. Bax
H.H. Achten

nr 38
Communication in the Building Industry
Bauke de Vries

nr 39
Optimaal Dimensioneren van Gelaste Plaatliggers
J.B.W. Stark
F. van Pelt
L.F.M. van Gorp
B.W.E.M. van Hove

nr 40
Huisvesting en Overwinning van Armoede
P.H. Thung
P. Beekman (red.)

nr 41
Urban Habitat: The Environment of Tomorrow
George G. van der Meulen
Peter A. Erkelens

nr 42
A Typology of Joints
John C.M. Olie

nr 43
Modeling Constraints-Based Choices for Leisure Mobility Planning
Marcus P. Stemerding

nr 44
Activity-Based Travel Demand Modeling
Dick Ettema

nr 45
Wind-Induced Pressure Fluctuations on Building Facades
Chris Geurts

nr 46
Generic Representations
Henri Achten

nr 47
Johann Santini Aichel: Architectuur en Ambiguiteit
Dirk De Meyer

nr 48
Concrete Behaviour in Multiaxial Compression
Erik van Geel

nr 49
Modelling Site Selection
Frank Witlox

nr 50
Ecolemma Model
Ferdinand Beetstra

nr 51
Conjoint Approaches to Developing Activity-Based Models
Donggen Wang

nr 52
On the Effectiveness of Ventilation
Ad Roos

nr 53
Conjoint Modeling Approaches for Residential Group preferences
Eric Molin

nr 54
Modelling Architectural Design Information by Features
Jos van Leeuwen

nr 55
A Spatial Decision Support System for the Planning of Retail and Service Facilities
Theo Arentze

nr 56
Integrated Lighting System Assistant
Ellie de Groot

nr 57
Ontwerpend Leren, Leren Ontwerpen
J.T. Boekholt

nr 58
Temporal Aspects of Theme Park Choice Behavior
Astrid Kemperman

nr 59
Ontwerp van een Geïndustrialiseerde Funderingswijze
Faas Moonen

nr 60
Merlin: A Decision Support System for Outdoor Leisure Planning
Manon van Middelkoop

nr 61
The Aura of Modernity
Jos Bosman

nr 62
Urban Form and Activity-Travel Patterns
Daniëlle Snellen

nr 63
Design Research in the Netherlands 2000
Henri Achten

nr 64
Computer Aided Dimensional Control in Building Construction
Rui Wu

nr 65
Beyond Sustainable Building
editors: Peter A. Erkelens
Sander de Jonge
August A.M. van Vliet
co-editor: Ruth J.G. Verhagen

nr 66
Das Globalrecyclingfähige Haus
Hans Löfflad

nr 67
Cool Schools for Hot Suburbs
René J. Dierkx

nr 68
A Bamboo Building Design Decision Support Tool
Fitri Mardjono

nr 69
Driving Rain on Building Envelopes
Fabien van Mook

nr 70
Heating Monumental Churches
Henk Schellen

nr 71
Van Woningverhuurder naar Aanbieder van Woongenot
Patrick Dogge

nr 72
Moisture Transfer Properties of Coated Gypsum
Emile Goossens

nr 73
Plybamboo Wall-Panels for Housing
Guillermo E. González-Beltrán

nr 74
The Future Site-Proceedings
Ger Maas
Frans van Gassel

nr 75
Radon transport in Autoclaved Aerated Concrete
Michel van der Pal

nr 76
The Reliability and Validity of Interactive Virtual Reality Computer Experiments
Amy Tan

nr 77
Measuring Housing Preferences Using Virtual Reality and Belief Networks
Maciej A. Orzechowski

nr 78
Computational Representations of Words and Associations in Architectural Design
Nicole Segers

nr 79
Measuring and Predicting Adaptation in Multidimensional Activity-Travel Patterns
Chang-Hyeon Joh

nr 80
Strategic Briefing
Fayez Al Hassan

nr 81
Well Being in Hospitals
Simona Di Cicco

nr 82
Solares Bauen: Implementierungs- und Umsetzungs-Aspekte in der Hochschulausbildung in Österreich
Gerhard Schuster

nr 83
Supporting Strategic Design of Workplace Environments with Case-Based Reasoning
Shauna Mallory-Hill

nr 84
ACCEL: A Tool for Supporting Concept Generation in the Early Design Phase
Maxim Ivashkov

nr 85
Brick-Mortar Interaction in Masonry under Compression
Ad Vermeltfoort

nr 86
Zelfredzaam Wonen
Guus van Vliet

nr 87
Een Ensemble met Grootstedelijke Allure
Jos Bosman
Hans Schippers

nr 88
On the Computation of Well-Structured Graphic Representations in Architectural Design
Henri Achten

nr 89
De Evolutie van een West-Afrikaanse Vernaculaire Architectuur
Wolf Schijns

nr 90
ROMBO Tactiek
Christoph Maria Ravesloot

nr 91
External Coupling between Building Energy Simulation and Computational Fluid Dynamics
Ery Djunaedy

nr 92
Design Research in the Netherlands 2005
editors: Henri Achten
Kees Dorst
Pieter Jan Stappers
Bauke de Vries

nr 93
Ein Modell zur Baulichen Transformation
Jalil H. Saber Zaimian

nr 94
Human Lighting Demands: Healthy Lighting in an Office Environment
Myriam Aries

nr 95
A Spatial Decision Support System for the Provision and Monitoring of Urban Greenspace
Claudia Pelizaro

nr 96
Leren Creëren
Adri Proveniers

nr 97
Simlandscape
Rob de Waard

nr 98
Design Team Communication
Ad den Otter

nr 99
Humaan-Ecologisch Georiënteerde Woningbouw
Juri Czabanowski

nr 100
Hambase
Martin de Wit

nr 101
Sound Transmission through Pipe Systems and into Building Structures
Susanne Bron-van der Jagt

nr 102
Het Bouwkundig Contrapunt
Jan Francis Boelen

nr 103
A Framework for a Multi-Agent Planning Support System
Dick Saarloos

nr 104
Bracing Steel Frames with Calcium Silicate Element Walls
Bright Mweene Ng'andu

nr 105
Naar een Nieuwe Houtskeletbouw
F.N.G. De Medts

nr 106 and 107
Niet gepubliceerd

nr 108
Geborgenheid
T.E.L. van Pinxteren

nr 109
Modelling Strategic Behaviour in Anticipation of Congestion
Qi Han

nr 110
Reflecties op het Woondomein
Fred Sanders

nr 111
On Assessment of Wind Comfort by Sand Erosion
Gábor Dezsö

nr 112
Bench Heating in Monumental Churches
Dionne Limpens-Neilen

nr 113
RE. Architecture
Ana Pereira Roders

nr 114
Toward Applicable Green Architecture
Usama El Fiky

nr 115
Knowledge Representation under Inherent Uncertainty in a Multi-Agent System for Land Use Planning
Liying Ma

nr 116
Integrated Heat Air and Moisture Modeling and Simulation
Jos van Schijndel

nr 117
Concrete Behaviour in Multiaxial Compression
J.P.W. Bongers

nr 118
The Image of the Urban Landscape
Ana Moya Pellitero

nr 119
The Self-Organizing City in Vietnam
Stephanie Geertman

nr 120
A Multi-Agent Planning Support System for Assessing Externalities of Urban Form Scenarios
Rachel Katoshevski-Cavari

nr 121
Den Schulbau Neu Denken, Fühlen und Wollen
Urs Christian Maurer-Dietrich

nr 122
Peter Eisenman Theories and Practices
Bernhard Kormoss

nr 123
User Simulation of Space Utilisation
Vincent Tabak

nr 125
In Search of a Complex System Model
Oswald Devisch

nr 126
Lighting at Work: Environmental Study of Direct Effects of Lighting Level and Spectrum on Psycho-Physiological Variables
Grazyna Górnicka

nr 127
Flanking Sound Transmission through Lightweight Framed Double Leaf Walls
Stefan Schoenwald

nr 128
Bounded Rationality and Spatio-Temporal Pedestrian Shopping Behavior
Wei Zhu

nr 129
Travel Information: Impact on Activity Travel Pattern
Zhongwei Sun

nr 130
Co-Simulation for Performance Prediction of Innovative Integrated Mechanical Energy Systems in Buildings
Marija Trčka

nr 131
Niet gepubliceerd

nr 132
Architectural Cue Model in Evacuation Simulation for Underground Space Design
Chengyu Sun

nr 133
Uncertainty and Sensitivity Analysis in Building Performance Simulation for Decision Support and Design Optimization
Christina Hopfe

nr 134
Facilitating Distributed Collaboration in the AEC/FM Sector Using Semantic Web Technologies
Jacob Beetz

nr 135
Circumferentially Adhesive Bonded Glass Panes for Bracing Steel Frame in Façades
Edwin Huveners

nr 136
Influence of Temperature on Concrete Beams Strengthened in Flexure with CFRP
Ernst-Lucas Klamer

nr 137
Sturen op Klantwaarde
Jos Smeets

nr 139
Lateral Behavior of Steel Frames with Discretely Connected Precast Concrete Infill Panels
Paul Teewen

nr 140
Integral Design Method in the Context of Sustainable Building Design
Perica Savanović

nr 141
Household Activity-Travel Behavior: Implementation of Within-Household Interactions
Renni Anggraini

nr 142
Design Research in the Netherlands 2010
Henri Achten

nr 143
Modelling Life Trajectories and Transport Mode Choice Using Bayesian Belief Networks
Marloes Verhoeven

nr 144
Assessing Construction Project Performance in Ghana
William Gyadu-Asiedu

nr 145
Empowering Seniors through Domotic Homes
Masi Mohammadi

nr 146
An Integral Design Concept for Ecological Self-Compacting Concrete
Martin Hunger

nr 147
Governing Multi-Actor Decision Processes in Dutch Industrial Area Redevelopment
Erik Blokhuis

nr 148
A Multifunctional Design Approach for Sustainable Concrete
Götz Hüsken

nr 149
Quality Monitoring in Infrastructural Design-Build Projects
Ruben Favié

nr 150
Assessment Matrix for Conservation of Valuable Timber Structures
Michael Abels

nr 151
Co-simulation of Building Energy Simulation and Computational Fluid Dynamics for Whole-Building Heat, Air and Moisture Engineering
Mohammad Mirsadeghi

nr 152
External Coupling of Building Energy Simulation and Building Element Heat, Air and Moisture Simulation
Daniel Cóstola

nr 153
Adaptive Decision Making In Multi-Stakeholder Retail Planning
Ingrid Janssen

nr 154
Landscape Generator
Kymo Slager

nr 155
Constraint Specification in Architecture
Remco Niemeijer

nr 156
A Need-Based Approach to Dynamic Activity Generation
Linda Nijland

nr 157
Modeling Office Firm Dynamics in an Agent-Based Micro Simulation Framework
Gustavo Garcia Manzato

nr 158
Lightweight Floor System for Vibration Comfort
Sander Zegers

nr 159
Aanpasbaarheid van de Draagstructuur
Roel Gijsbers

nr 160
'Village in the City' in Guangzhou, China
Yanliu Lin

nr 161
Climate Risk Assessment in Museums
Marco Martens

nr 162
Social Activity-Travel Patterns
Pauline van den Berg

nr 163
Sound Concentration Caused by Curved Surfaces
Martijn Vercammen

nr 164
Design of Environmentally Friendly Calcium Sulfate-Based Building Materials: Towards an Improved Indoor Air Quality
Qingliang Yu

nr 165
Beyond Uniform Thermal Comfort on the Effects of Non-Uniformity and Individual Physiology
Lisje Schellen

nr 166
Sustainable Residential Districts
Gaby Abdalla

nr 167
Towards a Performance Assessment Methodology using Computational Simulation for Air Distribution System Designs in Operating Rooms
Mônica do Amaral Melhado

nr 168
Strategic Decision Modeling in Brownfield Redevelopment
Brano Glumac

nr 169
Pamela: A Parking Analysis Model for Predicting Effects in Local Areas
Peter van der Waerden

nr 170
A Vision Driven Wayfinding Simulation-System Based on the Architectural Features Perceived in the Office Environment
Qunli Chen

nr 171
Measuring Mental Representations Underlying Activity-Travel Choices
Oliver Horeni

nr 172
Modelling the Effects of Social Networks on Activity and Travel Behaviour
Nicole Ronald

nr 173
Uncertainty Propagation and Sensitivity Analysis Techniques in Building Performance Simulation to Support Conceptual Building and System Design
Christian Struck

nr 174
Numerical Modeling of Micro-Scale Wind-Induced Pollutant Dispersion in the Built Environment
Pierre Gousseau

nr 175
Modeling Recreation Choices over the Family Lifecycle
Anna Beatriz Grigolon

nr 176
Experimental and Numerical Analysis of Mixing Ventilation at Laminar, Transitional and Turbulent Slot Reynolds Numbers
Twan van Hooff

nr 177
Collaborative Design Support: Workshops to Stimulate Interaction and Knowledge Exchange Between Practitioners
Emile M.C.J. Quanjel

nr 178
Future-Proof Platforms for Aging-in-Place
Michiel Brink

nr 179
Motivate: A Context-Aware Mobile Application for Physical Activity Promotion
Yuzhong Lin

nr 180
Experience the City: Analysis of Space-Time Behaviour and Spatial Learning
Anastasia Moiseeva

nr 181
Unbonded Post-Tensioned Shear Walls of Calcium Silicate Element Masonry
Lex van der Meer

nr 182
Construction and Demolition Waste Recycling into Innovative Building Materials for Sustainable Construction in Tanzania
Mwita M. Sabai

nr 183
Durability of Concrete with Emphasis on Chloride Migration
Przemysław Spiesz

nr 184
Computational Modeling of Urban Wind Flow and Natural Ventilation Potential of Buildings
Rubina Ramponi

nr 185
A Distributed Dynamic Simulation Mechanism for Buildings Automation and Control Systems
Azzedine Yahiaoui

nr 186
Modeling Cognitive Learning of Urban Networks in Daily Activity-Travel Behavior
Şehnaz Cenani Durmazoğlu

nr 187
Functionality and Adaptability of Design Solutions for Public Apartment Buildings in Ghana
Stephen Agyefi-Mensah

nr 188
A Construction Waste Generation Model for Developing Countries
Lilliana Abarca-Guerrero

nr 189
Synchronizing Networks: The Modeling of Supernetworks for Activity-Travel Behavior
Feixiong Liao

nr 190
Time and Money Allocation Decisions in Out-of-Home Leisure Activity Choices
Gamze Zeynep Dane

nr 191
How to Measure Added Value of CRE and Building Design
Rianne Appel-Meulenbroek

nr 192
Secondary Materials in Cement-Based Products: Treatment, Modeling and Environmental Interaction
Miruna Florea

nr 193
Concepts for the Robustness Improvement of Self-Compacting Concrete: Effects of Admixtures and Mixture Components on the Rheology and Early Hydration at Varying Temperatures
Wolfram Schmidt

nr 194
Modelling and Simulation of Virtual Natural Lighting Solutions in Buildings
Rizki A. Mangkuto

nr 195
Nano-Silica Production at Low Temperatures from the Dissolution of Olivine - Synthesis, Tailoring and Modelling
Alberto Lazaro Garcia

nr 196
Building Energy Simulation Based Assessment of Industrial Halls for Design Support
Bruno Lee

nr 197
Computational Performance Prediction of the Potential of Hybrid Adaptable Thermal Storage Concepts for Lightweight Low-Energy Houses
Pieter-Jan Hoes

nr 198
Application of Nano-Silica in Concrete
George Quercia Bianchi

nr 199
Dynamics of Social Networks and Activity Travel Behaviour
Fariya Sharmeen

nr 200
Building Structural Design Generation and Optimisation including Spatial Modification
Juan Manuel Davila Delgado

nr 201
Hydration and Thermal Decomposition of Cement/Calcium-Sulphate Based Materials
Ariën de Korte

nr 202
Republiek van Beelden:
De Politieke Werkingen van het Ontwerp in Regionale Planvorming
Bart de Zwart

nr 203
Effects of Energy Price Increases on Individual Activity-Travel Repertoires and Energy Consumption
Dujuan Yang

nr 204
Geometry and Ventilation:
Evaluation of the Leeward Sawtooth Roof Potential in the Natural Ventilation of Buildings
Jorge Isaac Perén Montero

nr 205
Computational Modelling of Evaporative Cooling as a Climate Change Adaptation Measure at the Spatial Scale of Buildings and Streets
Hamid Montazeri

nr 206
Local Buckling of Aluminium Beams in Fire Conditions
Ronald van der Meulen

nr 207
Historic Urban Landscapes:
Framing the Integration of Urban and Heritage Planning in Multilevel Governance
Loes Veldpaus

nr 208
Sustainable Transformation of the Cities:
Urban Design Pragmatics to Achieve a Sustainable City
Ernesto Antonio Zumelzu Scheel

nr 209
Development of Sustainable Protective Ultra-High Performance Fibre Reinforced Concrete (UHPFRC):
Design, Assessment and Modeling
Rui Yu

nr 210
Uncertainty in Modeling Activity-Travel Demand in Complex Uban Systems
Soora Rasouli

nr 211
Simulation-based Performance Assessment of Climate Adaptive Greenhouse Shells
Chul-sung Lee

nr 212
Green Cities:
Modelling the Spatial Transformation of the Urban Environment using Renewable Energy Technologies
Saleh Mohammadi

nr 213
A Bounded Rationality Model of Short and Long-Term Dynamics of Activity-Travel Behavior
Ifigeneia Psarra

nr 214
Effects of Pricing Strategies on Dynamic Repertoires of Activity-Travel Behaviour
Elaheh Khademi

nr 215
Handstorm Principles for Creative and Collaborative Working
Frans van Gassel

nr 216
Light Conditions in Nursing Homes: Visual Comfort and Visual Functioning of Residents
Marianne M. Sinoo

nr 217
Woonsporen: De Sociale en Ruimtelijke Biografie van een Stedelijk Bouwblok in de Amsterdamse Transvaalbuurt
Hüseyin Hüsnü Yegenoglu

nr 218
Studies on User Control in Ambient Intelligent Systems
Berent Willem Meerbeek

nr 219
Daily Livings in a Smart Home: Users' Living Preference Modeling of Smart Homes
Erfaneh Allameh

nr 220
Smart Home Design: Spatial Preference Modeling of Smart Homes
Mohammadali Heidari Jozam

nr 221
Wonen: Discoursen, Praktijken, Perspectieven
Jos Smeets

nr 222
Personal Control over Indoor Climate in Offices: Impact on Comfort, Health and Productivity
Atze Christiaan Boerstra

nr 223
Personalized Route Finding in Multimodal Transportation Networks
Jianwe Zhang

nr 224
The Design of an Adaptive Healing Room for Stroke Patients
Elke Daemen

nr 225
Experimental and Numerical Analysis of Climate Change Induced Risks to Historic Buildings and Collections
Zara Huijbregts

nr 226
Wind Flow Modeling in Urban Areas Through Experimental and Numerical Techniques
Alessio Ricci

nr 227
Clever Climate Control for Culture: Energy Efficient Indoor Climate Control Strategies for Museums Respecting Collection Preservation and Thermal Comfort of Visitors
Rick Kramer

nr 228
Fatigue Life Estimation of Metal Structures Based on Damage Modeling
Sarmediran Silitonga

nr 229
A multi-agents and occupancy based strategy for energy management and process control on the room-level
Timilehin Moses Labeodan

nr 230
Environmental assessment of Building Integrated Photovoltaics: Numerical and Experimental Carrying Capacity Based Approach
Michiel Ritzen

nr 231
Performance of Admixture and Secondary Minerals in Alkali Activated Concrete: Sustaining a Concrete Future
Arno Keulen

nr 232
World Heritage Cities and Sustainable Urban Development:
Bridging Global and Local Levels in Monitoring the Sustainable Urban Development of World Heritage Cities
Paloma C. Guzman Molina

nr 233
Stage Acoustics and Sound Exposure in Performance and Rehearsal Spaces for Orchestras:
Methods for Physical Measurements
Remy Wenmaekers

nr 234
Municipal Solid Waste Incineration (MSWI) Bottom Ash:
From Waste to Value Characterization, Treatments and Application
Pei Tang

nr 235
Large Eddy Simulations Applied to Wind Loading and Pollutant Dispersion
Mattia Ricci

nr 236
Alkali Activated Slag-Fly Ash Binders: Design, Modeling and Application
Xu Gao

nr 237
Sodium Carbonate Activated Slag: Reaction Analysis, Microstructural Modification & Engineering Application
Bo Yuan

nr 238
Shopping Behavior in Malls
Widiyani

nr 239
Smart Grid-Building Energy Interactions: Demand Side Power Flexibility in Office Buildings
Kennedy Otieno Aduda

nr 240
Modeling Taxis Dynamic Behavior in Uncertain Urban Environments
Zheng Zhong

nr 241
Gap-Theoretical Analyses of Residential Satisfaction and Intention to Move
Wen Jiang

nr 242
Travel Satisfaction and Subjective Well-Being: A Behavioral Modeling Perspective
Yanan Gao

nr 243
Building Energy Modelling to Support the Commissioning of Holistic Data Centre Operation
Vojtech Zavrel

nr 244
Regret-Based Travel Behavior Modeling: An Extended Framework
Sunghoon Jang

nr 245
Towards Robust Low-Energy Houses: A Computational Approach for Performance Robustness Assessment using Scenario Analysis
Rajesh Reddy Kotireddy

nr 246
Development of sustainable and functionalized inorganic binder-biofiber composites
Guillaume Doudart de la Grée

nr 247
A Multiscale Analysis of the Urban Heat Island Effect: From City Averaged Temperatures to the Energy Demand of Individual Buildings
Yasin Toparlar

nr 248
Design Method for Adaptive Daylight Systems for buildings covered by large (span) roofs
Florian Heinzelmann

nr 249
Hardening, high-temperature resistance and acid resistance of one-part geopolymers
Patrick Sturm

nr 250
Effects of the built environment on dynamic repertoires of activity-travel behaviour
Aida Pontes de Aquino

nr 251
Modeling for auralization of urban environments: Incorporation of directivity in sound propagation and analysis of a framework for auralizing a car pass-by
Fotis Georgiou

In a solar tower plant, temperatures up to 700°C are reached by moving mirror systems called ‘heliostats’ tracking the sun and concentrating its radiation to the top of a tower for large scale electricity production and industrial process heating. To enable a breakthrough of this solar energy technology the heliostat costs have to be further reduced. With precise knowledge of the wind loads they can be built lighter and cheaper. The objective of the presented thesis is to close knowledge gaps and to reduce uncertainties regarding the wind loading of heliostats. Some of the main open questions were the following:

- How can the wind loads on heliostats be reduced in an economic way?
- Which is the optimum aspect ratio of the mirror panel?
- At which heliostat field position do maximum wind loads occur?
- Do the wind load coefficients of heliostats depend on the wind speed?
- Which turbulence properties have to be matched by wind tunnel tests?
- Can the peak wind loads be reduced by shock absorbers?

By wind tunnel tests and full scale measurements these questions were addressed. The results are also valid for double axis photovoltaic trackers. With the gained knowledge, new heliostat designs were developed with cost reductions of up to 25%.

/ Department of the Built Environment

TU/e Technische Universiteit Eindhoven University of Technology